

Theory of Electron and Phonon Transport in Nano and Molecular Quantum Devices

Design strategies for molecular electronics and thermoelectricity

Hatef Sadeghi

PhD Thesis in Nanoelectronics

Submitted in part fulfilment of the requirements for the degree of Doctor of Philosophy

July 4, 2016



Declaration

Except where stated otherwise, this thesis is a result of the author's original work and has not been submitted in whole or in part for the award of a higher degree elsewhere. This thesis documents work carried out between November 2011 and May 2016 at Lancaster University, UK, under the supervision of Prof. Colin J. Lambert and funded by EU ITN NanoCTM network and a faculty of science and technology studentship.

Hatef Sadeghi

July 4, 2016

*To my parents, Tahereh Moslemi and Hafez Sadeghi
and in memory of my grandmother Fatemeh Azarpeyvand,
people who had a great influence in my life.*

Abstract

Understanding the electronic and phononic transport properties of junctions consisting of a scattering region such as a nanoscale region or molecule connected two or more electrodes is the central basis for future nano and molecular scale applications. The theoretical and mathematical techniques to treat electron and phonon transport are leading to model the physical properties of nano and molecular scale junctions. In this thesis, I use these methods not only to understand the experimental observations by experimental collaborators, but also to develop strategies to design and engineer molecular electronic building blocks, thermoelectric devices and sensors.

In this thesis, after a discussion about the theoretical methods used to model electron and phonon transport through the nanoscale junctions, I cover four main results in the areas of molecular sensing, new graphene-based molecular junctions, quantum interference rules and thermoelectricity (or thermal management). I demonstrate the discriminating sensing properties of new bilayer-graphene, sculptureene-based nano-pore devices for DNA sequencing. A unique and novel signal processing method is presented to selectively sense the nucleobases based on direct electrical current. Then I consider a newly developed platform for single-molecule device fabrication based on electro-burnt graphene nano-junctions, which allows three terminal device realization at a single molecule level with gating capability. I provide a fundamental understanding of transport phenomena in these junctions. Furthermore, I discuss our newly developed mid-gap transport theory for single molecules, where in the weak coupling regime and in the vicinity of the middle of the HOMO and LUMO gap, a minimal parameter-free theory of the connectivity dependent transport and quantum interference could be used to model conductance measurements in polycyclic aromatic hydrocarbons. After these discussion of the electronic properties of the junctions, I consider the phonon transport through the nano and molecular scale devices. This allows me to identify strategies for controlling the transmission of phonons from one side of the junction to another for both low-power thermoelectric and thermal management devices.

Acknowledgements

First and foremost, I would like to thank God, whose many blessings have made me who I am today. Also I would like to express a deep sense of gratitude to my beloved parents, to whom I owe my life for their constant love, encouragement, support and blessings.

This thesis would not have been possible without support and guidance from a number of people. I was incredibly fortunate to work with and learn from my supervisor, Professor Colin J. Lambert, whose encouragement, guidance and great support enabled me to develop a deep understanding of the "*Nanoscale Transport*". I am heartily thankful for all amazing lectures and the incredible discussions we had, for providing a great opportunity for communicating with other experimental and theoretical groups in my field of research and creating very positive environment to grow.

I would like to thank my beloved wife and colleague, Sara Sangtarash, with whom I started this fantastic spiritual and scientific journey and enjoy every single moment of that. I would like to thank Prof. Jaime Ferrer, (Oviedo University, Spain) for his continued support in developing the Gollum transport code and Prof. John J. Jefferson (Lancaster University, UK) for very useful discussions. I also would like to thank my experimental collaborators, Prof. G. Andrew D. Briggs (Oxford University, UK), Prof. Harry L. Anderson (Oxford University, UK), Prof. Lesley F. Cohen (Imperial College London, UK), Prof. Stuart A. Solin (Washington University in St. Louis, USA), Prof. Silvio Decurtins (University of Bern, Switzerland), Prof. Thomas Wandlowski (University of Bern, Switzerland), Prof. Kyriakos Porfyraakis (Oxford University, UK), Prof. Jamie Warner (Oxford University, UK), Dr. Olga Kazakova (National Physical Laboratory, UK) and Prof. Martin Bryce (Durham University, UK) for remarkable synthesis and measurements and very useful discussions. Of course I also thank their group members who actually have carried out the experiments, Jan, Aaron, Pascal, Gregory, Adam, Vish, Shi-Xia and Wenjing.

I would also like to thank Dr. Steven Bailey, Dr. Iain Grace and Dr. Victor Manuel Garcia-Suarez for helping me to use the SIESTA DFT code. I thank the other group members who have created a great environment and have been good friends; Qusiy, Laith, Mohammed, Marco, Thomas, Kata, Ahmed, Nasser, David, Csaba and many others. I was appointed as Marie Curie Early Stage Researcher (ESR) at Lancaster University within Nanoelectronics: Concepts, Theory and Modeling EU Innovative Training Network (EU ITN: NanoCTM) to pursue my PhD

study in Nanoscience. I would like to thank the funding resources, EU NanoCTM network and the faculty of science and technology studentship. And finally I would like to thank my beloved brother Faraz, who has always stood by me in times of need and his support and encouragement was worth more than I can express.

List of publication during my PhD study

During my PhD studies I published the following journal articles and patent:

Patent

1. Nanopore arrangement for DNA sequencing Hatef Sadeghi, Colin J Lambert, Laith Algharagholy, Steven William Dennis Bailey, Jaime Ferrer and Vctor M Garca-Surez 18/12/2013
Patent number: WO2015092411A1

Journal articles

1. Functionalization mediates heat transport in graphene nanoflakes, Han, H., Zhang, Y., Wang, N., Samani, M.K., Ni, Y., Mijbil, Z.Y., Edwards, M., Xiong, S., Saaskilahti, K., Murugesan, M., Fu, Y., Ye, L., Sadeghi, H., Bailey, S., Kosevich, YA., Lambert, C.J., Liu, J., Volz, S. 2016/04/29 In: Nature Communications. 7, p. 11281, 9 p.
2. Tuning the thermoelectric properties of metallo-porphyrins, Al-Galiby, Q.H., Sadeghi, H., Algharagholy, L.A., Grace, I., Lambert, C.J. 5/1/2016 In: Nanoscale. 8 (4), p. 2428-2433, 6 p.
3. Multifunctional semiconductor micro-Hall devices for magnetic, electric, and photo-detection Gilbertson, A.M., Sadeghi, H., Panchal, V., Kazakova, O., Lambert, C.J., Solin, S.A., Cohen, L.F. 9/12/2015 In: Applied Physics Letters. 107, 23, 6 p.
4. Negative differential electrical resistance of a rotational organic nanomotor Sadeghi, H., Sangtarash, S., Al-galiby, Q., Sparks, R., Bailey, S., Lambert, C.J. 8/12/2015 In: Beilstein Journal of Nanotechnology. 6 (1), p. 2332-2337. 6 p.
5. Redox-dependent Franck-Condon blockade and avalanche transport in a graphene-fullerene single-molecule transistor Chit Siong Lau, Hatef Sadeghi, Gregory Rogers, Sara Sangtarash, Panagiotis Dallas, Kyriakos Porfyrakis, Jamie H Warner, Colin J Lambert, G Andrew D Briggs, Jan Mol 7/12/2015 In: Nano letters
6. Tuning thermoelectric properties of graphene/boron nitride heterostructures Algharagholy, L.A., Al-Galiby, Q., Marhoon, H.A., Sadeghi, H., Abduljalil, H.M., Lambert, C.J. 3/11/2015

In: *Nanotechnology*. 26, 47, 9 p.

7. Oligoynes molecular junctions for efficient room temperature thermoelectric power generation Sadeghi, H., Sangtarash, S., Lambert, C.J. 12/10/2015 In: *Nano Letters*. 15, 11, p. 7467-7472. 6 p.
8. Hexagonal-boron nitride substrates for electroburnt graphene nanojunctions Sadeghi, H., Sangtarash, S., Lambert, C. 18/09/2015 In: *Physica E: Low-dimensional Systems and Nanostructures*.
9. Searching the hearts of graphene-like molecules for simplicity, sensitivity, and logic Sangtarash, S., Huang, C., Sadeghi, H., Sorohhov, G., Hauser, J., Wandlowski, T., Hong, W., Decurtins, S., Liu, S., Lambert, C.J. 9/09/2015 In: *Journal of the American Chemical Society*. 137, 35, p. 11425-11431. 7 p.
10. Graphene-porphyrin single-molecule transistors Mol, J.A., Lau, C.S., Lewis, W.J.M., Sadeghi, H., Roche, C., Cnossen, A., Warner, J.H., Lambert, C.J., Anderson, H.L., Briggs, G.A.D. 10/07/2015 In: *Nanoscale*. 7, 31, p. 13181-13185. 4 p.
11. Electron and heat transport in porphyrin-based single-molecule transistors with electroburnt graphene electrodes Sadeghi, H., Sangtarash, S., Lambert, C.J. 26/06/2015 In: *Beilstein Journal of Nanotechnology*. 6, p. 1413-1420. 8 p.
12. Enhancing the thermoelectric figure of merit in engineered graphene nanoribbons Sadeghi, H., Sangtarash, S., Lambert, C.J. 18/05/2015 In: *Beilstein Journal of Nanotechnology*. 6, p. 1176-1182. 7 p.
13. Enhanced thermoelectric efficiency of porous silicene nanoribbons Sadeghi, H., Sangtarash, S., Lambert, C.J. 30/03/2015 In: *Scientific Reports*. 5
14. Magic ratios for connectivity-driven electrical conductance of graphene-like molecules Geng, Y., Sangtarash, S., Huang, C., Sadeghi, H., Fu, Y., Hong, W., Wandlowski, T., Decurtins, S., Lambert, C.J., Liu, S. 17/03/2015 In: *Journal of the American Chemical Society*. 137, 13, p. 4469-4476. 8 p.
15. Exploiting the extended π -system of perylene bisimide for label-free single-molecule sensing Al-Galiby, Q., Grace, I., Sadeghi, H., Lambert, C.J. 7/03/2015 In: *Journal of Materials Chemistry C*. 3, 9, p. 2101-2106. 6 p.

16. A quantum circuit rule for interference effects in single-molecule electrical junctions Manrique, D.Z., Huang, C., Baghernejad, M., Zhao, X., Al-owaedi, O.A., Sadeghi, H., Kaliginedi, V., Hong, W., Gulcur, M., Wandlowski, T., Bryce, M.R., Lambert, C.J. 3/03/2015 In: Nature Communications. 6
17. Conductance enlargement in picoscale electroburnt graphene nanojunctions Sadeghi, H., Mol, J.A., Lau, C.S., Briggs, G.A.D., Warner, J., Lambert, C.J. 3/03/2015 In: Proceedings of the National Academy of Sciences. 112, 9, p. 2658-2663. 6 p.
18. GOLLUM: a next-generation simulation tool for electron, thermal and spin transport Ferrer, J., Lambert, C., Garcia-Suarez, V.M., Manrique, D.Z., Visontai, D., Oroszlany, L., Rodriguez-Ferradas, R., Grace, I., Bailey, S.W.D., Gillemot, K., Sadeghi, H., Algharagholy, L.A. 23/09/2014 In: New Journal of Physics. 16, 9, 66 p.
19. Graphene sculpture nanpores for DNA nucleobase sensing Sadeghi, H., Algharagholy, L., Pope, T., Bailey, S., Visontai, D., Manrique, D., Ferrer, J., Garcia-Suarez, V., Sangtarash, S., Lambert, C.J. 19/06/2014 In: Journal of Physical Chemistry B. 118, 24, p. 6908-6914. 7 p.
20. Electrical transport model of silicene as a channel of field effect transistor Sadeghi, H. 06/2014 In: Journal of Nanoscience and Nanotechnology. 14, 6, p. 4178-4184. 7 p.
21. Silicene-based DNA nucleobase sensing Sadeghi, H., Bailey, S., Lambert, C.J. 13/05/2014 In: Applied Physics Letters. 104, 5 p.

Contents

1	Introduction	11
1.1	Molecular Electronics	11
1.2	Thesis Outline	12
2	Transport in molecular scale	16
2.0.1	Schrödinger equation	17
2.0.2	Density functional theory (DFT)	19
2.0.3	Tight-Binding Model	23
2.0.4	Current carried by a Bloch function	28
2.1	Transport on resonance and off resonance	29
2.1.1	Breit-Wigner formula (BWF)	31
2.1.2	Scattering theory and non-equilibrium Green's function	31
2.1.3	The Landauer Formula	33
2.1.4	Generalized model to calculate $T(E)$	35
2.1.5	Equilibrium vs. non-equilibrium I-V	39
2.1.6	Master equation	42
2.2	Modelling the experiment	45
2.2.1	Virtual leads versus physical leads	46
2.2.2	Charge, spin and and thermal currents	47
2.2.3	Phonon thermal conductance	50
2.2.4	Spectral adjustment	51
2.2.5	Inclusion of a Gauge field	52
2.2.6	Superconducting systems	52
2.2.7	Environmental effects	54
2.3	GOLLUM transport code	55

3	DNA nucleobase sensing	58
4	Picoscale graphene nanojunctions	78
5	A Magic-Ratio Rule (MRR)	99
6	Molecular thermoelectric devices	119
7	Conclusions	142
A	Analytical calculation for the electrical conductance of rings and chains	145
B	Connectivity driven conductances in molecular junctions	150

Chapter 1

Introduction

1.1 Molecular Electronics

The idea of using single molecules as building blocks to design and fabricate molecular electronic components has been around for more than 40 years [1], but only recently it has attracted huge scientific interest to explore their unique properties and opportunities. Molecular electronics including self-assembled monolayers [2] and single-molecule junctions [3] are of interest not only for their potential to deliver logic gates [4], sensors[5], and memories [6] with ultra-low power requirements and sub-10-nm device footprints, but also for their ability to probe room-temperature quantum properties at a molecular scale such as quantum interference [7] and thermoelectricity [8]. There are five main area of research in molecular-scale electronics [3] namely: Molecular mechanics, molecular optoelectronics, molecular electronics, molecular spintronics and molecular thermoelectrics as shown in figure 1.1.1 in which studying the electronic and phononic transport properties of the junction is the central basis toward junction characterization for a wide range of the applications.

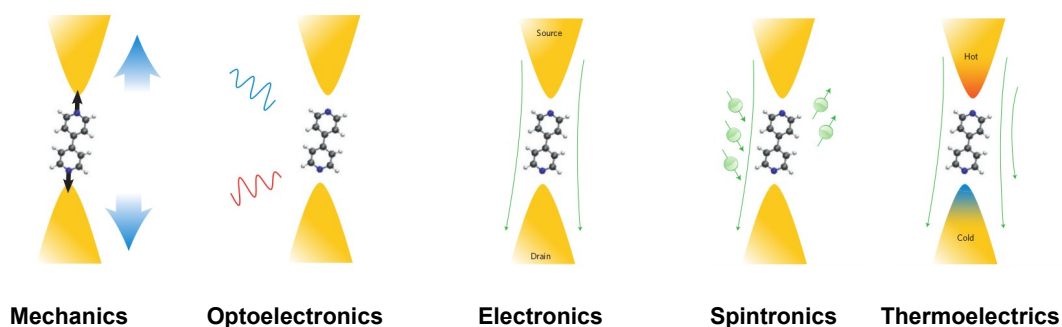


Figure 1.1.1: Molecular electronic active area of research[3]

By studying electron and phonon transport across a junction consisting of two or more electrodes connected to a single or a few hundred molecules, one could study all phenomenon shown in figure 1.1.1 from mechanical properties of the junction to electronic and thermoelectrics. For example, when a single molecule is attached to metallic electrodes, de Broglie waves of electrons entering the molecule from one electrode and leaving through the other form complex interference patterns inside the molecule. These patterns could be utilize to optimize the single-molecule device performance [4, 9]. Furthermore, recently their potential for removing heat from nanoelectronic devices (thermal management) and thermoelectrically converting waste heat into electricity has also been recognised [8]. Indeed, electrons passing through single molecules have been demonstrated to remain phase coherent, even at room temperature. In practice, the task of identifying and harnessing quantum effects is hampered because transport properties are strongly affected by the method used to anchor single molecules to electrodes.

1.2 Thesis Outline

My aim in this thesis is to review the theoretical and mathematical techniques to treat electron and phonon transport in nano and molecular scale junctions leading to models of their physical properties. This helps not only to understand the experimental observations but also provides a vital design tool to develop strategies for molecular electronic building blocks, thermoelectric device and sensors. In my PhD study, I have tried to cover both aspects. In this period, not only I have used this techniques to understand the experiments done by our collaborators [9–13], but also I have introduced a set of the strategies to enhance the thermoelectric power generation [8, 14–18], to design single molecule transistors [15] and nanomotors [19], to use quantum interference for logic applications [4, 20], to use graphene to probe molecules [21, 22], for DNA sequencing [21, 23, 24], for molecular sensing [25, 26] and to engineer phonons' transport through the junction [8].

In this thesis after this introductory chapter, I introduce the general idea about nanoscale transport and the methods which could be applied to model nano and molecular scale devices. In the next chapters, four selected papers out of my publication are included. I then close with the discussion and concluding chapter.

References

- [1] “Visions for a molecular future,” *Nature Nanotechnology*, vol. 8, no. 6, pp. 385–389, 2013.
- [2] J. L. Christopher, L. A. Estroff, J. K. Kriebel, R. G. Nuzzo, and G. M. Whitesides, “Self-assembled monolayers of thiolates on metals as a form of nanotechnology,” *Chemical Reviews*, vol. 105, no. 4, pp. 1103–1170, 2005. PMID: 15826011.
- [3] S. V. Aradhyia and L. Venkataraman, “Single-molecule junctions beyond electronic transport,” *Nature Nanotechnology*, vol. 8, no. 6, pp. 399–410, 2013.
- [4] S. Sangtarash, C. Huang, H. Sadeghi, G. Sorohhov, J. Hauser, T. Wandlowski, W. Hong, S. Decurtins, S.-X. Liu, and C. J. Lambert, “Searching the Hearts of Graphene-like Molecules for Simplicity, Sensitivity, and Logic,” *Journal of the American Chemical Society*, vol. 137, no. 35, pp. 11425–11431, 2015.
- [5] H. Sadeghi, L. Algaragholy, T. Pope, S. Bailey, D. Visontai, D. Manrique, J. Ferrer, V. Garcia-Suarez, S. Sangtarash, and C. J. Lambert, “Graphene sculpture nanpores for DNA nucleobase sensing,” *Journal of Physical Chemistry B*, vol. 118, no. 24, pp. 6908–6914, 2014.
- [6] T. Prodromakis, C. Toumazou, and L. Chua, “Two centuries of memristors,” *Nature Materials*, vol. 11, no. 6, pp. 478–481, 2012.
- [7] C. J. Lambert, “Basic concepts of quantum interference and electron transport in single-molecule electronics,” *Chem. Soc. Rev.*, vol. 44, pp. 875–888, 2015.
- [8] H. Sadeghi, S. Sangtarash, and C. J. Lambert, “Oligoynes molecular junctions for efficient room temperature thermoelectric power generation,” *Nano letters*, vol. 15, no. 11, pp. 7467–7472, 2015.
- [9] Y. Geng, S. Sangtarash, C. Huang, H. Sadeghi, Y. Fu, W. Hong, T. Wandlowski, S. Decurtins, C. J. Lambert, and S.-X. Liu, “Magic Ratios for Connectivity-Driven Electrical Conductance of Graphene-like Molecules,” *Journal of the American Chemical Society*, vol. 137, no. 13, pp. 4469–4476, 2015.
- [10] J. A. Mol, C. S. Lau, W. J. Lewis, H. Sadeghi, C. Roche, A. Cnossen, J. H. Warner, C. J. Lambert, H. L. Anderson, and G. A. D. Briggs, “Graphene-porphyrin single-molecule transistors,” *Nanoscale*, vol. 7, no. 31, pp. 13181–13185, 2015.

- [11] H. Han, Y. Zhang, Z. Y. Mijbil, H. Sadeghi, Y. Ni, S. Xiong, K. Saaskilahti, S. Bailey, Y. A. Kosevich, J. Liu, *et al.*, “Functionalization mediates heat transport in graphene nanoflakes,” *arXiv preprint arXiv:1508.01616*, 2015.
- [12] C. S. Lau, H. Sadeghi, G. Rogers, S. Sangtarash, P. Dallas, K. Porfyraakis, J. Warner, C. J. Lambert, G. A. D. Briggs, and J. A. Mol, “Redox-dependent Franck–Condon blockade and avalanche transport in a graphene–fullerene single-molecule transistor,” *Nano letters*, vol. 16, no. 1, pp. 170–176, 2015.
- [13] A. Gilbertson, H. Sadeghi, V. Panchal, O. Kazakova, C. Lambert, S. Solin, and L. Cohen, “Multifunctional semiconductor micro-hall devices for magnetic, electric, and photo-detection,” *Applied Physics Letters*, vol. 107, no. 23, p. 233504, 2015.
- [14] H. Sadeghi, S. Sangtarash, and C. J. Lambert, “Enhancing the thermoelectric figure of merit in engineered graphene nanoribbons,” *Beilstein journal of nanotechnology*, vol. 6, no. 1, pp. 1176–1182, 2015.
- [15] H. Sadeghi, S. Sangtarash, and C. J. Lambert, “Electron and heat transport in porphyrin-based single-molecule transistors with electro-burnt graphene electrodes,” *Beilstein journal of nanotechnology*, vol. 6, no. 1, pp. 1413–1420, 2015.
- [16] H. Sadeghi, S. Sangtarash, and C. J. Lambert, “Enhanced thermoelectric efficiency of porous silicene nanoribbons,” *Scientific reports*, vol. 5, 2015.
- [17] L. A. Algharagholy, Q. Al-Galiby, H. A. Marhoon, H. Sadeghi, H. M. Abduljalil, and C. J. Lambert, “Tuning thermoelectric properties of graphene/boron nitride heterostructures,” *Nanotechnology*, vol. 26, no. 47, p. 475401, 2015.
- [18] Q. H. Al-Galiby, H. Sadeghi, L. A. Algharagholy, I. Grace, and C. Lambert, “Tuning the thermoelectric properties of metallo-porphyrins,” *Nanoscale*, vol. 8, no. 4, pp. 2428–2433, 2016.
- [19] H. Sadeghi, S. Sangtarash, Q. Al-Galiby, R. Sparks, S. Bailey, and C. J. Lambert, “Negative differential electrical resistance of a rotational organic nanomotor,” *Beilstein journal of nanotechnology*, vol. 6, no. 1, pp. 2332–2337, 2015.
- [20] H. Sadeghi, J. A. Mol, C. S. Lau, G. A. D. Briggs, J. Warner, and C. J. Lambert, “Conduc-

- tance enlargement in picoscale electroburnt graphene nanojunctions,” *Proceedings of the National Academy of Sciences*, vol. 112, no. 9, pp. 2658–2663, 2015.
- [21] H. Sadeghi, L. Algharagholy, T. Pope, S. Bailey, D. Visontai, D. Manrique, J. Ferrer, V. Garcia-Suarez, S. Sangtarash, and C. J. Lambert, “Graphene sculpture nanopores for dna nucleobase sensing,” *The Journal of Physical Chemistry B*, vol. 118, no. 24, pp. 6908–6914, 2014.
- [22] H. Sadeghi, S. Sangtarash, and C. Lambert, “Hexagonal-boron nitride substrates for electroburnt graphene nanojunctions,” *Physica E: Low-dimensional Systems and Nanostructures*, 2015.
- [23] H. Sadeghi, S. Bailey, and C. J. Lambert, “Silicene-based dna nucleobase sensing,” *Applied Physics Letters*, vol. 104, no. 10, p. 103104, 2014.
- [24] H. Sadeghi, C. J. Lambert, L. Algharagholy, S. W. D. Bailey, J. Ferrer, and V. M. Garcia-Suarez, “Nanopore arrangement for dna sequencing,” 2015.
- [25] Q. Al-Galiby, I. Grace, H. Sadeghi, and C. J. Lambert, “Exploiting the extended π -system of perylene bisimide for label-free single-molecule sensing,” *Journal of Materials Chemistry C*, vol. 3, no. 9, pp. 2101–2106, 2015.
- [26] L. Algharagholy, T. Pope, Q. Al-Galiby, H. Sadeghi, S. W. Bailey, and C. J. Lambert, “Sensing single molecules with carbon-boron-nitride nanotubes,” *Journal of Materials Chemistry C*, vol. 3, no. 39, pp. 10273–10276, 2015.

Chapter 2

Transport in molecular scale

My focus in this chapter is on reviewing the methods used to model electron and phonon transport in nano and molecular scale systems. Any device consists of two or more electrodes (leads) connected to a scattering region (figure 2.0.1). The electrodes are perfect waveguides where electrons and phonons transmit without any scattering. The main scattering occurs either at the junction to the leads or inside the scattering region. The goal is to understand electrical and vibrational properties of nano and molecular junctions where nanoscale scatter or molecules are the bridge between the electrodes with or without surroundings, such as an electric field (gate and bias voltages or local charge), a magnetic field, a laser beam or a molecular environment (water, gases, biological species, donors and acceptors, etc). In principle, the molecule could be coupled to the electrodes with a weak or strong coupling strength. However, in most cases the coupling is weak. There are different approaches to study the electronic and vibrational properties of the junctions [1] though, my focus in this thesis is mostly on the Green's function formalism and partially the master equation approach.

In this chapter, I will begin with the Schrödinger equation and try to relate it to the physical description of matter at the nano and molecular scale. Then I will discuss the definition of the current using the time-dependent Schrödinger equation and introduce tight binding description of the quantum system. The scattering theory and non-equilibrium Green's function method are discussed and different transport regimes (on and off resonances) are considered. One dimensional system and a more general multi-channel method are derived to calculate transmission coefficient $T(E)$ in a molecular junction for electrons (phonons) with energy E ($\hbar\omega$) traversing from one electrode to another. I then briefly discuss the master equation method to model transport in the Coulomb and Franck-Condon blockade regimes. I follow with a discussion

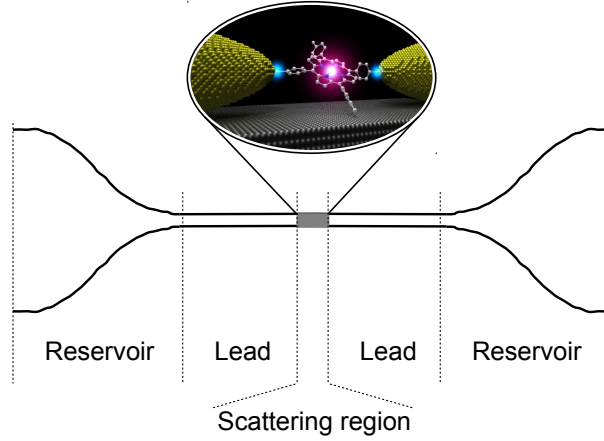


Figure 2.0.1: A scattering region is connected to the reservoirs through ballistic leads. Reservoirs have slightly different electrochemical potentials to drive electrons from the left to the right lead. All inelastic relaxation processes take place in the reservoirs and transport in the leads is ballistic.

about physical interpretation of a quantum system and different techniques used to model the experiment.

2.0.1 Schrödinger equation

The most general Schrödinger equation [2] describes the evolution of the physical properties of a system in time and was proposed by the Austrian physicist Erwin Schrödinger in 1926 as:

$$i\hbar \frac{\partial}{\partial t} \Psi(r,t) = \hat{H} \Psi(r,t) \quad (2.0.1)$$

where i is $\sqrt{-1}$, \hbar is the reduced Planck constant ($h/2\pi$), Ψ is the wave function of the quantum system, and \hat{H} is the Hamiltonian operator which characterizes the total energy of any given wave function. For a single particle moving in an electric field, the non-relativistic Schrödinger equation reads as:

$$i\hbar \frac{\partial}{\partial t} \Psi(r,t) = \left[\frac{-\hbar^2}{2m} \nabla^2 + V(r,t) \right] \Psi(r,t) \quad (2.0.2)$$

If we write the wavefunction as a product of spatial and temporal terms: $\Psi(r,t) = \psi(r)\theta(t)$, the Schrödinger equation becomes two ordinary differential equations:

$$\frac{1}{\theta(t)} \frac{d}{dt} \theta(t) = -\frac{iE}{\hbar} \quad (2.0.3)$$

and

$$\hat{H}\psi(r) = E\psi(r) \quad (2.0.4)$$

where $\hat{H} = \frac{-\hbar^2}{2m} \nabla^2 + V(r)$. The solution of equation 2.0.3 could be written as: $\theta(t) = e^{-iEt/\hbar}$. The amplitude of $\theta(t)$ does not change with time and therefore the solutions $\theta(t)$ are purely oscillatory. The total wave function

$$\Psi(r,t) = \psi(r)e^{-iEt/\hbar} \quad (2.0.5)$$

differs from $\psi(r)$ only by a phase factor of constant magnitude and the expectation value $|\Psi(r,t)|^2$ is time-independent. Of course 2.0.5 is a particular solution of time-dependent Schrödinger equation. The most general solution is a linear combination of these particular solutions as:

$$\Psi(r,t) = \sum_i \phi_i e^{-iE_i t/\hbar} \psi_i(r) \quad (2.0.6)$$

In time independent problems only the spatial part needs to be solved since the time dependent phase factor in 2.0.5 is always the same. Equation 2.0.4 is called time-independent Schrödinger equation and it is an eigenvalue problem where E 's are eigenvalues of the Hamiltonian \hat{H} . Since the Hamiltonian is a Hermitian operator, the eigenvalues E are real. $\psi(r)$ describes the standing wave solutions of the time-dependent equation, which are the states with definite energy called "stationary states" or "energy eigenstates" in physics and "atomic orbitals" or "molecular orbitals" in chemistry.

The Schrödinger equation must be solved subject to appropriate boundary conditions. Since the electrons are fermions, the solution must satisfy the Pauli exclusion principle and wavefunction ψ must be well behaved everywhere. The Schrödinger equation can be solved analytically for a few small systems such as the hydrogen atom. However, this is too complex to be solved in most cases even with the best supercomputers available today, so some approximations are needed. To describe the electronic properties of the system in this thesis I am going to use a series of the approximations [3] such as the Born-Oppenheimer approximation to decouple the movement of the electrons and the nuclei; density functional theory (DFT) to describe the electron - electron interactions and pseudopotentials to treat the nuclei and the core electrons except those in the valence band. These methods are well-known and are described in [3] and briefly discussed in the next section. In this thesis, I shall start from the DFT mean-field Hamiltonian or build a simple tight-binding Hamiltonian using Huckel parameters for the desired system and

use these to describe the transport through these systems.

To reduce the size of the Hamiltonian, it is appropriate to define the idea of the basis functions where

$$\Psi(r) = \sum_i \phi_i \psi_i(r) \quad (2.0.7)$$

The wavefunction then can be represented by a column vector $|\phi\rangle$ consisting of the expansion coefficients ϕ_i . The time-independent Schrödinger equation could be written as a matrix equation:

$$[H]|\phi\rangle = E[S]|\phi\rangle \quad (2.0.8)$$

where

$$S_{ij} = \langle i|j\rangle = \int dr \psi_j^*(r) \psi_i(r) \quad (2.0.9)$$

and

$$H_{ij} = \langle i|H|j\rangle = \int dr \psi_j^*(r) H \psi_i(r) \quad (2.0.10)$$

The evaluation of these integrals is the most time-consuming step, but once $[H]$ and $[S]$ are obtained, the eigenvalues E_n and eigenvectors ϕ_n are easily calculated. If $\langle i|$ and $|j\rangle$ are orthogonal then $S_{ij} = \delta_{ij}$ where δ_{ij} is the Kronecker delta ($\delta_{ij} = 1$ if $i = j$ and $\delta_{ij} = 0$ if $i \neq j$).

2.0.2 Density functional theory (DFT)

In order to understand the behaviour of molecular electronic devices, it is necessary to possess a reliable source of structural and electronic information. A solution to the many body problem has been sought by many generations of physicists. The task is to find the eigenvalues and eigenstates of the full Hamiltonian operator of a system consisting of nuclei and electrons as shown in figure 2.0.2. Since this is not practically possible for the systems bigger than a few particles, some approximations are needed. The atomic masses are roughly three orders of magnitudes bigger than the electron mass, hence the Born-Oppenheimer approximation [3] can be employed to decouple the electronic wave function and the motion of the nuclei. In other words we solve the Schrödinger equation for the electronic degrees of freedom only. Once we know the electronic structure of a system we can calculate classical forces on the nuclei and minimize these forces to find the ground-state geometry (figure 2.0.2a).

Once the Schrödinger equation was solved, the wavefunction is known and all physical quantities of interest could be calculated. Although the Born-Oppenheimer approximation decouples the electronic wave function and the motion of the nuclei, the electronic part of the problem has reduced to many interacting particles problem which even for modest system sizes i.e. a couple of atoms, its diagonalization is practically impossible even on a modern supercomputer. The virtue of density functional theory DFT [3, 4] is that it expresses the physical quantities in terms of the ground-state density and by obtaining the ground-state density, one can in principle calculate the ground-state energy. However, the exact form of the functional is not known. The kinetic term and internal energies of the interacting particles cannot generally be expressed as functionals of the density. The solution is introduced by Kohn and Sham in 1965. According to Kohn and Sham, the original Hamiltonian of the many body interacting system can be replaced by an effective Hamiltonian of non-interacting particles in an effective external potential, which has the same ground-state density as the original system as illustrated in figure 2.0.2a. The difference between the energy of the non-interacting and interacting system is referred to the exchange correlation functional (figure 2.0.2a).

Exchange and correlation energy: There are numerous proposed forms for the exchange and correlation energy V_{xc} in the literature [3, 4]. The first successful - and yet simple - form was the Local Density Approximation (LDA) [4], which depends only on the density and is therefore a local functional. Then the next step was the Generalized Gradient Approximation (GGA) [4], including the derivative of the density. It also contains information about the neighborhood and therefore is semi-local. LDA and GGA are the two most commonly used approximations to the exchange and correlation energies in density functional theory. There are also several other functionals, which go beyond LDA and GGA. Some of these functionals are tailored to fit specific needs of basis sets used in solving the Kohn-Sham equations and a large category are the so called hybrid functionals (eg. B3LYP, HSE and Meta hybrid GGA), which include exact exchange terms from Hartree-Fock. One of the latest and most universal functionals, the Van der Waals density functional (vdW-DF), contains non-local terms and has proven to be very accurate in systems where dispersion forces are important.

Pseudopotentials: Despite all simplifications shown in 2.0.2, in typical systems of molecules which contain many atoms, the calculation is still very large and has the potential to be computationally expensive. In order to reduce the number of electrons, one can introduce pseudopotentials which effectively remove the core electrons from an atom. The electrons in an atom can

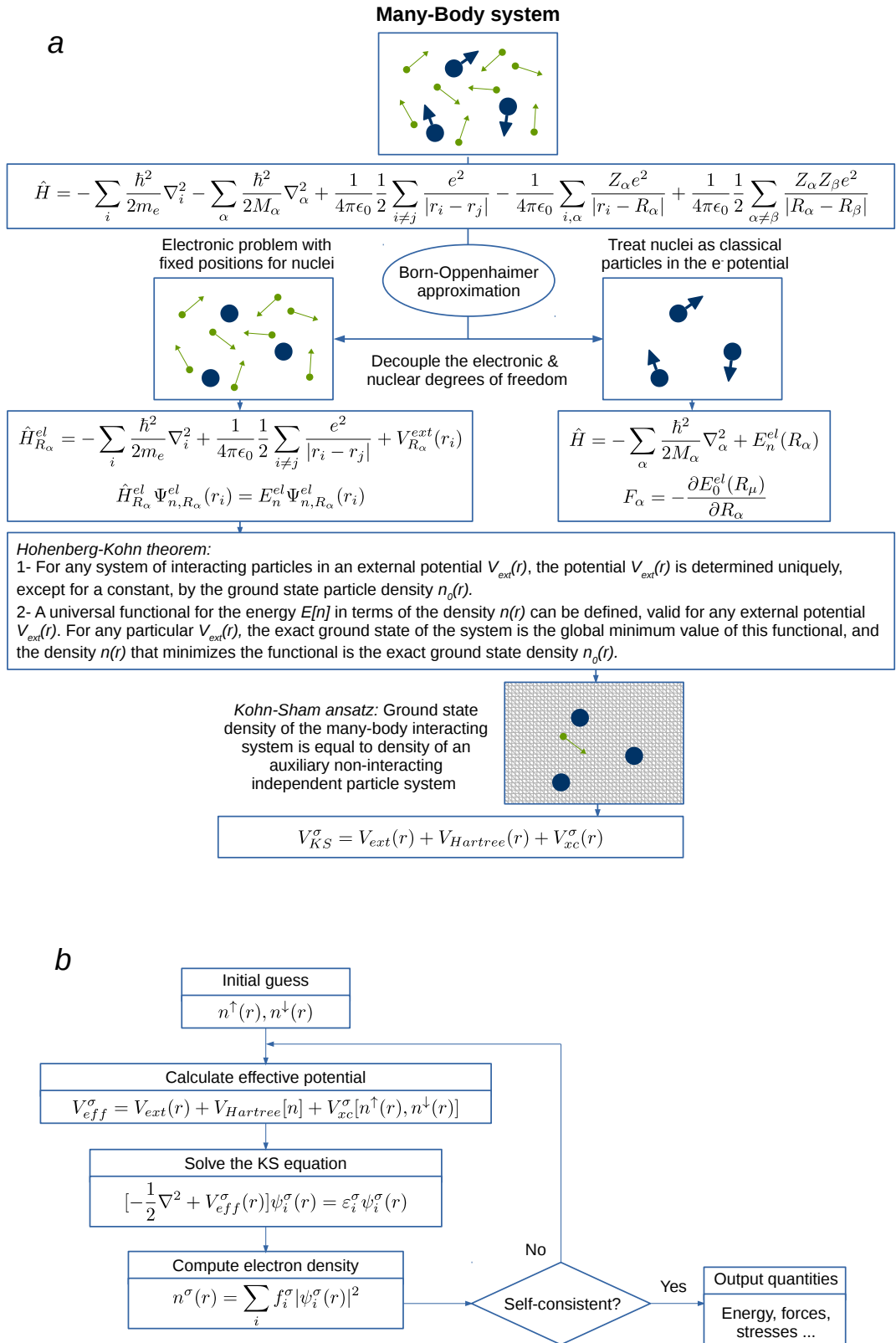


Figure 2.0.2: From many-body problem to density functional theory DFT. (a) Born-Oppenheimer approximation, Hohenberg-Kohn theorem and Kohn-Sham ansatz, (b) Schematic of the DFT self-consistency process.

be split into two types: core and valence, where core electrons lie within filled atomic shells and the valence electrons lie in partially filled shells. Together with the fact that core electrons are spatially localized about the nucleus, only valence electron states overlap when atoms are brought together so that in most systems only valence electrons contribute to the formation of molecular orbitals. This allows the core electrons to be removed and replaced by a pseudopotential such that the valence electrons still feel the same screened nucleon charge as if the core electrons were still present. This reduces the number of electrons in a system dramatically and in turn reduces the time and memory required to calculate properties of molecules that contain a large number of electrons. Another benefit of pseudopotentials is that they are smooth, leading to greater numerical stability.

Basis Sets: For a periodic system, the plane-wave basis set is natural since it is, by itself, periodic. However, since we need to construct a tight-binding Hamiltonian, we need to use localised basis sets discussed in the next section, which are not implicitly periodic. An example is a Linear Combination of Atomic Orbital (LCAO) basis set which are constrained to be zero after some defined cut-off radius, and are constructed from the orbitals of the atoms.

To obtain a ground state mean-field Hamiltonian from DFT, the calculation is started by constructing the initial atomic configuration of the system. Depending on the applied DFT implementation, the appropriate pseudopotentials for each element which can be different for every exchange-correlation functional might be needed. Furthermore, a suitable choice of the basis set has to be made for each element present in the calculation. The larger the basis set, the more accurate our calculation - and, of course, the longer it will take. With a couple of test calculations we can optimize the accuracy and computational cost. Other input parameters are also needed that set the accuracy of the calculation such as the fineness and density of the k -grid points used to evaluate the integral([4, 5]). Then an initial charge density assuming no interaction between atoms is calculated. Since the pseudopotentials are known this step is simple and the total charge density will be the sum of the atomic densities.

The self-consistent calculation [4](figure 2.0.2b) starts by calculating the Hartree potential and the exchange correlation potential. Since the density is represented in real space, the Hartree potential is obtained by solving the Poisson equation with the multi-grid or fast Fourier-transform method, and the exchange-correlation potential is obtained. Then the Kohn-Sham equations are solved and a new density is obtained. This self-consistent iterations end when the necessary convergence criteria are reached such as density matrix tolerance. Once the initial

electronic structure of a system obtained, the forces on the nuclei could be calculated and a new atomic configuration to minimize these forces obtained. New atomic configuration is new initial coordinate for self-consistent calculation. This structural optimization is controlled by the conjugate gradient method for finding the minimal ground state energy and the corresponding atomic configuration [4]. From the obtained ground state geometry of the system, the ground state electronic properties of the system such as total energy, binding energies between different part of the system, density of states, local density of states, forces, etc could be calculated. It is apparent that the DFT could potentially provide an accurate description of the ground state properties of a system such as total energy, binding energy and geometrical structures. However, DFT has not been originally designed to describe the excited state properties and therefore all electronic properties related to excited states are less accurate within DFT. If the LCAO basis is used, the Hamiltonian and overlap matrices used within the scattering calculation could be extracted.

2.0.3 Tight-Binding Model

By expanding the wavefunction over a finite set of the atomic orbitals, the Hamiltonian of the system can be written in a tight-binding model. The main idea is to represent the wave function of a particle as a linear combination of some known localized states. A typical choice is to consider a linear combination of atomic orbitals (LCAO). For a periodic system where the wavefunction is described by a Bloch function, equation 2.0.8 could be written as

$$\sum_{\beta,c'} H_{\alpha,c;\beta,c'} \phi_{\beta,c'} = E \sum_{\beta,c'} S_{\alpha,c;\beta,c'} \phi_{\beta,c'} \quad (2.0.11)$$

where c and c' are the neighbouring identical cells containing states α and

$$H_{\alpha,c;\beta,c'} = H_{\alpha,\beta}(R_c - R_{c'}) \quad (2.0.12)$$

and

$$\phi_{\beta,c} = \phi_{\beta} e^{ik \cdot R_c} \quad (2.0.13)$$

The equation 2.0.11 could be written as

$$\sum_{\beta} H_{\alpha\beta}(k)\phi_{\beta} = E \sum_{\beta} S_{\alpha\beta}(k)\phi_{\beta} \quad (2.0.14)$$

where

$$H_{\alpha\beta}(k) = \sum_{c'} H_{\alpha\beta}(R_c - R_{c'}) e^{ik(R_c - R_{c'})} \quad (2.0.15)$$

and

$$S_{\alpha\beta}(k) = \sum_{c'} S_{\alpha\beta}(R_c - R_{c'}) e^{ik(R_c - R_{c'})} \quad (2.0.16)$$

More generally, the single-particle tight-binding Hamiltonian in the Hilbert space formed by $|R_{\alpha}\rangle$ could be written as:

$$H = \sum_{\alpha} (\epsilon_{\alpha} + eV_{\alpha}) |\alpha\rangle\langle\alpha| + \sum_{\alpha\beta} \gamma_{\alpha\beta} |\alpha\rangle\langle\beta| \quad (2.0.17)$$

where ϵ_{α} is the corresponding on-site energy of the state $|\alpha\rangle$, V_{α} is the electrical potential and the $\gamma_{\alpha\beta}$ is the hopping matrix element between states $|\alpha\rangle$ and $|\beta\rangle$. For conjugated hydrocarbon systems, the energies of molecular orbitals associated with the pi electrons could be determined by a very simple LCAO molecular orbitals method called Huckel molecular orbital method (HMO). Therefore, a simple TB description of the system could be conduct just by assigning a Huckel parameter for on-site energy ϵ_{α} of each atom in the molecule connected to the nearest neighbours with a single Huckel parameter for hopping matrix element $\gamma_{\alpha\beta}$. Obviously, more complex TB models could be made using HMO by taking second, third, forth or more nearest neighbours hopping matrix element into account.

One dimensional (1D) infinite chain

As an example, a single-orbital orthogonal nearest neighbour tight binding Hamiltonian of an infinite linear chain of hydrogen atoms shown in figure 2.0.3 with on-site energy $\langle j|H|j\rangle = \epsilon_0$ and the hopping matrix element $\langle j|H|j\pm 1\rangle = \langle j\pm 1|H|j\rangle = -\gamma$ could be written as:

$$H = \sum_j \epsilon_0 |j\rangle\langle j| - \sum_{j,j+1} \gamma |j\rangle\langle j+1| - \sum_{j-1,j} \gamma |j-1\rangle\langle j| \quad (2.0.18)$$

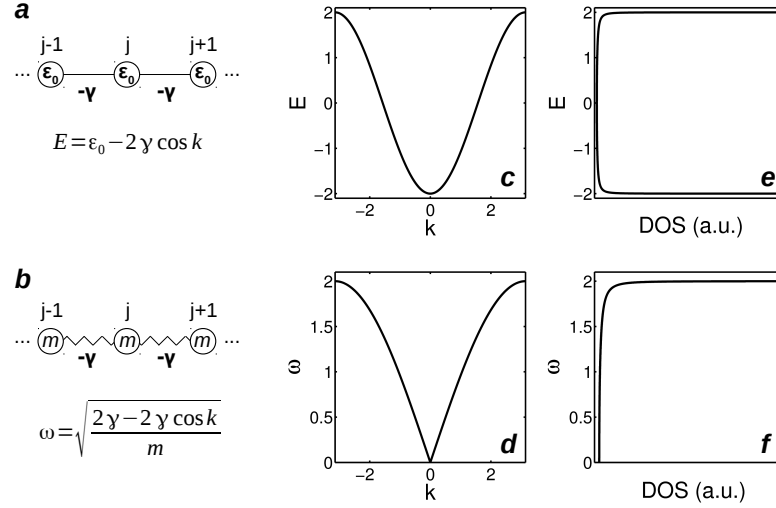


Figure 2.0.3: One dimensional (1D) infinite chain. (a) hydrogen atoms in an infinite chain with one orbital per atom, (b) 1D balls and springs, (c,d) electronic and phononic band structures and (e,f) density of states (DOS) for a and b.

Therefore the Schrödinger equation reads

$$\epsilon_0 \phi_j - \gamma \phi_{j-1} - \gamma \phi_{j+1} = E \phi_j \quad (2.0.19)$$

where $-\infty < j < +\infty$. The solution of this equation could be obtained using the Bloch function as

$$|\Psi_k\rangle = \frac{1}{\sqrt{N}} \sum_j e^{ikja_0} |j\rangle \quad (2.0.20)$$

and

$$E(k) = \epsilon_0 - 2\gamma \cos(ka_0) \quad (2.0.21)$$

where $-\pi/a_0 < k < \pi/a_0$ in the first Brillouin zone. Equation 2.0.21 is called a dispersion relation ($E - k$) or electronic bandstructure of a 1D chain. Since $-1 < \cos(ka_0) < 1$, hence $\epsilon_0 - 2\gamma < E < \epsilon_0 + 2\gamma$; therefore the bandwidth is 4γ . The density of states (DOS) could be calculated from:

$$D(E) = \sum_i \delta(E - \epsilon_i) \quad (2.0.22)$$

where ϵ_i is the eigenvalues of a system and δ is Kronecker delta. Figure 2.0.3a shows the band structure and density of states for a 1D chain.

I have yet discussed the electronic properties of a quantum system e.g. 1D chain. Now consider a chain of the atoms with mass m connected to each other with the springs with spring-constant $K = -\gamma$ as shown in figure 2.0.3. In one hand, the derivative of the energy with respect to the position of the atoms describe the forces in the system ($F = -\frac{\partial}{\partial x}U$). On the other hand, from Newton's second law $F = -m\frac{d^2x}{dt^2}$. Using the harmonic approximation method the Schrödinger-like equation could be written as:

$$-m\frac{d^2x_n}{dt^2} = -K[2x_n - x_{n-1} - x_{n+1}] \quad (2.0.23)$$

Similar to what was discussed above, using $x_n(t) = Ae^{i(kn-\omega t)}$, equation 2.0.23 reads $-m\omega^2 = -K[2 - e^{-ik} - e^{ik}]$ and therefore the phononic dispersion relation is obtained as

$$\omega(k) = \sqrt{\frac{2\gamma - 2\gamma\cos k}{m}} \quad (2.0.24)$$

Comparing the equation 2.0.21 and 2.0.24, it is apparent that the equation 2.0.24 could be written by changing the $E \rightarrow m\omega^2$ and $\epsilon_0 \rightarrow 2\gamma$ in the equation 2.0.21. $\epsilon_0 = 2\gamma$ is the negative of the sum of all off-diagonal terms of the 1D chain TB Hamiltonian in which make sense to satisfy translational invariance. The general Schrödinger equation for phonons could be written as

$$\omega^2\psi = D\psi \quad (2.0.25)$$

This is very similar to the equation 2.0.8, where $E \rightarrow \omega^2$, and the dynamical matrix $D = -K/M$ where M is the mass matrix, K_{ij} could be calculated from the force matrix and $K_{ii} = \sum_{i \neq j} K_{ij}$.

One dimensional (1D) finite chain and ring

To analyse the effect of the different boundary conditions in the solution of the Schrödinger equation, I consider three examples shown in figure 2.0.4. Consider a 1D finite chain of N atoms. As a consequence of introducing the boundary condition at the two ends of the chain, the energy levels and states are no longer (continuous) in the range of $\epsilon_0 - 2\gamma < E < \epsilon_0 + 2\gamma$; instead there are discrete energy levels and corresponding states in this range. The differences in the allowed energy levels between a 1D finite chain and a 1D ring demonstrates that small

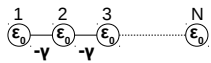
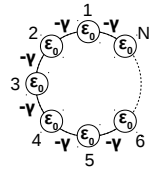
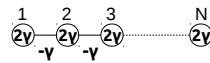
Electronic wave function and energy levels		Phononic modes
1D finite chain	1D ring	1D finite chain
		
$E = \epsilon_0 - 2\gamma \cos k$ $\psi_j = A \sin kj$ $A = \sqrt{\frac{2}{N+1}}$ $k = \frac{n\pi}{N+1} \quad n=1, \dots, N$	$E = \epsilon_0 - 2\gamma \cos k$ $\psi_j = A e^{ikj}$ $A = \frac{1}{\sqrt{N}}$ $k = \frac{2n\pi}{N} \quad n=0, \dots, N-1$	$\omega = \sqrt{\frac{2\gamma - 2\gamma \cos k}{m}}$ $\psi_j = A \cos k(j - \frac{1}{2})$ $A = 1/\sqrt{2N} \quad n \neq 0$ $A = 1/\sqrt{N} \quad n = 0$ $k = \frac{n\pi}{N} \quad n=1, \dots, N$

Figure 2.0.4: 1D finite chain and ring. The energy levels and corresponding wave functions or orbitals for a 1D finite chain and ring. The phononic mode for a finite chain of balls and springs with mass m .

changes in the system significantly affect the energy levels and corresponding orbitals. This is more important where few number of atoms investigated e.g. the molecules, so two very similar molecule could show different electronic properties.

Two dimensional (2D) square and hexagonal lattices

Using the TB Hamiltonian of a 1D chain, I calculated its band-structure and density of states. Now let's consider two most used 2D lattices: a square lattice where the unit-cell consist of one atom is connected to the first nearest neighbour in two dimensions (figure 2.0.5a) and a hexagonal lattice where a unit cell consist of two atoms is connected to the neighbouring cells in which first (second) atom in a cell is only connected to the second (first) atom in any first nearest neighbour cell (figure 2.0.5b). The TB Hamiltonian and corresponding band-structure could be calculated [1] using the equation 2.0.17 and the Bloch wave function has the form of $Ae^{ik_x j + ik_y l}$ as shown in figure 2.0.5.

Figures 2.0.5b,c,f,g show the bandstructure of square and hexagonal lattices. Furthermore, the number of conduction channels could be calculated as shown in figures 2.0.5d,h using the method described in section 2.1.4. The number of channels has a maximum in the middle of the band for a square lattice, whereas for a hexagonal lattice, there are fewer open channels (e.g. only two for graphene) in the middle of the band.

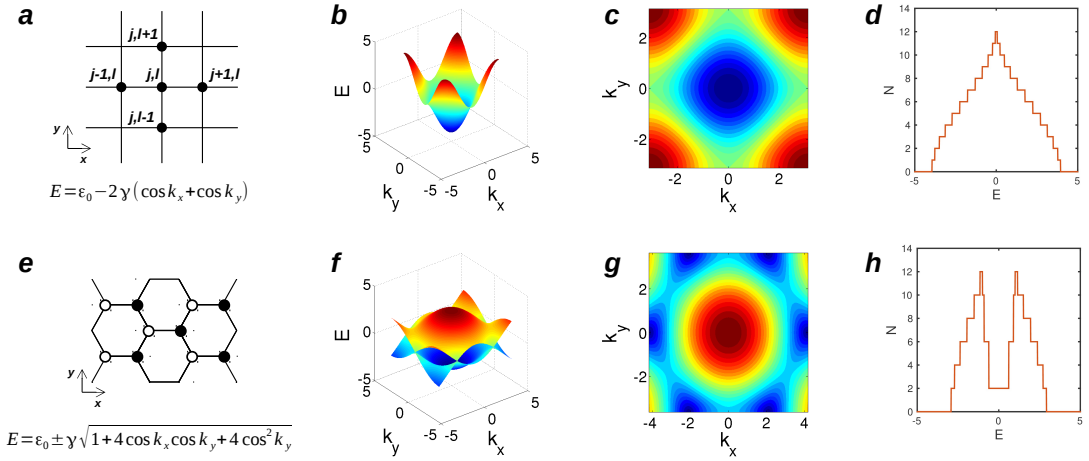


Figure 2.0.5: Two dimensional square and hexagonal lattices. Lattice geometry of (a) square and (e) hexagonal lattices, the bandstructure of (b,c) square and (f,g) hexagonal lattices and the number of conduction channels in (d) square and (h) hexagonal lattices.

2.0.4 Current carried by a Bloch function

The time evolution of the density matrix $\rho_t = |\psi_t\rangle\langle\psi_t|$ allows us to obtain current associated with a particular quantum state $|\psi_t\rangle$. Using the time-dependent Schrödinger equation 2.0.1, I define

$$I = \frac{d}{dt}|\psi_t\rangle\langle\psi_t| = \frac{1}{i\hbar}[H|\psi_t\rangle\langle\psi_t| - |\psi_t\rangle\langle\psi_t|H] \quad (2.0.26)$$

By expanding $|\psi_t\rangle$ over orthogonal basis $|j\rangle$ equation 2.0.26 could be written as:

$$\frac{d\rho_t}{dt} = \frac{1}{i\hbar}[\sum_{jj'} H|j\rangle\langle j'| \psi_j \psi_{j'}^* - \sum_{jj'} |j\rangle\langle j'| H \psi_j \psi_{j'}^*] \quad (2.0.27)$$

For a 1D infinite chain with the Hamiltonian of the form of 2.0.18, the rate of change of charge $I_l = d\rho_t^l/dt$ at site l could be obtained by calculating the expectation value of both side of 2.0.27 over the state $|l\rangle$

$$\frac{d\rho_t^l}{dt} = \frac{1}{i\hbar}[\sum_{jj'} \langle l|H|j\rangle\langle j'|l\rangle \psi_j \psi_{j'}^* - \sum_{jj'} \langle l|j\rangle\langle j'|H|l\rangle \psi_j \psi_{j'}^*] \quad (2.0.28)$$

which could be simplified as

$$\frac{d\rho_t^l}{dt} = I_{l+1 \rightarrow l} + I_{l-1 \rightarrow l} \quad (2.0.29)$$

where

$$I_{l+1 \rightarrow l} = -\frac{1}{i\hbar} [\langle l|H|l+1\rangle \psi_{l+1} \psi_l^* - \langle l+1|H|l\rangle \psi_l \psi_{l+1}^*] \quad (2.0.30)$$

and

$$I_{l-1 \rightarrow l} = -\frac{1}{i\hbar} [\langle l|H|l-1\rangle \psi_{l-1} \psi_l^* - \langle l-1|H|l\rangle \psi_l \psi_{l-1}^*] \quad (2.0.31)$$

The charge density is changing at atom site l as a result of two currents: right moving electrons $I_{l+1 \rightarrow l}$ and left moving electrons $I_{l-1 \rightarrow l}$. The corresponding current to a Bloch state $\psi_j(t) = e^{ikj - iE(k)t/\hbar}$ are:

$$I_{l+1 \rightarrow l} = -v_k \quad (2.0.32)$$

and

$$I_{l-1 \rightarrow l} = +v_k \quad (2.0.33)$$

where $v_k = \partial E(k)/\hbar \partial k = 2\gamma \sin(k)/\hbar$ is the group velocity. It is apparent that although the individual currents are non-zero proportional to the group velocity, the total current $I = I_{l+1 \rightarrow l} + I_{l-1 \rightarrow l}$ for a pure Bloch state is zero due to an exact balance between left and right going currents. It is worth to mention that to simplify the notation, a Bloch state e^{ikj} is often normalized with its current flux $1/\sqrt{v_k}$ calculated from equation 2.0.32 and 2.0.33 to obtain a unitary current. Hence I will mostly use a normalized Bloch state $e^{ikj}/\sqrt{v_k}$ in later derivations.

2.1 Transport on resonance and off resonance

Nanoscale transport can be described by three regimes:

(1) The self-consistent field (SCF) regime in which the thermal broadening $k_B T$ and coupling Γ to the electrodes are comparable to the Coulomb energy U_0 . The SCF method (single electron picture) implemented with NEGF could be used to describe transport in this regime as discussed in sections 2.1.1 to 2.1.5. In molecular junctions smaller than $\sim 3nm$, it is shown that the transport remain elastic and phase coherent at room temperature. Therefore, it is well accepted in the mesoscopic community to use SCF models to describe the properties of the molecular junctions. Based on a single electron picture and without taking into account the Coulomb energy, this NEGF method coupled to the SCF Hamiltonian describes the properties of the system on

and off resonances. Good agreement between these models and many room-temperature experiments suggest applicability of this method. A simplified Breit-Wigner formula derived from this method also could be used to model on-resonance transport through the device provided the level spacing is big compared with the resonances width. However, in those cases where the Coulomb energy has higher contribution, this method cannot describe the properties of the system on resonance.

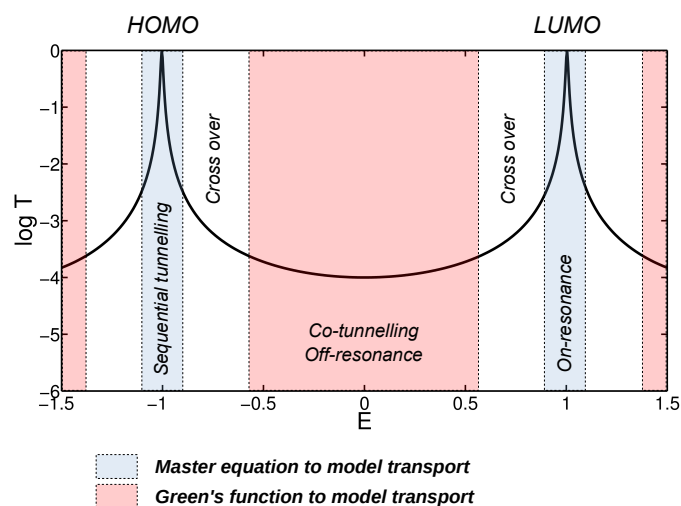


Figure 2.1.1: Transport on resonance and off resonance. The transport mechanism in a molecular junction could be either in tunnelling regime (off-resonance) where electrons tunnelled through the molecule modelled usually with NEGF, or on resonance where electrons are transmitted with high rate through a energy level modelled using master equation. The intermediate state (cross-over) between on and off resonance regimes are difficult to interpret either with NEGF or master equation.

(2) The Coulomb blockade (CB) regime in which Coulomb energy U_0 is much higher than both the thermal broadening $k_B T$ and coupling Γ where the SCF method is not adequate and the multi-electron master equation should be used to describe the properties of the system in this regime as discussed in section 2.1.6. This is needed usually to model the properties of molecular junctions at low temperature where an electrostatic gate voltage could be applied through back gate.

(3) The intermediate regime in which the Coulomb energy U_0 is comparable to the larger of the thermal broadening $k_B T$ and coupling Γ . There is no simple approach to model this regime. Neither the SCF method nor master equation could be used to well describe the transport in this regime because SCF method does not do justice to the charging, while the master equation does not do justice to the broadening.

2.1.1 Breit-Wigner formula (BWF)

In the SCF regime, provided the coupling to electrodes was weak enough where the level broadening on resonances due to the electrodes are small enough and the level spacing (differences between the eigenenergies of a quantum system) is large enough, the on resonance transmission coefficient T of the electrons with energy E through a molecule could be described by a Lorentzian function, via the Breit-Wigner formula [6]:

$$T(E) = \frac{4\Gamma_1\Gamma_2}{(E - \varepsilon_n)^2 + (\Gamma_1 + \Gamma_2)^2} \quad (2.1.1)$$

where Γ_1 and Γ_2 describe the coupling of the molecular orbital to the electrodes and $\varepsilon_n = E_n - \sigma$ is the eigenenergy E_n of the molecular orbital shifted slightly by an amount σ due to the coupling of the orbital to the electrodes. This formula shows that when the electron resonates with the molecular orbital (e.g. when $E = \varepsilon_n$), electron transmission is a maximum. The formula is valid when the energy E of the electron is close to an eigenenergy E_n of the isolated molecule, and if the level spacing of the isolated molecule is larger than $(\Gamma_1 + \Gamma_2)$. If $\Gamma_1 = \Gamma_2$ (a symmetric molecule attached symmetrically to identical leads), $T(E) = 1$ on resonance ($E = \varepsilon_n$).

If a bound state (e.g. a pendant group ε_p) is coupled (by coupling integral α) to a continuum of states, Fano resonances could occur. This could be modelled by considering $\varepsilon_n = \varepsilon_0 + \alpha^2/(E - \varepsilon_p)$ in BWF. At $E = \varepsilon_p$, the electron transmission is destroyed (the electron anti-resonates with the pendant orbital) and at $E = \varepsilon_n$, the electron transmission is resonated by ε_n . The level spacing between this resonance and antiresonance is proportional to α .

2.1.2 Scattering theory and non-equilibrium Green's function

Non-equilibrium Green's function method has been widely used in the literature to model electron and phonon transport in nano and molecular scale devices and has been successful to predict and explain different physical properties. The Green's function is a wave function in a specific point of the system due to an impulse source in another point. In other words, the Green's function is the impulse response of the Schrödinger equation. Therefore, a Green's function should naturally carry all information about wave-function evolution from one point to another in a system. In this thesis, I have used the standard Green's function methods to calculate the transport. I will discuss it briefly but more detail discussion could be found in [1, 7–9].

Figure 2.1.2 shows how the Green's function could be used to calculate the transmission and

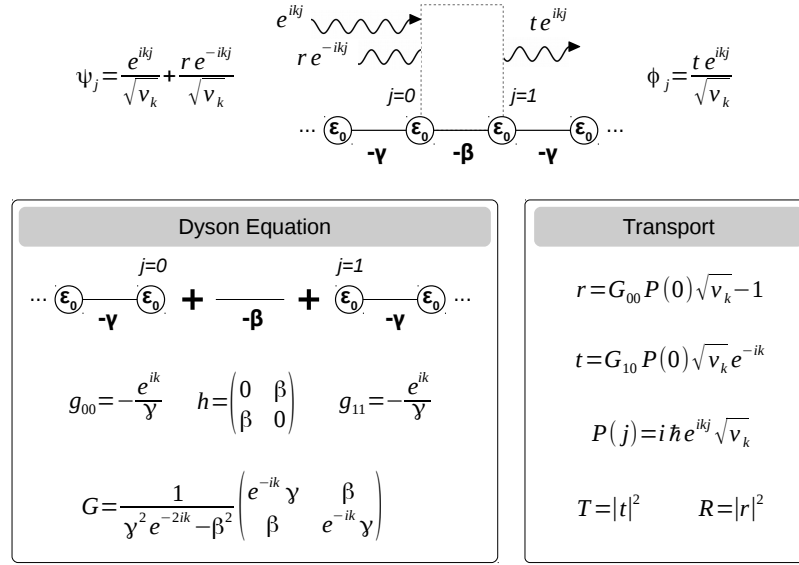


Figure 2.1.2: Transport through a scatter connected to two 1D leads. For a Bloch wave $e^{ikj}/\sqrt{v_k}$ incident with a barrier, the wave is transmitted with the amplitude of t ($t e^{ikj}/\sqrt{v_k}$) and reflected with the amplitude of r ($r e^{-ikj}/\sqrt{v_k}$). Using the surface Green's function of the leads (g_{00} and g_{11}), the Hamiltonian of the scattering region in which bridge two leads h and Dyson's equation, the total Green's function G could be calculated. The Green's function is the impulse response of the system and could be used to calculate the transmission t and reflection r amplitudes.

reflection amplitudes in a two terminal system where two semi-infinite crystalline 1D leads are connected to a scattering region. The main question is what are the amplitudes of the transmitted and reflected waves? There are two main steps, first to calculate the total Green's function matrix element between the site 0 and 1 (G_{10}) or 0 and 0 (G_{00}); and secondly project these to the wavefunction to calculate transmission t and reflection r amplitudes. The total transmission and reflection probabilities then could be calculated by

$$T = \sum_{ij} t_{ij} t_{ij}^* = Tr(tt^\dagger) \quad (2.1.2)$$

and

$$R = \sum_{ij} r_{ij} r_{ij}^* = Tr(rr^\dagger) \quad (2.1.3)$$

$t_{i,j}$ ($r_{i,j}$) is the transmission (reflection) amplitude describing scattering from the j th channel of the left lead to the i th channel of the right (same) lead. Scattering matrix S is defined from $\Psi_{OUT} = S\Psi_{IN}$ and could be written by combining reflection and transmission amplitudes as:

$$S = \begin{pmatrix} r & t' \\ t & r' \end{pmatrix} \quad (2.1.4)$$

The S matrix is a central object of *scattering theory* and charge conservation implies that the S matrix to be unitary: $SS^\dagger = I$.

As shown in figure 2.1.2, the total Green's function (first step) could be obtained using Dyson equation $G = (g^{-1} - h)^{-1}$ where the surface Green's functions of decoupled two semi infinite leads $g = \begin{pmatrix} g_{00} & 0 \\ 0 & g_{11} \end{pmatrix}$ and the Hamiltonian in which couples them together h are known. The second step is to calculate the projector which projects the Green's function in the leads

$$g = \sum_{jl} g_{jl} |j\rangle\langle l| = \sum_{jl} \frac{e^{ik|j-l|}}{i\hbar v_k} |j\rangle\langle l| \quad (2.1.5)$$

to the normalized wavefunction at site l (e^{ikl}). It could be shown that [7, 8], this projector $P(j)$ also projects the total Green's function G to the wavefunction ψ and therefore could be used to calculate t and r . Using this projector at site $j = 0$, $P(0)$ and G_{10} (G_{00}), the transmission (reflection) amplitude is obtained (see figure 2.1.2).

2.1.3 The Landauer Formula

Landauer used the *scattering theory of transport* as a conceptual framework to describe the electrical conductance and wrote "Conductance is transmission" [10]. In the Landauer approach a mesoscopic scatterer is connected to two ballistic leads (see figure 2.0.1). The leads are connected to the reservoirs where all inelastic relaxation processes take place. The reservoirs have slightly different electrochemical potentials $\mu_L - \mu_R \rightarrow 0$ to drive electrons from the left to the right lead. The current therefore could be written as:

$$I = \frac{e}{h} \int dE T(E) (f(E - \mu_L) - f(E - \mu_R)) \quad (2.1.6)$$

where e is the electronic charge, $T(E)$ is the transmission coefficient and f is Fermi-Dirac distribution function $f(E - \mu) = 1/(1 + e^{(E - \mu)/k_B T})$ associated with the electrochemical potential μ , k_B is Boltzmann constant and T is temperature. The Fermi functions can be Taylor expanded over the range eV ,

$$I = \frac{e}{h} \int dE T(E) \left(-\frac{\partial f(E)}{\partial E} \right) (\mu_L - \mu_R) \quad (2.1.7)$$

where $\mu_L - \mu_R = eV$. By including the spin, the electrical conductance $G = I/V$ reads as:

$$G = \frac{2e^2}{h} \int dE T(E) \left(-\frac{\partial f(E)}{\partial E} \right) \quad (2.1.8)$$

At $T = 0K$, $-\frac{\partial f(E-\mu)}{\partial E} = \delta(\mu)$ where $\delta(\mu)$ is the Kronecker delta. For an ideal periodic chain where $T(E) = 1$ at $T = 0K$, the Landauer formula becomes:

$$G_0 = \frac{2e^2}{h} \simeq 77.5 \mu \text{ Siemens} \quad (2.1.9)$$

G_0 is called the "Conductance Quantum". In other words, the current associated with a single Bloch state v_k/L and generated by the electrochemical potential gradient is $I = e(v_k/L)D\Delta\mu$ where the density of states $D = \partial n/\partial E = L/hv_k$. It is worth mentioning that the Landauer formula 2.1.7 describes the linear response conductance, hence it only holds for small bias voltages, $\delta V \rightarrow 0$.

Landauer-Buttiker formula for multi-terminal structures

Conductance measurements are often performed using a four-probe structure to minimize the contact resistance effect. Also multi-probe structures are widely used to describe the Hall-effect or in sensing applications. Based on the Landauer approach for two terminal system, Buttiker [11] suggested a formula to model multi-probe currents for structures with multiple terminals as:

$$I_i = \frac{e}{h} \sum_j T_{ij} (\mu_i - \mu_j) \quad (2.1.10)$$

where I_i is the current at i th terminal and T_{ij} is the transmission probability from terminal j to i . In a multi-terminal system, it is consistent to assume one of the probes as reference voltage $V_{ref} = 0$ and write the currents based on that. As an example, for a four probe structure, the current in each probe could be written as:

$$\begin{pmatrix} I_1 \\ I_2 \\ I_3 \\ I_4 \end{pmatrix} = \frac{2e^2}{h} \begin{pmatrix} N_1 - T_{11} & -T_{12} & -T_{13} & -T_{14} \\ -T_{21} & N_2 - T_{22} & -T_{23} & -T_{24} \\ -T_{31} & -T_{32} & N_3 - T_{33} & -T_{34} \\ -T_{41} & -T_{42} & -T_{43} & N_4 - T_{44} \end{pmatrix} \begin{pmatrix} V_1 \\ V_2 \\ V_3 \\ V_4 \end{pmatrix} \quad (2.1.11)$$

where N_i is number of open conduction channels in lead i . In a four probe structure, if probe 3 and 4 are outer voltage probes ($I_3 = I_4 = 0$) and probe 1 and 2 are the inner current probes, the four probe conductance is $G_{four-probe} = (2e^2/h)(V_3 - V_4)/I_1$.

2.1.4 Generalized model to calculate T(E)

In this section, I would like to discuss the generalized approach to calculate the transmission coefficient T of the electrons (phonons) with energy E ($\hbar\omega$) passing from one electrode to another using non-equilibrium Green's function method. Consider a quantum structure connected to ideal, normal leads of constant cross-section, labelled $L = 1, 2, \dots$ and therefore begin by considering two vector spaces A (representing the normal leads) and B (representing the structure of interest), spanned by a countable set of basis functions. For a system with an orthogonal basis set where the overlap matrix is unitary matrix I , the expression for the transmission coefficient $T_{nn'}$ between two scattering channels n, n' of an open vector space A , in contact with a closed sub-space B could be written as [7]:

$$T_{nn'} = |t_{n,n'}(E, H)|^2 \quad (2.1.12)$$

As shown in figure 2.1.3, the transmission amplitudes could be written [7] using the surface Green's function in the leads A and the Green's function of the scattering region B coupled to the outside world through coupling matrix elements H_1 .

$$t_{nn'} = i\hbar\sqrt{v_n}\sqrt{v_{n'}}\langle n|gWG_{BB}W^\dagger g|n'\rangle \quad (2.1.13)$$

or more precisely

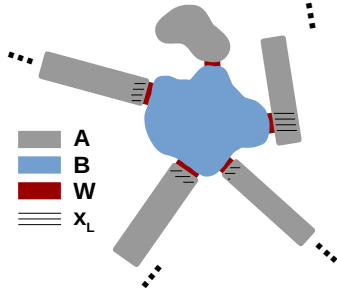
$$t_{nn'} = i\hbar\sqrt{v_n}\sqrt{v_{n'}}\sum_{x,x'} g_n(x_n, x)\langle n, x|WG_{BB}W^\dagger|n', x'\rangle g_{n'}(x', x_{n'}) \quad (2.1.14)$$

where

$$(G_{BB}^{-1})_{\mu\nu} = (E - \varepsilon_\nu)\delta_{\mu\nu} - \Sigma_{\mu\nu} + i\Gamma_{\mu\nu}, \quad (2.1.15)$$

and

$$g_n(x, x') = \frac{e^{ik_x^n|x-x'|} - e^{-ik_x^n(x+x'-2(x_L+a))}}{i\hbar v_n} \quad (2.1.16)$$



$$H = H_A + H_B + H_1 \quad H_1 = \begin{pmatrix} 0 & W \\ W^\dagger & 0 \end{pmatrix}$$

Green's function (GF)

$$g = \begin{pmatrix} g_A & 0 \\ 0 & g_B \end{pmatrix} \quad G = \begin{pmatrix} G_{AA} & G_{AB} \\ G_{BA} & G_{BB} \end{pmatrix}$$

decoupled system coupled system

Dyson equation to calculate GF of coupled system using GF of decoupled system and H_1	$G = g(1 - H_1g)^{-1}$ $G_{AA} = g_A(1 - Wg_BW^\dagger g_A)^{-1}, \quad G_{BB} = g_B(1 - W^\dagger g_A W g_B)^{-1}$ $G_{AB} = g_A(1 - Wg_BW^\dagger g_A)^{-1}Wg_B, \quad G_{BA} = g_B(1 - W^\dagger g_A W g_B)^{-1}W^\dagger g_A$
rewrite G_{AA}, G_{AB}, G_{BA} in terms of G_{BB}	$G_{AA} = g_A + g_A W G_{BB} W^\dagger g_A, \quad G_{AB} = g_A W G_{BB}, \quad G_{BA} = G_{BB} W^\dagger g_A$
write g in terms of sub-set of states $ \bar{n}\rangle = \bar{n}, x\rangle$ associate with open (n) and close (\bar{n}) channels of leads	$g_A = \sum_{n,x,x'} n,x\rangle g_n(x,x') \langle n,x' + \sum_{\bar{n}\bar{m}} \bar{n}\rangle g_{\bar{n}\bar{m}} \langle \bar{m} $ <p>Surface GF: $g_n(x_L, x_L) = g_n$</p> $g_n(x, x') = \frac{1}{i\hbar v_n} (e^{ik_x^n x-x' } - e^{-ik_x^n (x+x'-2(x_L+a))})$ $g_n(x, x_n) g_n^*(x', x_n) = \frac{-2}{\hbar v_n} \text{Im} g_n(x, x') = \frac{-2}{\hbar v_n} \text{Im} g_n(x', x)$
Transmission amplitude t	$t = i\hbar\sqrt{v_n}\sqrt{v'_n} \langle n, x_n G_{AA} n', x_{n'} \rangle,$ $t^\dagger = -i\hbar\sqrt{v_n}\sqrt{v'_n} \langle n, \bar{x}_n G_{AA} n', \bar{x}_{n'} \rangle^*$ $t = i\hbar\sqrt{v_n}\sqrt{v'_n} \sum_{x,x'} g_n(x_n, x) \langle n, x W G_{BB} W^\dagger n', x' \rangle g_{n'}(x', x_{n'})$
$H_B f_\nu\rangle = \epsilon_\nu f_\nu\rangle$ To calculate G_{BB}	$(G_{BB}^{-1})_{\mu\nu} = (E - \epsilon_\nu)\delta_{\mu\nu} - \Sigma_{\mu\nu} + i\Gamma_{\mu\nu}, \quad \Sigma_{\mu\nu} = \sigma_{\mu\nu} + \sigma'_{\mu\nu}$ $\sigma'_{\mu\nu} = \sum_{\bar{n}\bar{m}} \langle f_\mu W^\dagger \bar{n} \rangle g_{\bar{n}\bar{m}} \langle \bar{m} W f_\nu \rangle$ $\sigma_{\mu\nu} = \sum_n \sum_{x,x'} \langle f_\mu W^\dagger n, x \rangle [\text{Re } g_n(x, x')] \langle n, x' W f_\nu \rangle$ $\Gamma_{\mu\nu}(n) = - \sum_n \sum_{x,x'} \langle f_\mu W^\dagger n, x \rangle [\text{Im } g_n(x, x')] \langle n, x' W f_\nu \rangle$
Transmission coefficient	$T_{nn'} = t_{nn'} ^2$

Figure 2.1.3: Generalized transport model using Non-equilibrium Green's function method[7].

is the Green's function of the semi-infinite lead between any position point x and x' in the transport direction terminated at $x = x_L$ and vanishes at $x = x_L + a$. k_x^n is the longitudinal wavevector of channel n . If the lead belonging to channel n terminates at $x = x_L$, then on the surface of the lead, the Green's function $g_n(x, x')$ takes the form $g_n(x_L, x_L) = g_n$, where $g_n = a_n + ib_n$ with a_n real and b_n equal to π times the density of states per unit length of channel n . Moreover, if v_n is the group velocity for a wavepacket travelling along channel n , then $\hbar v_n = 2b_n/|g_n|^2$. It is interesting to note that if x and x' are positions located between x_L and some point x_n ,

$$g_n(x, x_n)g_n^*(x', x_n) = \frac{-2}{\hbar v_n} \text{Im}g_n(x, x') = \frac{-2}{\hbar v_n} \text{Im}g_n(x', x) \quad (2.1.17)$$

The eigenvalue and eigenvectors associated with the Hamiltonian of the B is obtained from the Schrödinger equation $H_B|f_\nu\rangle = \epsilon_\nu|f_\nu\rangle$. The self-energies Σ and broadening Γ then could be written as [7]:

$$\Sigma_{\mu\nu} = \sum_n \sum_{x, x'} \langle f_\mu | W^\dagger | n, x \rangle [\text{Re} g_n(x, x')] \langle n, x' | W | f_\nu \rangle + \sum_{\bar{n}\bar{m}} \langle f_\mu | W^\dagger | \bar{n} \rangle g_{\bar{n}\bar{m}} \langle \bar{m} | W | f_\nu \rangle \quad (2.1.18)$$

and

$$\Gamma_{\mu\nu}(n) = - \sum_n \sum_{x, x'} \langle f_\mu | W^\dagger | n, x \rangle [\text{Im} g_n(x, x')] \langle n, x' | W | f_\nu \rangle \quad (2.1.19)$$

This is very general and makes no assumptions about the presence or otherwise of resonances. For a system with non-orthogonal basis states, in equation 2.1.15 $\delta_{\mu\nu}$ should be replaced with the overlap matrix $S_{\mu\nu} = \langle f_\mu | f_\nu \rangle$. It is interesting to note that the vector spaces A representing the normal leads include both crystalline structures connected to the outside world and any close system coupled to the vector spaces B representing the structure of interest. In the latter case, the only effect of the closed part of the vector spaces A is to contribute in the scattering by its self-energy. The physical meaning of this and where it could be useful are discussed more in the next section. Furthermore, figure 2.1.4 shows a slightly different approach to calculate the transmission (reflection) amplitude t (r) in a two terminal system with non-orthogonal basis set derived in [8]. For better understanding, as well as the most general approach a simplified specific case for a one dimensional lead connected to an arbitrary scattering region is also included in this figure.

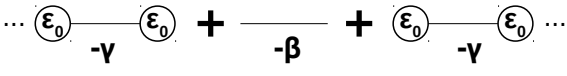
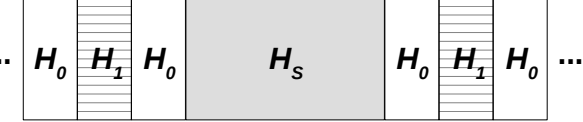
	1-dimensional	Generalized		
	<p>1-dimensional</p> 	<p>Generalized</p> 		
Band-structure	$E = \varepsilon_0 - 2\gamma \cos k$	$\det(H_0 + H_1 e^{ik} + H_1^\dagger e^{-ik} - E) = 0$		
Group velocity	$v_k = \frac{1}{\hbar} \frac{\partial E}{\partial k} = \hbar^{-1} 2\gamma \sin k$	$v_k = \frac{1}{\hbar} \frac{\partial}{\partial k} \langle \psi_k H \psi_k \rangle = \frac{i}{\hbar} \phi_k^\dagger (H_1 e^{ik} - H_1^\dagger e^{-ik}) \phi_k$		
Green's function (GF) of the doubly infinite system	$g_{x,x'} = \sum_{x,x'} \frac{e^{ik x-x' }}{i\hbar v_k} x\rangle \langle x' $	$g_{x,x'} = \begin{cases} \sum_{m=1}^M \phi_{k_m} e^{ik_m(x-x')} \phi_{k_m}^\dagger V^{-1} & x \geq x' \\ \sum_{m=1}^M \phi_{-k_m} e^{-ik_m(x-x')} \phi_{-k_m}^\dagger V^{-1} & x \leq x' \end{cases}$ $V = \sum_{l=1}^M H_1^\dagger (\phi_{k_m} e^{-ik_m} \phi_{k_m}^\dagger - \phi_{-k_m} e^{ik_m} \phi_{-k_m}^\dagger)$		
Subtract Δ from g to obtain surface GF in the left and right leads	$\Delta_x(x', x_0) = -\frac{e^{-ik(x-2x_0+x')}}{i\hbar v_k}$	$\Delta_x(x', x_0) = \sum_{m,n=1}^M \phi_{k_n} e^{ik_n(x-x_0)} \phi_{k_n}^\dagger \phi_{-k_m} e^{-ik_m(x_0-x')} \phi_{k_m}^\dagger V^{-1}$		
	$g_{l,l} = -\frac{e^{ik}}{\gamma}$	$g_L = (I - \sum_{m,n} \phi_{-k_n} e^{ik_n} \phi_{-k_n}^\dagger \phi_{k_m} e^{ik_m} \phi_{k_m}^\dagger) V^{-1}$ $g_R = (I - \sum_{m,n} \phi_{k_n} e^{ik_n} \phi_{k_n}^\dagger \phi_{-k_m} e^{-ik_m} \phi_{-k_m}^\dagger) V^{-1}$		
Use Dyson eq. to find GF of whole system including leads and scattering H	$G = \begin{pmatrix} -\gamma e^{-ik} & \beta \\ \beta & -\gamma e^{-ik} \end{pmatrix}^{-1}$	$G(E) = (g(E)^{-1} - H)^{-1} \quad g(E) = \begin{pmatrix} g_L & 0 \\ 0 & g_R \end{pmatrix}$		
Transmission and reflection amplitudes	$t = i v_k G_{10} e^{-ik}$ $r = i v_k G_{00} - 1$	$t_{nm} = \phi_{k_n}^\dagger G_{L0} V \phi_{k_m} \sqrt{\frac{v_{k_n}}{v_{k_m}}} e^{-ik_n L}$ $r_{nm} = \phi_{-k_n}^\dagger (G_{00} V - I) \phi_{k_m} \sqrt{\frac{v_{k_n}}{v_{k_m}}}$		
Number of open propagating channels in lead l	1	<i>left</i>	<i>right</i>	
		<i>Decaying</i>	$Im(k_l) > 0$	$Im(k_l) < 0$
		<i>Propagating</i>	$Im(k_l) = 0, v_{k_l} < 0$	$Im(k_l) = 0, v_{k_l} > 0$

Figure 2.1.4: Generalized transport model using Green's function method. Generalized transport model using equilibrium Green's function method [8] and its equivalent model for a simple 1D problem.

2.1.5 Equilibrium vs. non-equilibrium I-V

There are the terms usually used in the literature such as elastic vs. inelastic processes, coherent vs. incoherent regime or equilibrium vs. non-equilibrium Green's function method. The average distance that an electron (or a hole) travels before changing its momentum (energy) called elastic (inelastic) mean free path. For a junction with the length smaller than elastic (or inelastic) mean free path the process is assumed to be ballistic. These definition are well accepted in the mesoscopic community. However, the equilibrium and non-equilibrium process are defined differently in the literature. The view I adopt in this thesis is to call any process where the current is derived from any differences in the electrochemical potential whether small or big is called non-equilibrium condition. To calculate the current using Landauer formula (equation 2.1.6), one needs to bear in mind that the Landauer formula only holds in the linear response regime for a transmission coefficient T which describes the transmission probability of particle with energy E from one electrode to another calculated in steady state condition and assuming the junction is close to equilibrium ($\delta V \rightarrow 0$). However, for the non-linear regime where the voltage condition is big, the transmission coefficient T could be a function of bias voltages V_b . The potential profile applied to the junction due to a given electric field caused by bias voltage should be calculated by Poisson's equation [1]. In the non-equilibrium condition, the Landauer formula then takes the form,

$$I(V_b, V_g) = \frac{e}{h} \int dE T(E, V_b, V_g) \left(f(E + \frac{eV_b}{2}) - f(E - \frac{eV_b}{2}) \right) \quad (2.1.20)$$

It is worth mentioning that in some experiments due to very noisy measured conductance spectrum $G = I/V_b$, the differential conductance map $G_{diff}(V_b, V_g) = dI(V_b, V_g)/dV_b$ is plotted which could be calculated by differentiation of equation 2.1.20 with respect to the bias voltage V_b .

Another interesting point is how to interpret transport in a nano and molecular scale junctions physically. If $ES|\psi\rangle = H|\psi\rangle$ describes the properties of the closed system H with non-orthogonal basis set S , then once it connects to the outside world and became an open system (see figure 2.1.5), the modified Schrödinger equation in non-equilibrium condition could be written [1]:

$$ES|\psi\rangle = H|\psi\rangle + \Sigma|\psi\rangle + |s\rangle \quad (2.1.21)$$

where the terms $\Sigma|\psi\rangle$ and $|s\rangle$ describe the outflow and inflow, respectively arises from the bound-

ary conditions. Equation 2.1.21 could be rewritten as

$$|\psi\rangle = [G^R]|s\rangle \quad (2.1.22)$$

where $G^R = [ES - H - \Sigma]^{-1}$ is retarded Green's function ($G^A = [G^R]^\dagger$), $\Sigma = \Sigma_1 + \Sigma_2 + \Sigma_0$ is self-energies due to the electrodes Σ_1 , Σ_2 , and surroundings Σ_0 such as dephasing contact or inelastic scattering e.g. electron-phonon coupling, emission, absorption, etc. Dephasing contact terms could be described by SCF method whereas for inelastic processes one needs to use for instance Fermi's golden rule to describe these self energies. There are some disagreement in

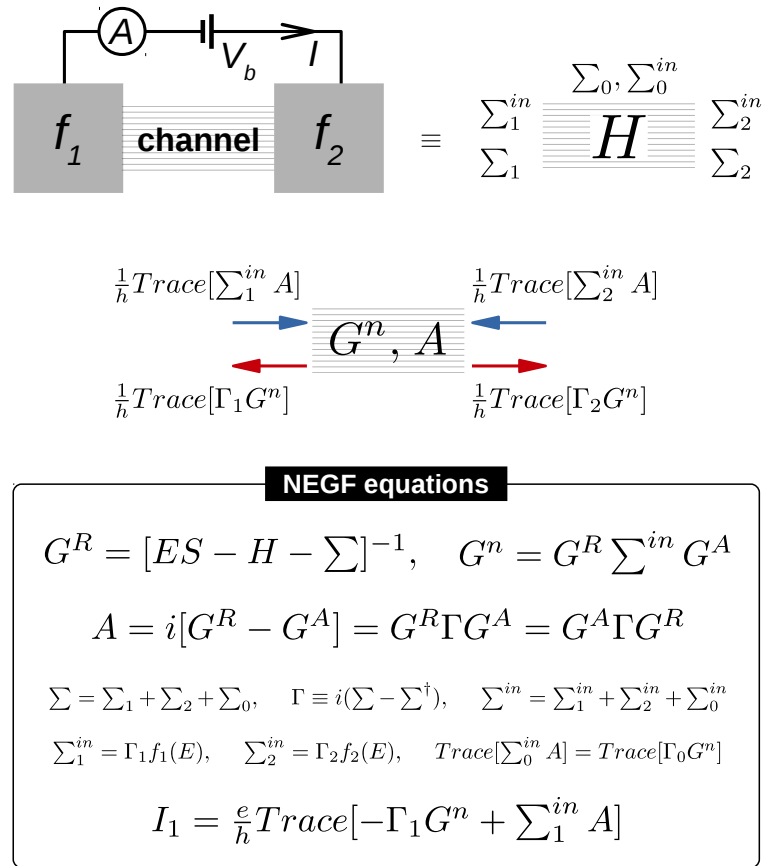


Figure 2.1.5: Non-equilibrium Green's function (NEGF) equations.

the literature about how to treat incoherent and inelastic processes [1, 12]. Buttiker's [12] view is to treat the inelastic and incoherent scattering by introducing a new electrode to the original coherent system. This could be seen as assigning the new self-energies associated with any inelastic or incoherent process. However, Datta has slightly different view. If you treat the incoherent and inelastic effect by introducing an extra electrode, you assign a corresponding distribution function e.g. Fermi function for electrons which in general may not be the case.

More generally, you could introduce any incoherence and/or inelastic process by appropriate self energy which not necessarily described by equivalent Fermi function in the contact.

For a normal, coherent elastic junction if $H_{1,2}$ are the coupling matrices between electrode 1 (2) and scattering region and $g_{1,2}$ are the surface Green's function of the electrodes, $\Sigma_{1,2} = H_{1,2}^\dagger g_{1,2} H_{1,2}$. Furthermore, the current could be calculated as $I_1 = \frac{e}{h} \text{Trace}[-\Gamma_1 G^n + \Sigma_1^{in} A]$ where Γ_1 , G^n , Σ_1^{in} and A defined in figure 2.1.5. From the basic law of equilibrium, in a special situation where we have only one contact connected; the ratio of the number of electrons to the number of states must be equal to the Fermi function in the contact ($\Sigma_{1,2}^{in} = \Gamma_{1,2} f_{1,2}(E)$). However, in dephasing contact, Σ_0^{in} is not described by any Fermi function and since inflow and outflow should be equal $\text{Trace}[\Sigma_0^{in} A] = \text{Trace}[\Gamma_0 G^n]$. Figure 2.1.5 summarize the basic non-equilibrium Green's function (NEGF) equations to calculate the current in a most general junction where surroundings presents. In the absence of surroundings, current in lead i could be written as [1]:

$$I_i = \frac{e}{h} \sum_j \text{Trace}[\Gamma_i G^R \Gamma_j G^A] (f_i - f_j) \quad (2.1.23)$$

where $T_{ij}(E) = \text{Trace}[\Gamma_i(E) G^R(E) \Gamma_j(E) G^A(E)]$ is the transmission coefficient for electrons with energy E passing from lead i to lead j . Consider two identical 1D leads with on-site

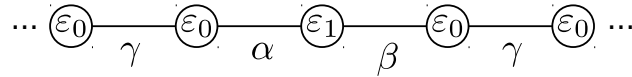


Figure 2.1.6: Two terminal system with two 1D leads connected to a scattering region ϵ_1 .

energies ϵ_0 and hopping integrals γ connected to a scattering region ϵ_1 with coupling integrals α and β as shown in figure 2.1.6. The transmission coefficient T for electrons with energy E traversing from left to right lead can be calculated as

$$T(E) = \Gamma_L(E) G^R(E) \Gamma_R(E) G^A(E) \quad (2.1.24)$$

where the retarded Green's function is $G^R(E) = (E - \epsilon_1 - \Sigma)$, the self-energies $\Sigma = \Sigma_L + \Sigma_R$ obtained from $\Sigma_L = \alpha^2 e^{ik} / \gamma$ and $\Sigma_R = \beta^2 e^{ik} / \gamma$ and the broadening due to the left and right leads are $\Gamma_L = i(\Sigma_L - \Sigma_L^\dagger) = -2\alpha^2 \sin(k) / \gamma$ and $\Gamma_R = i(\Sigma_R - \Sigma_R^\dagger) = -2\beta^2 \sin(k) / \gamma$.

2.1.6 Master equation

In the multi-electron picture, the overall system has different probabilities P_α of being in one of the 2^N possible states α . Furthermore all of these probabilities P_α must add up to one. The individual probabilities could be calculated under steady-state conditions where there is no net flow into or out of any state (see figures 2.1.7 and 2.1.8)

$$\sum_{\beta} R(\alpha \rightarrow \beta)P_\alpha = \sum_{\beta} R(\beta \rightarrow \alpha)P_\beta \quad (2.1.25)$$

where $R(\alpha \rightarrow \beta)$ is the rate constants obtained by assuming a specific model for the interaction with the surroundings. In a system that the electrons can only enter or exit from the source and drain contacts, these rates are given in figures 2.1.7 and 2.1.8 for one and two level systems. This equation is called a multi-electron master equation [1].

One level system

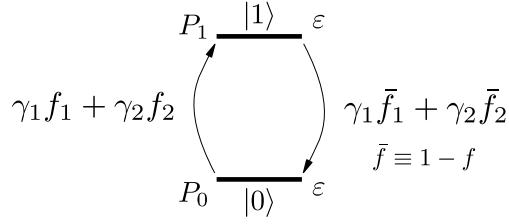
One-electron energy levels represent differences between energy levels corresponding to states that differ by one electron. If $E(N)$ is the energy associated with the N -electron state, the energy associated with the addition (removal) of one electron are called affinity (ionization) energy.

$$\begin{aligned} IP &= E(N-1) - E(N), \\ EA &= E(N) - E(N+1) \end{aligned} \quad (2.1.26)$$

The energy-gap E_g of a molecule (sometimes called additional energy) could be calculated from IP and EA as: $E_g = IP - EA$ [1]. The important conceptual point is that the electrochemical potential μ should lie between the affinity levels (above μ) and ionization levels (below μ). Figure 2.1.7 shows the master equation for spin-degenerate one level system with energy ϵ where there are only two possibilities, either the state is full $|1\rangle$ or empty $|0\rangle$. The current then could be calculated as:

$$I = \frac{e}{\hbar} \frac{\gamma_1 \gamma_2}{\gamma_1 + \gamma_2} (f_1(E) - f_2(E)) \quad (2.1.27)$$

where γ_1 and γ_2 are the rates electron can go in and out from the left and right electrodes with $f_1(E)$ and $f_2(E)$ Fermi functions.



Master equation	$P_0(\gamma_1 f_1 + \gamma_2 f_2) = P_1(\gamma_1 \bar{f}_1 + \gamma_2 \bar{f}_2)$
Energy conservation	$\sum_n P_n = 1 \quad P_1 = \frac{\gamma_1 f_1 + \gamma_2 f_2}{\gamma_1 + \gamma_2}$
Number of electrons	$N = P_1 \times 1 + P_0 \times 0 = P_1$
Current	$I = \frac{e}{\hbar} \frac{\gamma_1 \gamma_2}{\gamma_1 + \gamma_2} (f_1(\varepsilon) - f_2(\varepsilon))$

Figure 2.1.7: One level system.

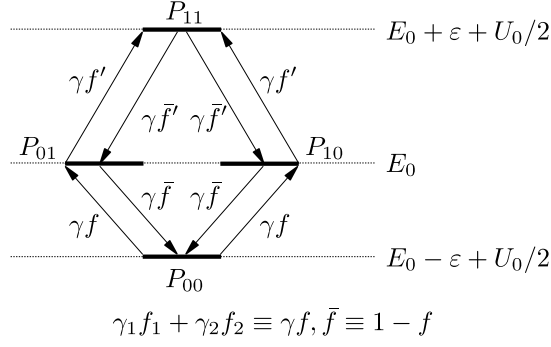
Two level system

However, in two level system there are four possibilities, both empty $|00\rangle$ or full $|11\rangle$ and either one of them full and another empty ($|01\rangle$ and $|10\rangle$). Figure 2.1.8 shows the obtained current for two level system [1]. The crucial point here is that, as soon as one state is full, there need an additional energy (Coulomb repulsion energy) to have second electron in the another state in addition to the level spacing energy. Another conceptual point is, it is incorrect to assume one Fermi function for all transitions. Due to the Coulomb blockade energy, each level needs certain electrochemical potential to overcome the barrier and current flow.

Coulomb and Franck-Condon blockade regimes

The electronic properties of weakly coupled molecules are dominated by Coulomb interactions and spatial confinement at low temperatures. This could lead to Coulomb blockade (CB) regimes in which the channel is blocked due to the presence of an electron trapped in the channel. In addition, charge transfer can excite vibrational modes or vibrons, and strong electron-vibron coupling leads to suppression of tunnel current at low bias called Franck-Condon (FC) blockade regimes.

To describe the transport in this regime, a minimal model (the Anderson-Holstein Hamiltonian) could be used [13] that captures the CB, FC and the Kondo effect if three assumptions are made: (1) the relaxation in the leads assumed to be sufficiently fast leading to Fermi func-



Master equation	$\sum_{\beta} R(\alpha \rightarrow \beta) P_{\alpha} = \sum_{\beta} R(\beta \rightarrow \alpha) P_{\beta} \quad \sum_n P_n = 1$
Number of electrons in system	$N = \sum_{\alpha} N_{\alpha} P_{\alpha}$
Current	$I_1 = -e \sum_{\beta} c R_1(\alpha \rightarrow \beta) P_{\alpha}, \quad c = \begin{cases} +1 & \text{if } N^{\beta} = 1 + N^{\alpha} \\ -1 & \text{if } N^{\alpha} = 1 + N^{\beta} \end{cases}$
Two level system	$\frac{P_{10}}{P_{00}} = \frac{P_{01}}{P_{00}} = \frac{\gamma_1 f_1 + \gamma_2 f_2}{\gamma_1 \bar{f}_1 + \gamma_2 \bar{f}_2}, \quad \frac{P_{11}}{P_{10}} = \frac{P_{11}}{P_{01}} = \frac{\gamma_1 f'_1 + \gamma_2 f'_2}{\gamma_1 \bar{f}'_1 + \gamma_2 \bar{f}'_2}$ $I_1 = -\frac{e}{\hbar} (2\gamma_1 f_1 P_{00} + \gamma_1 (f'_1 - \bar{f}_1) (P_{01} + P_{10}) - 2\gamma_1 \bar{f}'_1 P_{11})$ $f_1 = f_0(\varepsilon - U_0/2 - eV_g - E_{F1}), f_2 = f_0(\varepsilon - U_0/2 - eV_g - E_{F2})$ $f'_1 = f_0(\varepsilon + U_0/2 - eV_g - E_{F1}), f'_2 = f_0(\varepsilon + U_0/2 - eV_g - E_{F2})$

Figure 2.1.8: Two level system.

tions for the distribution of the electrons in thermal equilibrium at all times; (2) the transport through the molecule is dominated by tunneling through a single, spin-degenerate electronic level, and (3) one vibron taken into account within the harmonic approximation. In this case, the Anderson-Holstein Hamiltonian reads $H = H_{mol} + H_{leads} + H_T$ with

$$H_{mol} = \varepsilon_d n_d + U n_{d\uparrow} n_{d\downarrow} + \hbar\omega b^{\dagger} b + \lambda \hbar\omega (b^{\dagger} + b) n_d \quad (2.1.28)$$

describing the electronic and vibrational degrees of freedom of the molecule,

$$H_{leads} = \sum_{a=L,R} \sum_{p,\sigma} (\varepsilon_{ap} - \mu_a) c_{ap\sigma}^{\dagger} c_{ap\sigma} \quad (2.1.29)$$

the noninteracting leads, and

$$H_T = \sum_{a=L,R} \sum_{p,\sigma} (t_{ap} c_{ap\sigma}^{\dagger} d_{\sigma} + h.c.) \quad (2.1.30)$$

the tunneling between the leads and molecule. Here, Coulomb blockade is taken into account via the charging energy U where $eV, k_B T \ll U$. The operator d_{σ} (d_{σ}^{\dagger}) annihilates (creates)

an electron with spin projection σ on the molecule, $n_d = \sum_{\sigma} d_{\sigma} d_{\sigma}^{\dagger}$ denotes the corresponding occupation-number operator. Similarly, $c_{ap\sigma}$ ($c_{ap\sigma}^{\dagger}$) annihilates (creates) an electron in lead a ($a = L, R$) with momentum p and spin projection σ . Vibrational excitations are annihilated (created) by b (b^{\dagger}). They couple to the electric charge on the molecule by the term $\sim n_d(b^{\dagger} + b)$, which can be eliminated by a canonical transformation, leading to a renormalization of the parameters ε and U , and of the lead-molecule coupling $t_a \rightarrow t_a e^{-\lambda(b^{\dagger} + b)}$. The master equations determining the molecular occupation probabilities P_q^n for charge state n and vibrons q is:

$$\frac{dP_q^n}{dt} = \sum_{n', q'} (P_{q'}^{n'} W_{q' \rightarrow q}^{n' \rightarrow n} - P_q^n W_{q \rightarrow q'}^{n \rightarrow n'}) - \frac{1}{\tau} (P_q^n - P_q^{eq} \sum_{q'} P_{q'}^n) \quad (2.1.31)$$

P_q^{eq} denotes the equilibrium vibron distribution with a relaxation time τ and $W_{q \rightarrow q'}^{n \rightarrow n'}$ denotes the total rate for a transition from $|n, q\rangle$ to $|n', q'\rangle$.

$$\begin{aligned} W_{q \rightarrow q'}^{n \rightarrow n+1} &= \sum_{a=L,R} (f_a(E_{q'}^{n+1} - E_q^n)) \Gamma_{q \rightarrow q'; a}^{n \rightarrow n+1}, \\ W_{q \rightarrow q'}^{n \rightarrow n-1} &= \sum_{a=L,R} (1 - f_a(E_q^n - E_{q'}^{n-1})) \Gamma_{q \rightarrow q'; a}^{n \rightarrow n-1} \end{aligned} \quad (2.1.32)$$

where f_a is the Fermi function and the transition rates Γ are calculated from Fermi's golden rule.

$$\begin{aligned} \Gamma_{q \rightarrow q'; a}^{n \rightarrow n+1} &= s^{n \rightarrow n+1} \frac{2\pi}{\hbar} \rho_a(E_{q'}^{n+1} - E_q^n) |M_{q \rightarrow q'; a}^{n \rightarrow n+1}| \\ \Gamma_{q \rightarrow q'; a}^{n \rightarrow n-1} &= s^{n \rightarrow n-1} \frac{2\pi}{\hbar} \rho_a(E_q^n - E_{q'}^{n-1}) |M_{q \rightarrow q'; a}^{n \rightarrow n-1}| \end{aligned} \quad (2.1.33)$$

Here, ρ_a denotes the density of states in lead a , $M_{q \rightarrow q'; a}^{n \rightarrow n \pm 1}$ denotes the FC matrix elements and $s^{n \rightarrow m}$ the spin factor [14] such that for sequential tunnelling and assuming twofold degeneracy they are $s^{1 \rightarrow 0} = s^{1 \rightarrow 2} = 1, s^{0 \rightarrow 1} = s^{2 \rightarrow 1} = 2$. The matrix elements $M_{q \rightarrow q'; a}^{n \rightarrow n \pm 1}$ defined for vibrations are

$$M_{q \rightarrow q'; a}^{n \rightarrow n \pm 1} = t_0 \sqrt{\frac{q_1!}{q_2!}} \lambda^{q_2 - q_1} e^{-\lambda^2/2} \quad (2.1.34)$$

where $q_1 = \min\{q, q'\}$ and $q_2 = \max\{q, q'\}$.

2.2 Modelling the experiment

So far I have briefly discussed, different transport regimes and the methods to model electron and phonon through nanoscale junctions. However, all these tools are only useful if they can

explain new physical phenomenon or predict a new characteristic for a future physical system. Experiments in the field of molecular electronics either study new junction physical properties such as conductance and current or they focus on using well characterized junctions for future applications. The crucial point is, there are certain phenomenon that only theory could access and analyse such as wave-functions, which is not a physical observable and others that only experiment could shed light, such as the position of the Fermi energy, the overall effect of the inhomogeneous broadening on the transport, or screening effects which is related to the exact junction configuration in the real-time experiment. Therefore, theoretically, predictions made based for the trends by comparing two or more system with the similar condition are potentially more reliable than those which are only based on the numbers predicted from the theory.

The bottom line is the theory and experiment are not two isolated endeavours. They need to talk to each-other to lead a new discoveries. Those quantities that cannot be computed reliably, but for which experimental data is available, can be used to correct and refine theoretical models. Usually to explain new phenomena, one needs to make a working hypothesis and then try to build a model to quantify the phenomenon. To make an initial hypothesis, a theorist needs to know how different physical phenomenon such as the effect of the environment, presence of an electric or magnetic field could be modelled. In the following, my aim is to make a few bridges between the well-known physical phenomena and the methods to model them theoretically, some of which I have used to obtain results presented in this thesis and some others that applied in my other investigations reflected in my papers.

2.2.1 Virtual leads versus physical leads

Let's start by considering the differences between a lead and a channel theoretically? From a mathematical viewpoint, channels connect an extended scattering region to a reservoir and the role of lead i is simply to label those channels k_i, \bar{q}_i , which connect to a particular reservoir i . Conceptually, this means that from the point of view of solving a scattering problem at energy E , a single lead with $N(E)$ incoming channels can be regarded as $N(E)$ virtual leads, each with a single channel. We could take advantage of this equivalence by regarding the above groups of channels with wave-vectors $k_{\alpha_i}, \bar{q}_{\alpha_i}$ as virtual leads and treating them on the same footing as physical leads.

This viewpoint is particularly useful when the Hamiltonians H_0^i, H_1^i describing the principle layers PLs (the identical periodic unit cells H_0^i connected to each other by H_1^i) of the physical

lead i are block diagonal with respect to the quantum numbers associated with $k_{\alpha_i}, \bar{q}_{\alpha_i}$. For example, this occurs when the leads possess a uniform magnetization, in which case the lead Hamiltonian is block diagonal with respect to the local magnetization axis of the lead and α represents the spin degree of freedom σ . This occurs also when the leads are normal metals, but the scattering region contains one or more superconductors, in which case the lead Hamiltonian is block diagonal with respect to particle and hole degrees of freedom and α represents either particles p or holes h . More generally, in the presence of both magnetism and superconductivity, α would represent combinations of spin and particles and holes degrees of freedom.

In all of these cases, H_0^i, H_1^i are block diagonal and it is convenient to identify virtual leads α_i with each block, because I can compute the channels $k_{\alpha_i}, \bar{q}_{\alpha_i}$ belonging to each block in separate calculations and therefore guarantees that all such channels can be separately identified. This is advantageous, because if all channels of H_0^i, H_1^i were calculated simultaneously, then in the case of degeneracies, arbitrary superpositions of channels with different quantum numbers could result and therefore it would be necessary to implement a separate unitary transformation to sort channels into the chosen quantum numbers. By treating each block as a virtual lead, this problem is avoided.

2.2.2 Charge, spin and and thermal currents

When comparing theory with experiment, we are usually interested in computing the flux of some quantity Q from a particular reservoir. If the amount of Q carried by quasi-particles of type α_i is $Q_{\alpha_i}(E)$, then the flux of Q from reservoir i is:

$$I_Q^i = \int (dE/h) \sum_{\alpha_i, j, \beta_j} P_{\alpha_i, \beta_j}^{i, j} \bar{f}_{\beta_j}^j(E) \quad (2.2.1)$$

$P_{\alpha_i, \beta_j}^{i, j}$ in this expression is transmission coefficient of quasi-particles of type α_i . In the simplest case of a normal conductor, choosing $Q_{\alpha_i} = -e$, independent of α_i , this equation yields the electrical current from lead i . α_i may represent spin, and in the presence of superconductivity it may represent hole ($\alpha_i = h$) or particle ($\alpha_i = p$) degrees of freedom. In the latter case, the charge Q_p carried by particles is $-e$, whereas the charge Q_h carried by holes is $+e$. In the presence of non-collinear magnetic moments, provided the lead Hamiltonians are block diagonal in spin

indices, choosing $\alpha_i = \sigma_i$ and $Q_{\alpha_i} = -e$ in Eq. (2.2.1) yields for the total electrical current

$$I_e^i = -e \int (dE/h) \sum_{\sigma_i, j, \sigma_j} P_{\sigma_i, \sigma_j}^{i, j} \bar{f}_{\beta_j}^j(E) \quad (2.2.2)$$

Note that in general it is necessary to retain the subscripts i, j associated with σ_i or σ_j , because the leads may possess different magnetic axes.

Similarly the thermal energy carried by the electrons from reservoir i per unit time is

$$I_q^i = \int (dE/h) \sum_{\sigma_i, j, \sigma_j} (E - \mu_i) P_{\sigma_i, \sigma_j}^{i, j} \bar{f}_{\beta_j}^j(E) \quad (2.2.3)$$

For the special case of a normal multi-terminal junction having collinear magnetic moments, $\alpha_i = \sigma$ for all i and since there is no spin-flip scattering, $P_{\sigma, \sigma'}^{i, j} = P_{\sigma, \sigma}^{i, j} \delta_{\sigma, \sigma'}$. In this case, the total Hamiltonian of the whole system is block diagonal in spin indices and the scattering matrix can be obtained from separate calculations for each spin. I assume that initially the junction is in thermodynamic equilibrium, so that all reservoirs possess the same chemical potential μ_0 . Subsequently, I apply to each reservoir i a different voltage V_i , so that its chemical potential is $\mu_i = \mu_0 - eV_i$. Then from equation (2.2.1), the charge per unit time per spin entering the scatterer from each lead can be written as

$$I_e^i = -e \int (dE/h) \sum_{\sigma, j} P_{\sigma, \sigma}^{i, j} \bar{f}_{\sigma}^j(E) \quad (2.2.4)$$

and the thermal energy per spin per unit time is

$$I_q^i = \int (dE/h) \sum_{\sigma, j} (E - \mu_i) P_{\sigma, \sigma}^{i, j} \bar{f}_{\sigma}^j(E) \quad (2.2.5)$$

where $e = |e|$ and $\bar{f}_{\sigma}^i(E) = f(E - \mu_i) - f(E - \mu)$ is the deviation in Fermi distribution of lead i from the reference distribution $f(E - \mu)$.

In the linear-response regime, the electric current I and heat current \dot{Q} passing through a device is related to the voltage difference ΔV and temperature difference ΔT by

$$\begin{pmatrix} \Delta V \\ \dot{Q} \end{pmatrix} = \begin{pmatrix} G^{-1} & -S \\ \Pi & \kappa_{el} \end{pmatrix} \begin{pmatrix} I \\ \Delta T \end{pmatrix} \quad (2.2.6)$$

where electrical conductance G (thermal conductance κ_{el}) is the ability of the device to conduct

electricity (heat) and the thermopower S^e (Peltier Π) is a measure of generated voltage (temperature) due to a temperature (voltage) differences between two sides of the device. In the limit of small potential differences or small differences in reservoir temperatures, the deviations in the distributions from the reference distribution $\bar{f}_\sigma^j(E)$ can be approximated by differentials and therefore to evaluate currents, in the presence of collinear magnetism, the following spin-dependent integrals provided

$$L_{ij,\sigma}^n(T, E_F) = \int_{-\infty}^{\infty} dE (E - E_F)^n T_{\sigma,\sigma}^{ij}(E, E_F) \left(-\frac{\partial f}{\partial E} \right) \quad (2.2.7)$$

where $f(E, T) = (1 + e^{(E-E_F)/k_B T})^{-1}$ is Fermi-Dirac distribution function and k_B is Boltzmanns constant. In the presence of two leads labeled $i = 1, 2$, the spin-dependent low-voltage electrical conductance $G(T, E_F)$, the thermopower (Seebeck coefficient) $S(T, E_F)$, the Peltier coefficient $\Pi(T, E_F)$ and the thermal conductance due to the electrons $\kappa_{el}(T, E_F)$ as a function of Fermi energy E_F and temperature T can be obtained as

$$\begin{aligned} G(T, E_F) &= \sum_{\sigma} \frac{e^2}{h} L_{12,\sigma}^0 \\ S(T, E_F) &= -\frac{1}{eT} \frac{\sum_{\sigma} L_{12,\sigma}^1}{\sum_{\sigma} L_{12,\sigma}^0} \\ \Pi(T, E_F) &= T S(T, E_F) \\ \kappa_{el}(T, E_F) &= \frac{1}{hT} \left(\sum_{\sigma} L_{12,\sigma}^2 - \frac{(\sum_{\sigma} L_{12,\sigma}^1)^2}{\sum_{\sigma} L_{12,\sigma}^0} \right) \end{aligned} \quad (2.2.8)$$

Note that the thermal conductance is guaranteed to be positive, because the expectation value of the square of a variable is greater than or equal to the square of the expectation value.

Efficiency of a thermoelectric material η is defined as the ratio between the work done per unit time against the chemical potential difference (between two hot and cold reservoir) and the heat extracted from the hot reservoir per unit time. The maximum efficiency η_{max} could be written as:

$$\eta_{max} = \frac{\Delta T}{T_h} \frac{\sqrt{Z \cdot T_{avg} + 1} - 1}{\sqrt{Z \cdot T_{avg} + 1} + \frac{T_c}{T_h}} \quad (2.2.9)$$

where T_h and T_c are the hot- and cold-side temperatures, respectively, $\Delta T = T_h - T_c$ and $T_{avg} = (T_h + T_c)/2$. The thermoelectric conversion efficiency (equation 2.2.9) is the product of the Carnot efficiency ($\frac{\Delta T}{T_h}$) and a reduction factor as a function of the materials figure of merit $Z = S^2 G \kappa^{-1}$, where S , G , and $\kappa = \kappa_{el} + \kappa_{ph}$ are the Seebeck coefficient, electrical conductance,

and thermal conductance due to both electrons and phonons, respectively. More commonly a dimensionless figure of merit ($ZT = Z.T_{avg}$) is used to account for the efficiency of the thermoelectric materials. The thermoelectric figure of merit could be written as

$$ZT = ZT_{el} \frac{\kappa_{el}}{\kappa_{el} + \kappa_{ph}} \quad (2.2.10)$$

where the electronic thermoelectric figure of merit for a two-terminal system is

$$ZT_{el} = \frac{L_{12}^1}{L_{12}^0 L_{12}^2 - L_{12}^1} \quad (2.2.11)$$

To calculate the total ZT , not only the thermal conductance due to the electrons are needed but also it is absolutely crucial to take the phonons contribution to the thermal conductance (κ_{ph}) into account as described in the next section.

2.2.3 Phonon thermal conductance

To calculate the heat flux through a molecular junction carried by the phonons, the equation 2.2.1 could be used where the thermal conductance due to the phonons κ_{ph} could be obtained [15] by calculating the phononic transmission T_{ph} for different vibrational modes as

$$\kappa_{ph}(T) = \frac{1}{2\pi} \int_0^\infty \hbar\omega T_{ph}(\omega) \frac{\partial f_{BE}(\omega, T)}{\partial T} d\omega \quad (2.2.12)$$

where $f_{BE}(\omega, T) = (e^{\hbar\omega/k_B T} - 1)^{-1}$ is Bose-Einstein distribution function and \hbar is reduced Plancks constant and k_B is Boltzmanns constant. To calculate the vibrational modes of a system, I use the harmonic approximation method to construct the dynamical matrix D . From the ground state relaxed xyz coordinate of the system, each atom is displaced from its equilibrium position by δq and δq in x , y and z directions and the forces $F_i^q = (F_i^x, F_i^y, F_i^z)$ in three directions $q_i = (x_i, y_i, z_i)$ on each atoms calculated. For $3n$ degrees of freedom (n = number of atoms), the $3n \times 3n$ dynamical matrix D is constructed

$$D_{ij} = \frac{K_{ij}^{qq'}}{M_{ij}} \quad (2.2.13)$$

where $K_{ij}^{qq'}$ for $i \neq j$ are obtained from finite differences

$$K_{ij}^{qq'} = \frac{F_i^q(\delta q'_j) - F_i^{q'}(\delta q'_j)}{2\delta q'_j} \quad (2.2.14)$$

and the mass matrix $M = \sqrt{M_i M_j}$. To satisfy momentum conservation, the K s for $i = j$ (diagonal terms) are calculated from $k_{ii} = -\sum_{i \neq j} K_{ij}$. Once the dynamical matrix is constructed the Green's function method as described in 2.1.4 could be used to calculate the phononic transmission coefficient T_{ph} .

2.2.4 Spectral adjustment

Although DFT is good at predicting the trends, it usually underestimates the position of the Fermi energy E_F , the exact energy levels (Kohn-Sham eigenvalues [16]) and therefore the position of the HOMO and LUMO and the energy gap. Therefore, to compare mean-field theory with experiment, some corrections are needed. One way is to use hybrid functionals e.g. B3LYP [17] or many body calculations e.g. GW approximation [18]. These methods are either computationally very expensive (GW) where you cannot do calculation for a system with about 100 atoms in the best supercomputers today or they are fitted parameters to the experiment where their accuracy is not definite in new structures. For example, B3LYP combines the Hartree potential which usually overestimates the energy gap within the Kohn-Sham scheme which usually underestimate it to give more realistic gap. An alternative way is to correct the HOMO-LUMO gap using the values measured experimentally. A phenomenological scheme that improves the agreement between theoretical simulations and experiments in, for example, single-molecule electronics consists of shifting the occupied and unoccupied levels of the M (e.g. Molecule) region downwards and upwards respectively to increase the energy gap of the M region. The procedure is conveniently called spectral adjustment in nanoscale transport (SAINT) [9]. The Hamiltonian $K = H - ES$ of a given M region could be modified as:

$$K_M = K_M^0 + (\Delta_o - \Delta_u) S_M \rho_M S_M + \Delta_u S_M \quad (2.2.15)$$

where $\Delta_{o,u}$ are energy shifts and (no, nu) denote the occupied and unoccupied states, respectively. $\rho_M = \sum_{no} |\Psi_{no}\rangle \langle \Psi_{no}|$ is the density matrix and S_M is overlap matrix. If experimental HOMO and LUMO energies are available, $\Delta_{o,u}$ can be chosen to correct HOMO and LUMO obtained from mean-field Hamiltonian. Alternatively, in the simplest case, the shifts $\Delta_{o,u}$ are chosen to

align the highest occupied and lowest unoccupied molecular orbitals (ie the HOMO and LUMO) with (minus) the ionization potential (IP) and electron affinity (EA) of the isolated molecule

$$\begin{aligned}\Delta_o^0 &= \epsilon_{\text{HOMO}} + IP \\ \Delta_u^0 &= -(\epsilon_{\text{LUMO}} + EA)\end{aligned}\tag{2.2.16}$$

However the Coulomb interactions in the isolated molecule are screened if the molecule is placed in close proximity to the metallic electrodes. This could be taken into account by using a simple image charge model, where the molecule is replaced by a point charge located at the middle point of the molecule and where the image planes are placed 1 \AA above the electrodes' surfaces. Then the shifts are corrected by screening effects $\Delta_{o,u} = \Delta_{o,u}^0 + e^2 \ln 2 / (8\pi\epsilon_0 a)$ where a is the distance between the image plane and the point image charge.

2.2.5 Inclusion of a Gauge field

For a scattering region of area A , if a magnetic field B is applied the magnetic flux $\phi = B \times A$. To compute transport properties in the presence of a magnetic field, a Peierls substitution could be introduced by changing the phase factors of the coupling elements between atomic orbitals. For example in the case of a nearest-neighbor tight-binding Hamiltonian, the hopping matrix element H_{ij} between site i and site j is replaced with the modified element,

$$H_{ij}^B = H_{ij} e^{-i\phi},\tag{2.2.17}$$

where

$$\phi = \frac{e}{\hbar} \int_{\mathbf{r}_j}^{\mathbf{r}_i} \mathbf{A}(\mathbf{r}) d\mathbf{r}\tag{2.2.18}$$

and \mathbf{r}_i and \mathbf{r}_j are the positions of site i and j and \mathbf{A} is the vector potential. The gauge should be chosen such that the principal layers of the leads remain translationally invariant after the substitution.

2.2.6 Superconducting systems

Figure 2.2.1a shows a two-probe normal-superconductor-normal (N-S-N) device with left and right normal reservoirs connected to a scattering region containing one or more superconduc-

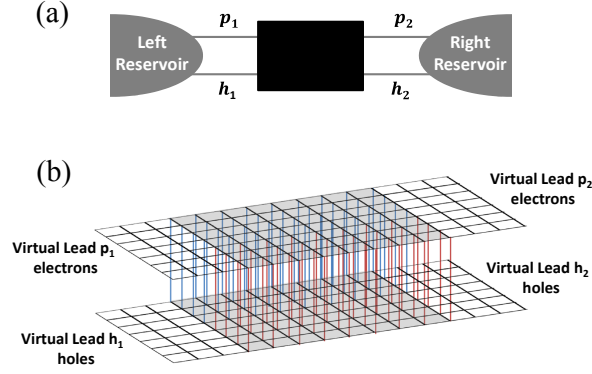


Figure 2.2.1: Two-probe device consist of reservoirs α and β connected to a superconductor

tors. If the complete Hamiltonian describing a normal system is H_N , then in the presence of superconductivity within the extended scattering region, the new system is described by the Bogoliubov-de Gennes Hamiltonian

$$H = \begin{pmatrix} H_N & \Delta \\ \Delta^* & -H_N^* \end{pmatrix} \quad (2.2.19)$$

where the elements of the matrix Δ are non-zero only in the region occupied by a superconductor, as indicated in figure 2.2.1b. Physically, H_N describes particle degrees of freedom, $-H_N^*$ describes hole degrees of freedom and Δ is the superconducting order parameter.

The multi-channel scattering theory for such a normal-superconducting-normal (N-S-N) structure could be written as [19]:

$$\begin{pmatrix} I_{left} \\ I_{right} \end{pmatrix} = \frac{2e^2}{h} a \begin{pmatrix} \frac{\mu_{left} - \mu}{e} \\ \frac{\mu_{right} - \mu}{e} \end{pmatrix} \quad (2.2.20)$$

where I_{left} (I_{right}) is the current from the left (right) reservoir, $\mu_{left} - \mu$ ($\mu_{right} - \mu$) is the difference between the chemical potential of the left (right) reservoir and the chemical potential μ of the superconducting condensate and the voltage difference between the left and right reservoirs is $(\mu_{left} - \mu_{right})/e$. In this equation,

$$a = \begin{pmatrix} N_{left} - R_o + R_a & -T_o' + T_a' \\ -T_o + T_a & N_{right} - R_o' + R_a' \end{pmatrix} \quad (2.2.21)$$

where N_{left} (N_{right}) is the number of open channels in the left (right) lead, R_o, T_o (R_a, T_a) are

normal (Andreev) reflection and transmission coefficients for quasi-particles emitted from the right lead, R'_o, T'_o (R'_a, T'_a) are normal (Andreev) reflection and transmission coefficients from the left lead and all quantities are evaluated at the Fermi energy $E = \mu$. As a consequence of unitarity of the scattering matrix, these satisfy $R_o + T_o + R_a + T_a = N_{left}$ and $R'_o + T'_o + R'_a + T'_a = N_{right}$.

The current-voltage relation of Equ. (2.2.20) is fundamentally different from that encountered for normal systems, because unitarity of the s-matrix does not imply that the sum of each row or column of the matrix a is zero. Consequently, the currents do not automatically depend solely of the applied voltage difference $(\mu_{left} - \mu_{right})/e$ (or more generally on the differences between incoming quasi-article distributions). In practice such a dependence arises only after the chemical potential of the superconductor adjusts itself self-consistently to ensure that the current from the left reservoir is equal to the current entering the right reservoir. Insisting that $I_{left} = -I_{right} = I$, the two-probe conductance $G = I/((\mu_{left} - \mu_{right})/e)$ takes the form of

$$G = \frac{2e^2}{h} \frac{a_{11}a_{22} - a_{12}a_{21}}{a_{11} + a_{22} + a_{12} + a_{21}} \quad (2.2.22)$$

The above equation demonstrates why a superconductor possesses zero resistivity, because if the superconductor is disordered, then as the length L of the superconductor increases, all transmission coefficients will vanish. In this limit, the above equation reduces to $(h/2e^2)G = 2/R_a + 2/R'_a$. In contrast with a normal scatterer, this shows that in the presence of Andreev scattering, as L tends to infinity, the resistance ($= 1/\text{conductance}$) remains finite and therefore the resistivity (ie resistance per unit length) vanishes.

2.2.7 Environmental effects

To model environmental effects e.g. water, counter-ions, etc on the transport properties of a molecular junction, usually a statistical analysis needs to be carried out. Since a molecular junction in the presence of the surrounding molecules is a dynamic object at room temperature, a molecular dynamics simulation is usually needed first, to understand the range of possible configurations of the system. A few configuration then should be extracted and full DFT calculations carried out to obtain the mean field Hamiltonian of the system in the presence of the surrounding molecules. Another way to study the environmental effect is to create a series of configurations in the presence of the surrounding molecules in a more systematic but less physical way e.g. by moving the surroundings artificially in different directions. Then without geometry relaxation,

one could find the binding energy of the surroundings to the backbone of the molecule for each configuration and only study those with higher binding energies. Both of these methods are widely used in the literature to model environmental effects. In this thesis whenever needed, I have used the first method in which molecular dynamics is used to study the dynamics of the system before full DFT-NFGF calculation. It is worth mentioning that since different effects such as physisorption, charge transfer, etc could play important role in these simulations, SCF methods need to be used to calculate the transport from mean-field Hamiltonian.

2.3 GOLLUM transport code

In this thesis, in most cases otherwise explicitly stated, I have used GOLLUM transport code [9], developed and maintained in Lancaster and Oviedo universities (physics.lancs.ac.uk/gollum) for transport calculations. Gollum is a program that computes the charge, spin and thermal transport properties of multi-terminal nano-scale junctions. The program can compute transport properties of either user-defined systems described by a tight-binding Hamiltonian, or more material-specific properties of systems composed of real atoms described by DFT mean field Hamiltonians. As Gollum administrator and one of the Gollum authors, I have been a part of Gollum development process throughout my PhD and the most of the functionalities described in this thesis either already included in official version of the Gollum available for academics free of charge or will be included in the near future.

References

- [1] S. Datta, *Quantum Transport : Atom to Transistor*. Cambridge Univ Pr, 2005.
- [2] E. Schrödinger, “An Undulatory Theory of the Mechanics of Atoms and Molecules,” *Phys. Rev.*, vol. 28, pp. 1049–1070, dec 1926.
- [3] E. Engel and R. M. Dreizler, *Density Functional Theory*, vol. 2011. Springer Verlag, 2011.
- [4] N. Harrison, “An introduction to density functional theory,” *NATO Science Series Sub Series III: Computer and systems sciences*, vol. 187, pp. 45–70, 2003.
- [5] J. M. J. M. Soler, E. Artacho, J. D. Gale, A. García, J. Junquera, P. Ordejón, D. Sánchez-Portal, A. Garcia, J. Junquera, P. Ordejon, and D. Sanchez-Portal, “The SIESTA method for

- ab initio order-N materials simulation,” *Journal of physics. Condensed matter* :, vol. 2745, p. 22, mar 2002.
- [6] C. J. Lambert, “Basic concepts of quantum interference and electron transport in single-molecule electronics,” *Chem. Soc. Rev.*, vol. 44, pp. 875–888, 2015.
- [7] N. R. Claughton, M. Leadbeater, and C. J. Lambert, “Theory of Andreev Resonances in Quantum Dots,” *Journal of Physics-Condensed Matter*, vol. 7, no. 46, pp. 8757–8784, 1995.
- [8] S. Sanvito, C. J. Lambert, J. H. Jefferson, and a. M. Bratkovsky, “General Green’s-function formalism for transport calculations with spd Hamiltonians and giant magnetoresistance in Co- and Ni-based magnetic multilayers,” *Phys. Rev. B*, vol. 59, no. 18, pp. 936–948, 1999.
- [9] J. Ferrer, C. J. Lambert, V. M. García-Suárez, D. Z. Manrique, D. Visontai, L. Oroszlany, R. Rodríguez-Ferradás, I. Grace, S. Bailey, K. Gillemot, *et al.*, “Gollum: a next-generation simulation tool for electron, thermal and spin transport,” *New Journal of Physics*, vol. 16, no. 9, p. 093029, 2014.
- [10] R. Landauer, “Electrical transport in open and closed systems,” *Z. Phys. B: Condens. Matter*, vol. 68, no. 2-3, pp. 217–228, 1987.
- [11] M. Buttiker, “Symmetry of electrical conduction,” *IBM Journal of Research and Development*, vol. 32, no. 3, pp. 317–334, 1988.
- [12] M. Buttiker, “Coherent and sequential tunneling in series barriers,” *IBM Journal of Research and Development*, vol. 32, no. 1, pp. 63–75, 1988.
- [13] J. Koch, F. von Oppen, F. V. Oppen, and F. von Oppen, “Franck-Condon Blockade and Giant Fano Factors in Transport through Single Molecules,” *Physical Review Letters*, vol. 94, no. 20, p. 206804, 2005.
- [14] C. S. Lau, H. Sadeghi, G. Rogers, S. Sangtarash, P. Dallas, K. Porfyrakis, J. Warner, C. J. Lambert, G. A. D. Briggs, and J. A. Mol, “Redox-dependent franck–condon blockade and avalanche transport in a graphene–fullerene single-molecule transistor,” *Nano letters*, vol. 16, no. 1, pp. 170–176, 2015.

- [15] H. Sadeghi, S. Sangtarash, and C. J. Lambert, “Oligoyne molecular junctions for efficient room temperature thermoelectric power generation,” *Nano letters*, vol. 15, no. 11, pp. 7467–7472, 2015.
- [16] J. M. Seminario, “An introduction to density functional theory in chemistry,” *Theoretical and Computational Chemistry*, vol. 2, no. C, pp. 1–27, 1995.
- [17] A. D. Becke, “A new mixing of hartree–fock and local density-functional theories,” *The Journal of Chemical Physics*, vol. 98, no. 2, pp. 1372–1377, 1993.
- [18] L. Hedin, “New method for calculating the one-particle green’s function with application to the electron-gas problem,” *Phys. Rev.*, vol. 139, pp. A796–A823, Aug 1965.
- [19] C. J. Lambert and R. Raimondi, “Phase-coherent transport in hybrid superconducting nanostructures,” *Journal of Physics: Condensed Matter*, vol. 10, no. 5, pp. 901–941, 1998.

Chapter 3

DNA nucleobase sensing

To demonstrate the potential of nanopores in bilayer graphene for DNA sequencing, I compute the current-voltage characteristics of a bilayer graphene junction containing a nanopore and show that this changes significantly when nucleobases are transported through the pore. To demonstrate the sensitivity and selectivity of exemplar devices, I compute the probability distribution $P_x(\beta)$ of the quantity β representing the change in the logarithmic current through the pore due to the presence of a nucleobase x (= adenine, thymine, guanine or cytosine). I quantify the selectivity of the bilayer-graphene nanopores by showing that $P_x(\beta)$ possesses distinct peaks for each base x . To demonstrate that such discriminating sensing is a general feature of bilayer nanopores, the well-separated positions of these peaks are shown to be present for different pores, with alternative examples of electrical contacts.

The results presented in this chapter were published in: Sadeghi, et al. Graphene sculpture nanopores for DNA nucleobase sensing, 2014, The Journal of Physical Chemistry B 118 (24), 6908-6914 and protected by patent number WO2015092411 A1 (18 Dec 2013) entitled: Nanopore arrangement for DNA sequencing.

A single strand of deoxyribonucleic acid (DNA) is constructed from a deoxyribose sugar and phosphate backbone with sequences of four nucleic acid bases, adenine (A), thymine (T), guanine (G) and cytosine (C) (see figure 3.1) attached along its length. Apart from well-established biological functionalities [1], DNA also exhibits interesting electrical characteristics, including a range of superconducting, conducting, semiconducting and insulating properties [2].

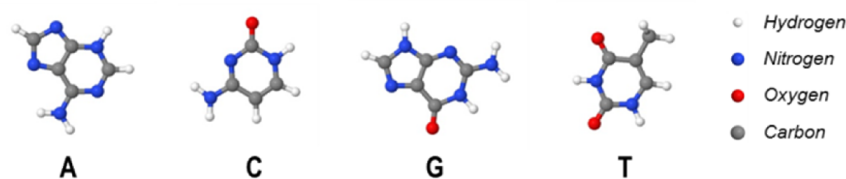
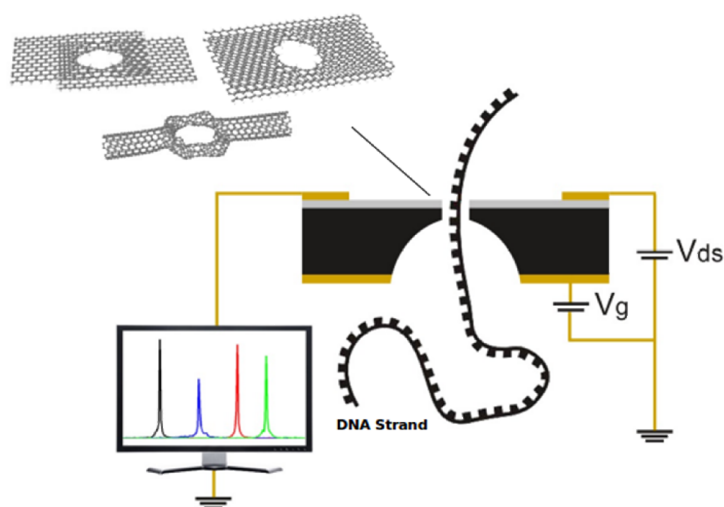


Figure 3.1. Schematics of the four DNA bases: adenine (A), thymine (T), guanine (G) and cytosine (C) [1].

Sequencing of nucleobases within single-stranded DNA is the focus of a great deal of research aimed at developing efficient and cost effective personalised medicine [3]. Established technologies, such as chain-termination and single-molecule sequencing methods [4-6] are time consuming and costly [7] and the search for alternative fourth-generation sequencing methods is attracting huge scientific interest [8, 9].

All molecular-based biosensors rely on a molecular recognition layer and a signal transducer that reports specific recognition events. Electrochemical or electrical methods are well suited for DNA sequencing, because there is no need for separate transduction to an electrical signal and therefore detection can be accomplished with an inexpensive electrochemical analyser [10]. Furthermore, recent developments in device miniaturization provide electrical transduction capabilities at the nano- and molecular scales, leading to low-cost and low-power requirements compared to conventional methods. One implementation of this approach is based on measurement of the variation in the ionic current through a solid state [11-15] or biological [16, 17] nanopore, due to the translocation of a DNA strand through the pore. However, the current leakage through such pores, low signal-to-noise ratios and poor control of the speed of the strand through the pore create significant obstacles [18, 19]. To overcome the

key technical problems associated with real-time, high-resolution nucleoside monophosphate detection, biological nanopores MspA and α -hemolysin have been employed as recognition sites inside the pore [16]. However the sensitivity of biological nanopores to experimental conditions, the integration of biological systems into large-scale arrays, the small (\sim pA) ionic currents and the mechanical instability of the lipid bilayer that supports the nanopore still need to be improved [19-22].



Schematic 3.1. Device structure proposed for DNA sequencing in this chapter. Different membrane nanopores could be used as the recognition site. A single strand DNA is translocated through the nanopore. A two terminal (I - V_{ds}) or three terminal (G - V_g) configurations with back gate voltage V_g could be utilized.

In this chapter, I examine an alternative strategy, which involves measuring changes in the electrical conductance of the membrane containing the pore (Schematic 3.1), rather than variations in an ionic current passing through the pore. In particular, I demonstrate the potential of this approach for sequencing nucleobases passing through nanopores in bilayer graphene. For sensing applications, graphene has a number of potential advantages, such a wide electrochemical potential window, low electrical resistance, and well-defined redox peaks, which can lead to increased sensitivity [23]. It also offers superior performance for future bio sensing applications [24] and high sensitivity towards the detection of a range of molecules and ions [25-34]. In addition, current technologies such as transmission electron microscopy (TEM)

allow the drilling of nanopores with different diameters, down to sub-angstrom precision [35-38]. Some of the first graphene nanopores for DNA sequencing were realized experimentally by Schneider *et al.* [39] and Merchant *et al.* [40], where they measured the change in ionic currents through graphene nanopores on top of silicon nitride, due to single-molecule DNA translocation. However, the response of device to changes of the ionic current upon translocation of DNA bases are slow (on the scale of ms) [41] compared with much faster response available to direct electrical measurement (on the scale of μs to ns) [42].

The first *ab initio* density functional theory (DFT) study of the interaction of nucleobases with a monolayer graphene nanopore device was reported by Nelson *et al* where the variation of the electrical current upon translocation of DNA bases inside the pore was proposed as a detection method [43]. Saha, et al also calculated the conductance of a monolayer graphene nanopore containing nucleobases and showed that the conductance depended on the orientation of the nucleobases within the pore [3]. However, they did not propose a clear method of distinguishing between different bases. Furthermore, nanopores in monolayer graphene are unstable and change their shape over time [44]. For DNA sequencing, it may be necessary to calibrate individual pores and such instabilities would lead to a progressive loss of calibration. On the other hand, our calculations in [45, 46] show that bilayer pores are stable and experiments such as [47] show that the edge reconstruction which stabilises such pores is persistent. For this reason, I examine in this chapter the potential of nanopores in bilayer graphene, which are more stable than their monolayer counterparts.

An exemplar platform consists of a bilayer graphene nanoribbon containing a reconstructed, stable nanopore, as shown in figure 3.2. This structure is an example of a class of sp^2 -bonded carbon structures known as sculpturenes [45]. The latter are formed by sculpting selected shapes from AB-stacked bilayer graphene and allowing the shapes to spontaneously reconstruct to form stable structures of sp^2 -bonded carbon, which remain stable over time.

For the structure of figure 3.2, after performing a structure relaxation using the density-functional theory code *SIESTA*, the top and bottom graphene layers adjust their positions to achieve a more locally-energetically-stable AA-stacking in the vicinity of the pore. This type of

relaxation has been recently reported elsewhere[48]. The width of the graphene nano-ribbon and the diameter of the pore in figure 3.2 are $\sim 3\text{nm}$ and $\sim 1.5\text{nm}$ respectively with an inter-sheet separation of 0.34 nm . Since the distance between two bases in a DNA strand is also $\sim 0.34\text{ nm}$ [49], the proposed bilayer graphene nanopore (BLGNP) is optimised for base detection, because on the one hand, a membrane of thickness more than 0.34 nm , would contain more than one base at a time inside the pore, thereby reducing its ability to discriminate [50], while on the other hand, a monolayer pore is less stable structurally.

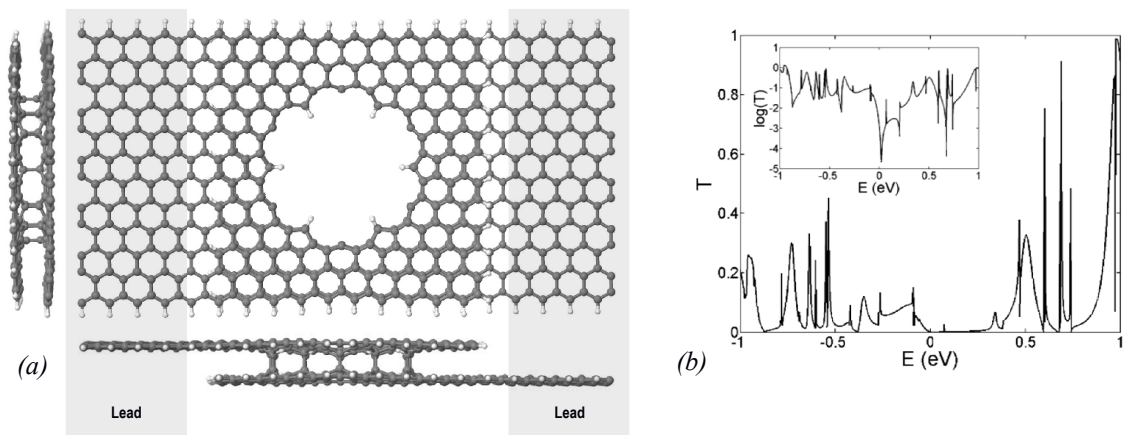


Figure 3.2. Relaxed atomic structure of a sculpted bilayer graphene nanopore with monolayer graphene leads (a) and the transmission coefficients $T(E)$ (b). The inset in (b) shows the logarithm of the transmission $T(E)$. The Fermi energy is set to $E_F = 0.0\text{ eV}$.

Furthermore the method should be easier to implement than an alternative nanopore technique, which relies on locating electrodes on an insulating pore-containing substrate and passing a tunnelling current through individual nucleobases [51]. To further optimise the device, I also propose that the pore is contacted to the outer current source via monolayer graphene leads, as shown in figure 3.2. As shown in the side view at the bottom of figure 3.2a, in order for the electrical current to flow from left to right through the monolayer graphene current-carrying leads, it must pass through the orbitals of the carbon atoms on the inner surface of the pore, which increases the sensitivity of the device to the presence of nucleobases. After relaxation, the surface carbon atoms are mainly sp^2 bonded, although there are also a small number of unsaturated bonds. In the structure of figure 3.2, these are passivated by adding hydrogen to

form C-H bonds [52]. In what follows, I compute the current I as a function of the voltage V between the left and right leads (i.e. between the source and drain) and show that through appropriate data analysis, this device can be used to discriminate between nucleobases passing through the pore.

To find the optimized geometry and ground state Hamiltonian of the structure of figure 3.2, I followed the procedure described in [45] and employed the *SIESTA* [53] implementation of *DFT* using the generalized gradient approximation (*GGA*) of the exchange and correlation functional with the Perdew-Burke-Ernzerhof parameterization (*PBE*) [54] a double zeta polarized basis set, a real-space grid defined with a plane wave cut-off energy of 250 Ry and a maximum force tolerance of 40 meV/\AA . To describe the many possible orientations and positions of nucleobases within the pore, molecular dynamics simulations of the nucleobases were carried out using the *LAMMPS* package [55]. The atoms were treated in the *DREIDING* force field model, a Langevin thermostat at 300K was employed and the atomic positions updated in 0.02fs time steps. During the simulation, a number of snapshots were taken and for each frozen snapshot, the electronic structure of the combined nucleobase and nanopore was obtained self-consistently using the *SIESTA*-based implementation of *DFT* described above. From the converged *DFT* calculation, the underlying mean-field Hamiltonian was combined with the *SMEAGOL* [56] implementation of the *NEGF* method. This yields the transmission coefficient $T(E)$ for electrons of energy E (passing from the source to the drain) via the relation

$$T(E) = \text{Trace} \{ \Gamma_R(E) G^R(E) \Gamma_L(E) G^{R\dagger}(E) \} \quad (3.1)$$

In this expression, $\Gamma_{L,R}(E) = i \left(\Sigma_{L,R}(E) - \Sigma_{L,R}^\dagger(E) \right)$ describe the level broadening due to the coupling between left (L) and right (R) electrodes and the central scattering region associated with the pore, $\Sigma_{L,R}(E)$ are the retarded self-energies associated with this coupling and $G^R = (ES - H - \Sigma_L - \Sigma_R)^{-1}$ is the retarded Green's function, where H is the Hamiltonian and S is overlap matrix (both of them obtained from *SIESTA*).

To highlight the underlying changes in transport properties due to a nucleobase $X=[A, C, G, T]$, located within the pore, with orientation m , I compute the transmission coefficient $T_{X,m}(E)$ and define the quantity

$$\alpha_{X,m}(E) = \log_{10}(T_{X,m}(E)) - \log_{10}(T_{\text{bare}}(E)) \quad (3.2)$$

where $T_{\text{bare}}(E)$ is the transmission coefficient for electrons of energy E passing from left to right in the presence of a ‘bare’ (ie unoccupied) pore. $\alpha_{X,m}(E)$ is a measure of the differences between $T_{X,m}(E)$ and the transmission $T_{\text{bare}}(E)$ in the absence of a base. To differentiate between different bases, I analyse the set of all values of $\alpha_{X,m}(E)$ for $E_{\min} < E < E_{\max}$ and configuration $m = 1, \dots, M$ belonging to a given base X . The probability distribution of the set $\{\alpha_{X,m}(E)\}$ for a given base X is then defined by

$$P_X(\alpha) = \frac{1}{M(E_{\max} - E_{\min})} \sum_{m=1}^M \int_{E_{\min}}^{E_{\max}} dE \delta(\alpha - \alpha_{X,m}(E)) \quad (3.3)$$

where $\delta(\alpha - \alpha_{X,m}(E))$ is a Dirac delta function. This has the property that the fraction of values of $\alpha_{X,m}(E)$ between $\alpha = a$ and $\alpha = b$ is $\int_a^b d\alpha P_X(\alpha)$.

From an experimental point of view, $\alpha_{X,m}(E)$ is not directly accessible in a two-terminal device such as that shown in figure 3.2, therefore for the purpose of analyzing experimentally-accessible two-terminal data, I also examine the quantity $\beta_{X,m}(V)$ defined by

$$\beta_{X,m}(V) = \log_{10}(I_{X,m}(V)) - \log_{10}(I_{\text{bare}}(V)) \quad (3.4)$$

where

$$I_{X,m}(V) = \frac{2e}{h} \int_{E_F - \frac{eV}{2}}^{E_F + \frac{eV}{2}} dE T_{X,m}(E) \quad (3.5)$$

is the finite-bias current evaluated for bias voltage V for each orientation $m = 1, \dots, M$ of a given base X within the pore. The probability distribution of the set $\{\beta_{X,m}(E)\}$ for a given base X is then defined by

$$P_X(\beta) = \frac{1}{M(eV_{\max} - eV_{\min})} \sum_{m=1}^M \int_{V_{\min}}^{V_{\max}} dV \delta(\beta - \beta_{X,m}(V)) \quad (3.6)$$

Figure 3.2b shows the transmission coefficient $T_{bare}(E)$ versus energy (where the energy origin is chosen such that Fermi energy $E_F = 0.0 eV$) in the absence of any nucleobase. It should be noted that for the purpose of this proof of principle, the effect of water has not been included in the calculations, because the H- π interactions between water molecules and graphene are weak and in a recent paper, [57] the effect of water was found to be insignificant. To study the sensing properties of the nanopore platform and the effect of the orientation of the bases inside the pore on the transmission, I chose 54 different configurations for each of the four nucleobases and calculated the transmission for all $4 \times 54 = 216$ possibilities. These configurations were obtained using molecular dynamics simulations, in which each base was allowed to move inside the pore. 54 different snapshots were taken and a full *NEGF* calculation was performed for each configuration. As examples, the left hand side in figures 3.3(a-d) show one configuration for each of the *A*, *C*, *G* and *T* bases, located inside the nanopore. The resulting logarithmic transmission coefficients ($\log_{10} T_{X,m}(E)$) and their deviations from those of the bare pore ($\alpha_{X,m}(E)$) are shown in the centre and left hand side of figure 3.3, respectively.

Figure 3.4 shows all 216 plots of $\log_{10} T_{X,m}(E)$ superposed on the same graph, for each of the *A*, *C*, *G* and *T* bases and 54 different configurations for each base. This shows that the low-voltage conductance alone (which is proportional to the transmission coefficient $T_{X,m}(E)$ evaluated at the Fermi energy $E=0$) does not provide enough information to discriminate between different nucleotides and therefore a more comprehensive analysis based on measurement of α_X or β_X is required.

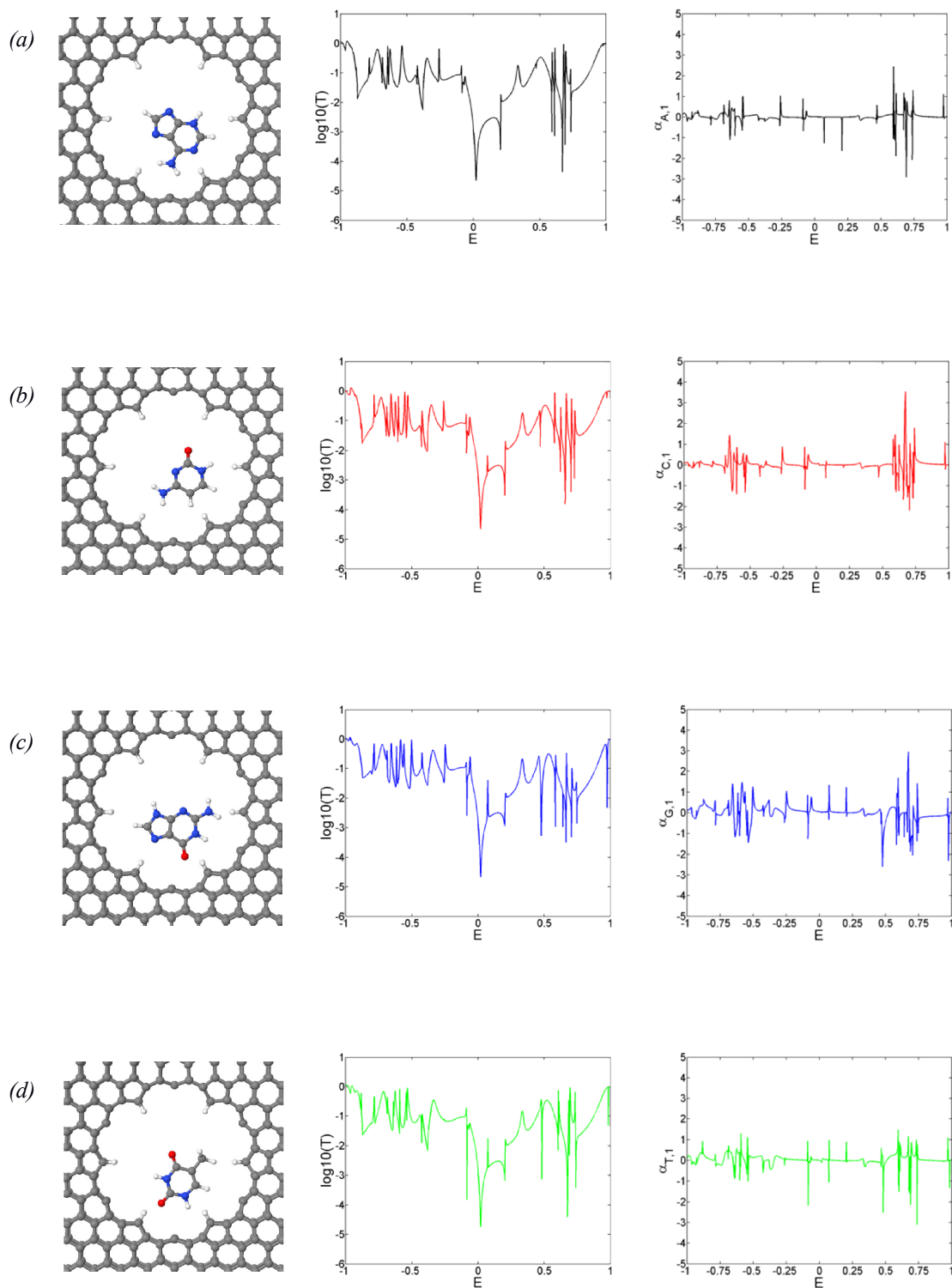


Figure 3.3. The left panels show one example each of the nucleobase bases *A*, *C*, *G* and *T* (parts (a), (b), (c) and (d) respectively) located inside the nanopore. The central panels show the resulting logarithmic transmission $\log_{10}T_{X,m}(E)$ and the right panels show their deviations $\alpha_{X,m}(E)$ from that of the bare (unoccupied) pore.

Figure 3.4 also shows that the energy dependence of $T_{X,m}(E)$ reflects a complex interference pattern, which arises from quantum interference in the vicinity of the pore surface. In this sense, the pore acts like a chaotic quantum dot, whose properties were well studied by the mesoscopic physics community in the late 1980s [58]. From the plots in figure 3.4, the probability distributions $P_X(\alpha)$ are obtained by sampling the curves at a uniformly-spaced set of energies and creating histograms of the associated values of $\alpha_{X,m}(E)$. The resulting probability distributions are shown in figure 3.5.

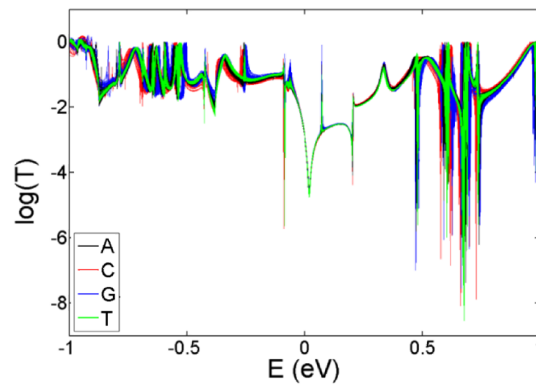


Figure 3.4. Logarithm of the transmission versus energy for each base with 54 different configurations (a total of 216 curves).

The presence of distinct peaks in figure 3.5 demonstrates the potential of this bilayer nanopore for the discriminating sensing of nucleobases. Figure 3.6(a) shows corresponding plots for the experimentally-accessible quantities $\beta_{X,m}(E)$, whose probability distributions are shown in figure 3.6(b). Again the presence of distinct peaks demonstrates the excellent sensing potential of the proposed bilayer nanopore for sequencing DNA.

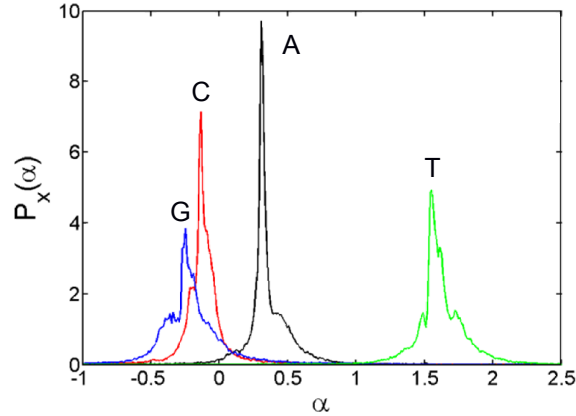


Figure 3.5. The probability distribution ($P_x(\alpha)$) of the set $\{\alpha_{x,m}(E)\}$ are shown for a given base X where $X = A$ in black, C in red, G in blue and T in green.

To demonstrate that discriminating sensing is a general feature of other sculpturene-based nanopores, with alternative electrical contacts, I now investigate the effect of varying the structure of both the pore and the electrical contacts. As discussed in [45], a range of stable nanopore-containing sculpturenes can be created by sculpting shapes from bilayer graphene and allowing the shapes to relax. Figure 3.7a (upper structure) shows one such structure, obtained by cutting bilayer graphene into a torus-containing nanoribbon and allowing it to reconstruct to form a two terminal hollow torus connected to carbon nanotube (CNT) leads. In figure 3.7a, the pore is approximately 1.6 nm in diameter and it is linked to (6,6) armchair CNTs with a thickness of approximately 0.5 nm. For the bare, unoccupied pore, figure 3.7b shows the transmission coefficients for electrons of energy E .

By introducing structurally optimised nucleobases into the cavity of the torus and calculating the $I(V)$ characteristic for 4 different orientations of each base, I obtain the probability distributions $P_x(\beta)$ shown in figure 3.7c. Despite the more limited data set, this figure again demonstrates the potential of this nanopore for discriminating nucleobase sensing and suggests that nanopores formed from bilayer graphene provided a basic technology platform for discriminating sensing. Since the ordering of the peaks in the figure 3.7c differs from that of figure 3.6b, this suggests that the size and shape of the pores is poorly controlled, then each pore would need to be calibrated prior to use. Furthermore the ordering of the peaks will also depend

on sample preparation. To demonstrate this feature, the inset of figure 3.7c shows the probability distributions arising when the phosphate deoxyribose backbone remains attached to the bases as they pass through the pore, as shown in figure 3.7d. Again the peaks in $P_x(\beta)$ remain well separated, but their ordering is changed.

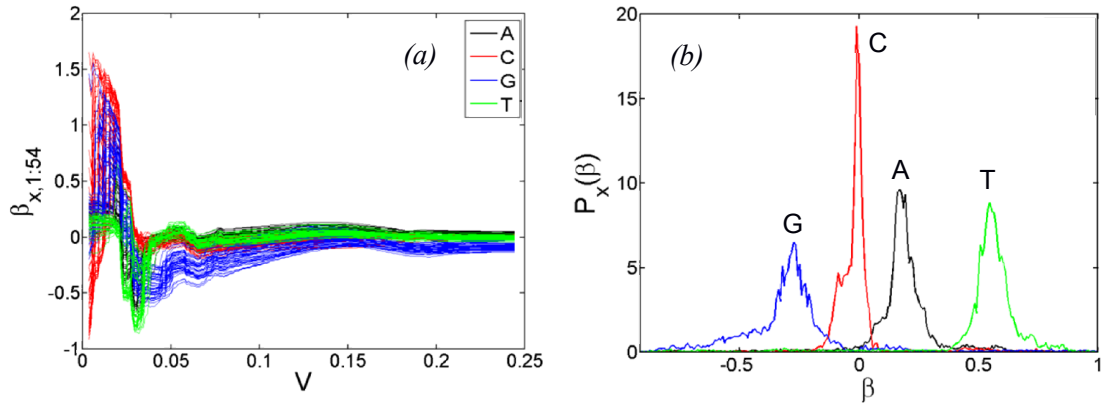


Figure 3.6. (a) The differences between the logarithm of the current in the presence of each base for 54 different configurations ($\beta_{X,m}$). (b) The probability distribution ($P_x(\beta)$) of the set $\{\beta_{X,m}\}$ are shown for a given base X where X = A in black, C in red, G in blue and T in green.

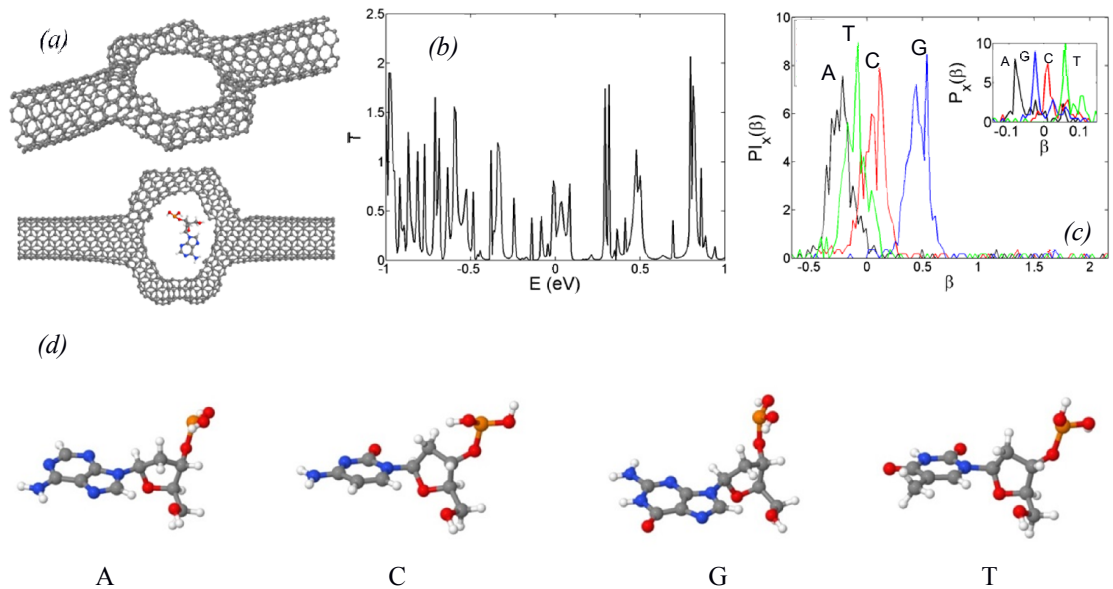


Figure 3.7. (a) Atomic structure of a two terminal hollow torus connected to carbon nanotube (CNT) leads. (b) The transmission coefficient $T_{bare}(E)$ calculated for single electron transport from the left to the right leads. (c) Probability distribution ($P_x(\beta)$) of the set $\{\beta_{X,m}\}$ for a given base X with backbone (inset: without backbone). (d) Schematics of the four DNA bases attached to phosphate deoxyribose: adenine (A), thymine (T), guanine (G) and cytosine (C).

In this chapter, I have demonstrated the discriminating sensing properties of new bilayer-graphene, sculptureene-based nano-pore devices by calculating the electrical current-voltage characteristics of two-terminal device in the absence and presence of given nucleobase for many different positions and orientations of bases within the pore. The resulting fingerprint probability distribution $P_x(\beta)$ shows distinct peaks for different nucleobase. The proposed method is based on direct electrical current measurement and potentially has clear advantages comparing with conventional DNA sequencing methods based on ionic current measurement. One of these is higher signal to noise, because the current through the graphene is of order microamps, whereas the current measured in ion-current-based methods are of order picoamps and there is no reason to suppose the noise would be greater. Another is the potential for a faster response, because conventional nanoelectronics can complete a current-voltage cycle on the scale of micro- or even nanoseconds, whereas ionic current-based methods require milliseconds or longer. By comparing bilayer and toroidal pore within different geometries and electrical contacts and by sensing bases in the absence and presence of the phosphate deoxyribose backbone, I have demonstrated that discriminating sensing is resilient. However the ordering of the peaks in $P_x(\beta)$ depends on the shape of the pore and on the presence of phosphate deoxyribose and therefore it is likely that nanopores will need to be calibrated individually before use. This calibration is feasible, because bilayer nanopores are much more stable than their monolayer counterparts and graphene-based nanostructures can be interfaced with CMOS electronics, thereby allowing them to be individually addressed and replicated many times in a single chip. Therefore, the proposed method could open new routes for label free, fast and cheap DNA sequencing.

References

- [1] M. Taniguchi and T. Kawai, "DNA electronics," *Physica E: Low-Dimensional Systems and Nanostructures*, vol. 33, pp. 1-12, 2006.
- [2] K. Siriwong and A. A. Voityuk, "Electron transfer in DNA," *Wiley Interdisciplinary Reviews: Computational Molecular Science*, vol. 2, pp. 780–794, 2012.

- [3] K. K. Saha, M. Drndic, and B. K. Nikolic, "DNA Base-Specific Modulation of Microampere Transverse Edge Currents through a Metallic Graphene Nanoribbon with a Nanopore," *Nano Letters*, vol. 12, pp. 50-55, 2012.
- [4] E. Pettersson, J. Lundeberg, and A. Ahmadian, "Generations of sequencing technologies," *Genomics*, vol. 93, pp. 105-111, 2009.
- [5] D. Branton, D. W. Deamer, A. Marziali, H. Bayley, S. A. Benner, T. Butler, *et al.*, "The potential and challenges of nanopore sequencing," *Nat Biotech*, vol. 26, pp. 1146-1153, 2008.
- [6] M. Xu, D. Fujita, and N. Hanagata, "Perspectives and Challenges of Emerging Single-Molecule DNA Sequencing Technologies," *Small*, vol. 5, pp. 2638-2649, 2009.
- [7] P. Hu, J. Zhang, L. Li, Z. Wang, W. O'Neill, and P. Estrela, "Carbon Nanostructure-Based Field-Effect Transistors for Label-Free Chemical/Biological Sensors," *Sensors*, vol. 10, pp. 5133-5159, 2010.
- [8] S. McGinn and I. Glynne Gu, "DNA sequencing – spanning the generations," *New biotechnology*, vol. 30, pp. 366-372, 2013.
- [9] H. Sadeghi, S. Bailey, and C. J. Lambert, "Silicene-based DNA nucleobase sensing," *Applied Physics Letters*, vol. 104, p. 103104, 2014.
- [10] T. G. Drummond, M. G. Hill, and J. K. Barton, "Electrochemical DNA sensors," *Nature biotechnology*, vol. 21, pp. 1192-1199, 2003.
- [11] C. Dekker, "Solid-state nanopores," *Nature Nanotechnology*, vol. 2, pp. 209-215, 2007.
- [12] J. Shim, G. I. Humphreys, B. M. Venkatesan, J. M. Munz, X. Zou, C. Sathe, *et al.*, "Detection and Quantification of Methylation in DNA using Solid-State Nanopores," *Sci. Rep.*, vol. 3, 2013.

- [13] D. B. Wells, M. Belkin, J. Comer, and A. Aksimentiev, "Assessing Graphene Nanopores for Sequencing DNA," *Nano Letters*, vol. 12, pp. 4117-4123, 2012.
- [14] S. Garaj, S. Liu, J. A. Golovchenko, and D. Branton, "Molecule-hugging graphene nanopores," *Proceedings of the National Academy of Sciences*, vol. 110, pp. 12192-12196, 2013.
- [15] B. M. Venkatesan, D. Estrada, S. Banerjee, X. Jin, V. E. Dorgan, M.-H. Bae, *et al.*, "Stacked Graphene-Al₂O₃ Nanopore Sensors for Sensitive Detection of DNA and DNA-Protein Complexes," *Acs Nano*, vol. 6, pp. 441-450, 2012.
- [16] E. A. Manrao, I. M. Derrington, A. H. Laszlo, K. W. Langford, M. K. Hopper, N. Gillgren, *et al.*, "Reading DNA at single-nucleotide resolution with a mutant MspA nanopore and phi29 DNA polymerase," *Nature biotechnology*, vol. 30, pp. 349-353, 2012.
- [17] J. Clarke, H.-C. Wu, L. Jayasinghe, A. Patel, S. Reid, and H. Bayley, "Continuous base identification for single-molecule nanopore DNA sequencing," *Nature Nanotechnology*, vol. 4, pp. 265-270, 2009.
- [18] B. Luan, G. Stolovitzky, and G. Martyna, "Slowing and controlling the translocation of DNA in a solid-state nanopore," *Nanoscale*, vol. 4, pp. 1068-1077, 2012.
- [19] B. M. Venkatesan and R. Bashir, "Nanopore sensors for nucleic acid analysis," *Nature Nanotechnology*, vol. 6, pp. 615-624, 2011.
- [20] P. Xie, Q. Xiong, Y. Fang, Q. Qing, and C. M. Lieber, "Local electrical potential detection of DNA by nanowire-nanopore sensors," *Nature Nanotechnology*, vol. 7, pp. 119-125, 2012.
- [21] D. Anselmetti, "Nanopores: Tiny holes with great promise," *Nature Nanotechnology*, vol. 7, pp. 81-82, 2012.

- [22] G. M. Cherf, K. R. Lieberman, H. Rashid, C. E. Lam, K. Karplus, and M. Akeson, "Automated forward and reverse ratcheting of DNA in a nanopore at 5-A precision," *Nature biotechnology*, vol. 30, pp. 344-348, 2012.
- [23] M. S. Artiles, C. S. Rout, and T. S. Fisher, "Graphene-based hybrid materials and devices for biosensing," *Advanced Drug Delivery Reviews*, vol. 63, pp. 1352-1360, 2011.
- [24] F. Liu, Y. Piao, K. S. Choi, and T. S. Seo, "Fabrication of free-standing graphene composite films as electrochemical biosensors," *Carbon*, vol. 50, pp. 123-133, 2012.
- [25] Z. Zhu, L. Garcia-Gancedo, A. J. Flewitt, H. Xie, F. Moussy, and W. I. Milne, "A Critical Review of Glucose Biosensors Based on Carbon Nanomaterials: Carbon Nanotubes and Graphene," *Sensors*, vol. 12, pp. 5996-6022, 2012.
- [26] N. Lei, P. Li, W. Xue, and J. Xu, "Simple graphene chemiresistors as pH sensors: fabrication and characterization," *Measurement Science & Technology*, vol. 22, 2011.
- [27] C. R. Ispas, G. Crivat, and S. Andreescu, "Review: Recent Developments in Enzyme-Based Biosensors For Biomedical Analysis," *Analytical Letters*, vol. 45, pp. 168-186, 2012.
- [28] J. Zhu, X. Chen, and W. Yang, "A high performance electrochemical sensor for NADH based on graphite nanosheet modified electrode," *Sensors and Actuators B-Chemical*, vol. 150, pp. 564-568, 2010.
- [29] Y. Shao, J. Wang, H. Wu, J. Liu, I. A. Aksay, and Y. Lin, "Graphene Based Electrochemical Sensors and Biosensors: A Review," *Electroanalysis*, vol. 22, pp. 1027-1036, 2010.
- [30] Q. He, S. Wu, Z. Yin, and H. Zhang, "Graphene-based electronic sensors," *Chemical Science*, vol. 3, pp. 1764-1772, 2012.

- [31] S.-J. Li, Y. Xing, and G.-F. Wang, "A graphene-based electrochemical sensor for sensitive and selective determination of hydroquinone," *Microchimica Acta*, vol. 176, pp. 163-168, 2012.
- [32] M. S. Goh and M. Pumera, "Graphene-based electrochemical sensor for detection of 2,4,6-trinitrotoluene (TNT) in seawater: the comparison of single-, few-, and multilayer graphene nanoribbons and graphite microparticles," *Analytical and Bioanalytical Chemistry*, vol. 399, pp. 127-131, 2011.
- [33] X. Kang, J. Wang, H. Wu, J. Liu, I. A. Aksay, and Y. Lin, "A graphene-based electrochemical sensor for sensitive detection of paracetamol," *Talanta*, vol. 81, pp. 754-759, 2010.
- [34] Y. Chen, H. Vedala, G. P. Kotchey, A. Audfray, S. Cecioni, A. Imberty, *et al.*, "Electronic Detection of Lectins Using Carbohydrate-Functionalized Nanostructures: Graphene versus Carbon Nanotubes," *Acs Nano*, vol. 6, pp. 760-770, 2012.
- [35] S. Liu, Q. Zhao, J. Xu, K. Yan, H. Peng, F. Yang, *et al.*, "Fast and controllable fabrication of suspended graphene nanopore devices," *Nanotechnology*, vol. 23, pp. 085301-085301, 2012.
- [36] P. S. Spinney, S. D. Collins, D. G. Howitt, and R. L. Smith, "Fabrication and characterization of a solid-state nanopore with self-aligned carbon nanoelectrodes for molecular detection," *Nanotechnology*, vol. 23, pp. 135501-135501, 2012.
- [37] M. Taniguchi, M. Tsutsui, K. Yokota, and T. Kawai, "Fabrication of the gating nanopore device," *Applied Physics Letters*, vol. 95, pp. 123701-123701-3, 2009.
- [38] C. J. Russo and J. A. Golovchenko, "Atom-by-atom nucleation and growth of graphene nanopores," *Proceedings of the National Academy of Sciences of the United States of America*, vol. 109, pp. 5953-5957, 2012.

- [39] G. F. Schneider, S. W. Kowalczyk, V. E. Calado, G. Pandraud, H. W. Zandbergen, L. M. K. Vandersypen, *et al.*, "DNA Translocation through Graphene Nanopores," *Nano Letters*, vol. 10, pp. 3163-3167, 2010.
- [40] C. A. Merchant, K. Healy, M. Wanunu, V. Ray, N. Peterman, J. Bartel, *et al.*, "DNA Translocation through Graphene Nanopores," *Nano Letters*, vol. 10, pp. 2915-2921, 2010.
- [41] M. Zwolak and M. Di Ventra, "Colloquium: Physical approaches to DNA sequencing and detection," *Reviews of Modern Physics*, vol. 80, pp. 141-165, 2008.
- [42] J. Lagerqvist, M. Zwolak, and M. Di Ventra, "Fast DNA Sequencing via Transverse Electronic Transport," *Nano Letters*, vol. 6, pp. 779-782, 2006.
- [43] T. Nelson, B. Zhang, and O. V. Prezhdo, "Detection of Nucleic Acids with Graphene Nanopores: Ab Initio Characterization of a Novel Sequencing Device," *Nano Letters*, vol. 10, pp. 3237-3242, 2010.
- [44] R. Zan, Q. M. Ramasse, U. Bangert, and K. S. Novoselov, "Graphene Reknits Its Holes," *Nano Letters*, vol. 12, pp. 3936-3940, 2012.
- [45] L. Algharagholy, S. W. D. Bailey, T. Pope, and C. J. Lambert, "Sculpting molecular structures from bilayer graphene and other materials," *Physical Review B*, vol. 86, p. 075427, 2012.
- [46] A. Laith, P. Thomas, W. D. B. Steven, and J. L. Colin, "Electronic properties of sculpturenes," *New Journal of Physics*, vol. 16, p. 013060, 2014.
- [47] Z. Liu, K. Suenaga, P. J. F. Harris, and S. Iijima, "Open and Closed Edges of Graphene Layers," *Physical Review Letters*, vol. 102, p. 015501, 2009.

- [48] L. Qi, Y. Mao, and J. Li, "Slip corona surrounding bilayer graphene nanopore," *Nanoscale*, vol. 4, pp. 5989-5997, 2012.
- [49] Bruce Alberts, Alexander Johnson, Julian Lewis, Martin Raff, Keith Roberts, and P. Walter, *Molecular Biology of the Cell: The Structure and Function of DNA*, 4th edition ed.: Garland Science, 2002.
- [50] C. R. O'Donnell, H. Wang, and W. B. Dunbar, "Error analysis of idealized nanopore sequencing," *Electrophoresis*, vol. 34, pp. 2137-2144, 2013.
- [51] J. R. Alvarez, D. Skachkov, S. E. Massey, J. Lu, A. Kalitsov, and J. P. Velev, "Intrinsic Noise from Neighboring Bases in the DNA Transverse Tunneling Current," *Physical Review Applied*, vol. 1, p. 034001, 2014.
- [52] Y. He, R. H. Scheicher, A. Grigoriev, R. Ahuja, S. Long, Z. Huo, *et al.*, "Enhanced DNA Sequencing Performance Through Edge-Hydrogenation of Graphene Electrodes," *Advanced Functional Materials*, vol. 21, pp. 2674-2679, 2011.
- [53] J. M. Soler, E. Artacho, J. D. Gale, A. García, J. Junquera, P. Ordejón, *et al.*, "The SIESTA method for ab initio order- N materials simulation," *Journal of Physics: Condensed Matter*, vol. 14, p. 2745, 2002.
- [54] J. P. Perdew, K. Burke, and M. Ernzerhof, "Generalized Gradient Approximation Made Simple," *Physical Review Letters*, vol. 77, pp. 3865-3868, 1996.
- [55] S. Plimpton, "Fast parallel algorithms for short-range molecular dynamics," *Journal of Computational Physics*, vol. 117, pp. 1-19, 1995.
- [56] A. R. Rocha, V. M. Garcia-suarez, S. W. Bailey, C. J. Lambert, J. Ferrer, and S. Sanvito, "Towards molecular spintronics," *Nat Mater*, vol. 4, pp. 335-339, 2005.

- [57] S. K. Min, W. Y. Kim, Y. Cho, and K. S. Kim, "Fast DNA sequencing with a graphene-based nanochannel device," *Nature Nanotechnology*, vol. 6, pp. 162-165, 2011.
- [58] H. U. Baranger and P. A. Mello, "Mesoscopic transport through chaotic cavities: A random S -matrix theory approach," *Physical Review Letters*, vol. 73, pp. 142-145, 1994.

Chapter 4

Picoscale graphene nanojunctions

Provided the electrical properties of electro-burnt graphene junctions can be understood and controlled, they have the potential to underpin the development of a wide range of future sub-10nm electrical devices. In this chapter, the electrical conductance of electro-burnt graphene junctions at the last stages of nanogap formation is examined both theoretically and experimentally. I account for the appearance of a counterintuitive increase in electrical conductance just before the gap forms. This is a manifestation of room-temperature quantum interference and arises from a combination of the semi-metallic band structure of graphene and a crossover from electrodes with multiple-path connectivity to single-path connectivity just prior to breaking. Therefore these results suggest that conductance enlargement prior to junction rupture is a signal of the formation of electro-burnt junctions, with a pico-scale current path formed from a single sp^2 -bond.

The results presented in this chapter were published in: Sadeghi, et al. Conductance enlargement in picoscale electroburnt graphene nanojunctions, 2015, Proceedings of the National Academy of Sciences (PNAS), 112 (9), 2658-2666

This study is a collaborative work and the experiment has been carried out in the University of Oxford.

Graphene nanojunctions are attractive as electrodes for electrical contact to single molecules [1-7], due to their excellent stability and conductivity up to high temperatures and a close match between their Fermi energy and the HOMO (highest occupied molecular orbital) or LUMO (lowest unoccupied molecular orbit) energy levels of organic materials. Graphene electrodes also facilitate electrostatic gating due to their reduced screening compared with more bulky metallic electrodes. Although different strategies for forming nano-gaps in graphene such as atomic force microscopy, nanolithography [8], electrical breakdown [9] and mechanical stress [10] have been employed, only electro-burning delivers the required gap-size control below 10 nm [11-13]. This new technology has the potential to overcome the challenges of making stable and reproducible single-molecule junctions with gating capabilities and compatibility with integrated circuit technology [14] and may provide the breakthrough that will enable molecular devices to compete with foreseeable developments in Moore's Law, at least for some niche applications [15-17].

One set of such applications is likely to be associated with room-temperature manifestations of quantum interference (QI), which are enabled by the small size of these junctions. If such interference effects could be harnessed in a single-molecule device, this would pave the way towards logic devices with energy consumption lower than the current state-of-the-art. Indirect evidence for such QI in single-molecule mechanically-controlled break junctions has been reported recently in a number of papers [18], but direct control of QI has not been possible, because electrostatic gating of such devices is difficult. Graphene electro-burnt junctions have the potential to deliver direct control of QI in single molecules, but before this can be fully achieved, it is necessary to identify and differentiate intrinsic manifestations of room temperature QI in the bare junctions, without molecules. In the present chapter, I account for one such manifestation, which is a ubiquitous feature in the fabrication of pico-scale gaps for molecular devices, namely an unexpected *increase* in the conductance prior to the formation of a tunnel gap.

Only a few groups in the world have been able to implement electro-burning method to form nanogap size junctions. In a recent study of electro-burnt graphene junctions, Barreiro, et

al. [19] used real-time in situ transmission electron microscopy (TEM) to investigate this conductance enlargement in the last moment of gap formation and ruled out the effects of both extra edge scattering and impurities, which reduce the current density near breaking. Also they showed that the graphene junctions can be free of contaminants prior to the formation of the nano-gap. Having eliminated these effects, they suggested that the enlargement may arise from the formation of the seamless graphene bilayers. Here I show that the conductance enlargement occurs in monolayer graphene, which rules out an explanation based on bilayers. Moreover, we have observed the enlargement in a large number of nominally identical graphene devices and therefore we can rule out the possibility of device- or flake-specific features in the electro-burning process. An alternative explanation was proposed by Lu, et al. [20], who observed the enlargement in few-layer graphene nanoconstrictions fabricated using TEM. They attributed the enlargement to an improvement in the quality of few-layer graphene due to current annealing, which simply ruled out by our experiments on electro-burnt single layers. They also attributed this to the reduction of the edge scattering due to the orientation of the edges (i.e. zigzag edges). However such edge effects have been ruled out by the TEM images of Barreiro, et al. Therefore, although this enlargement appears to be a common feature of graphene nano-junctions, so far the origin of the increase remains unexplained.

In what follows, my aim is to demonstrate that such conductance enlargement is a universal feature of electro-burnt graphene junctions and arises from quantum interference (QI) at the moment of breaking. Graphene provides an ideal platform for studying room-temperature QI effects [21], because as well as being a suitable material for contacting single molecules, it can serve as a natural two-dimensional grid of interfering pathways. By electro-burning a graphene junction to the point where only a few carbon bonds connect the left and right electrodes, one can study the effect of QI in ring- and chain-like structures that are covalently bonded to the electrodes. A feedback-controlled electro-burning on single-layer graphene nano-junctions performed by our collaborators confirms that there is an increase in conductance immediately before the formation of the tunnel-junction. My transport calculations for a variety of different atomic configurations using the non-equilibrium Green's function (NEGF) method

coupled to density functional theory (DFT) show a similar behaviour. To elucidate the origin of the effect, I provide a model for the observed increase in the conductance based on the transition from multi-path connectivity to single-path connectivity, in close analogy to an optical double slit experiment. The model suggests that the conductance increase is likely to occur whenever junctions are formed from any sp^2 -bonded material.

Experimentally the conductance jumps is studied by applying the method of feedback-controlled electro-burning to single-layer graphene (SLG) that was grown using chemical vapour deposition (CVD) and transferred onto a pre-patterned silicon chip as explained in the methods below and performed by our collaborators. The CVD graphene was patterned into 3 μm wide ribbons with a 200 nm wide constriction (see figure 4.1a) using electron-beam lithography and oxygen plasma etching. Feedback-controlled electro-burning has been demonstrated previously using few-layer graphene flakes that were deposited by mechanically exfoliation of kish graphite [11]. However, by applying the method to an array of nominally identical single-layer graphene devices, the possibility of device- or flake-specific features in the electro-burning process can be ruled out.

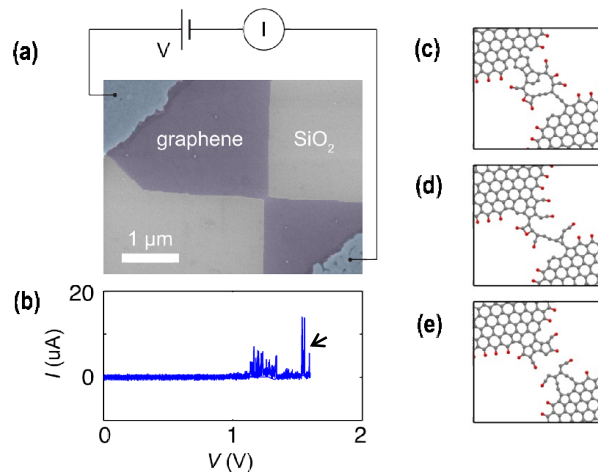


Figure 4.1. (a) Scanning electron micrograph of the graphene device, (b) Measured current-voltage characteristic of the final voltage ramp prior to the formation of the nano-gap. This exhibits a sharp increase of the conductance just before the nano-gap forms. (c-e) three atomic configuration with two (c), one (d) and zero (e) pathways.

The nano-gaps is formed by ramping up the voltage that is applied across the graphene device. As the conductance starts to decrease due to the breakdown of the graphene, the voltage is ramped back to zero. This process is repeated until the nano-gap is formed. The I - V traces of the voltage ramps, closely resemble those recorded for mechanically exfoliated graphite flakes. As the constriction narrows, the conductance of the SLG device decreases. When the conductance becomes less than the conductance quantum $G_0 = 2e^2/h$, the low-bias I - V traces are no longer Ohmic and start exhibiting random telegraph signal (RTS) as the SLG device switches between different atomic configurations. Figure 4.1b shows the I - V trace of the final voltage ramp, which exhibits a sharp increase of the conductance just before the nano-gap forms. This behaviour is characteristic of many of the devices. Out of the 279 devices that were studied, 138 devices showed a sharp increase in the conductance prior to the formation of the nano-gap.

To investigate theoretically the transport characteristics of graphene junctions upon breaking, I used classical molecular-dynamics simulations to simulate a series of junctions with oxygen and hydrogen terminations as well as carbon terminated edges and then used *DFT* combined with non-equilibrium Green's function (*NEGF*) methods to compute the electrical conductance of each structure as explained in the methods below. Figures 4.1c-e show three examples of the resulting junctions with oxygen terminated edges (which are the most likely to arise from the burning process), in which the left and right electrodes are connected via two (figure 4.1c), one (figure 4.1d) and zero (figure 4.1e) pathways.

Surprisingly, the conductance G through the single-path junction (figure 4.1d) is larger than the conductance through the double-path junction (figure 4.1c) (e.g. $G = 18\mu S$ for one path versus $G = 0.4\mu S$ for two paths in the low bias regime $V = 40mV$). For the nano-gap junction shown in figure 4.1e, the conductance is less than both of these ($G = 0.016 \mu S$). I have calculated the conductance for 42 atomic junction configurations (see figures 4.2 and 4.3), and commonly find that the conductance is larger for single-path junctions than for those with two or a few conductance paths.

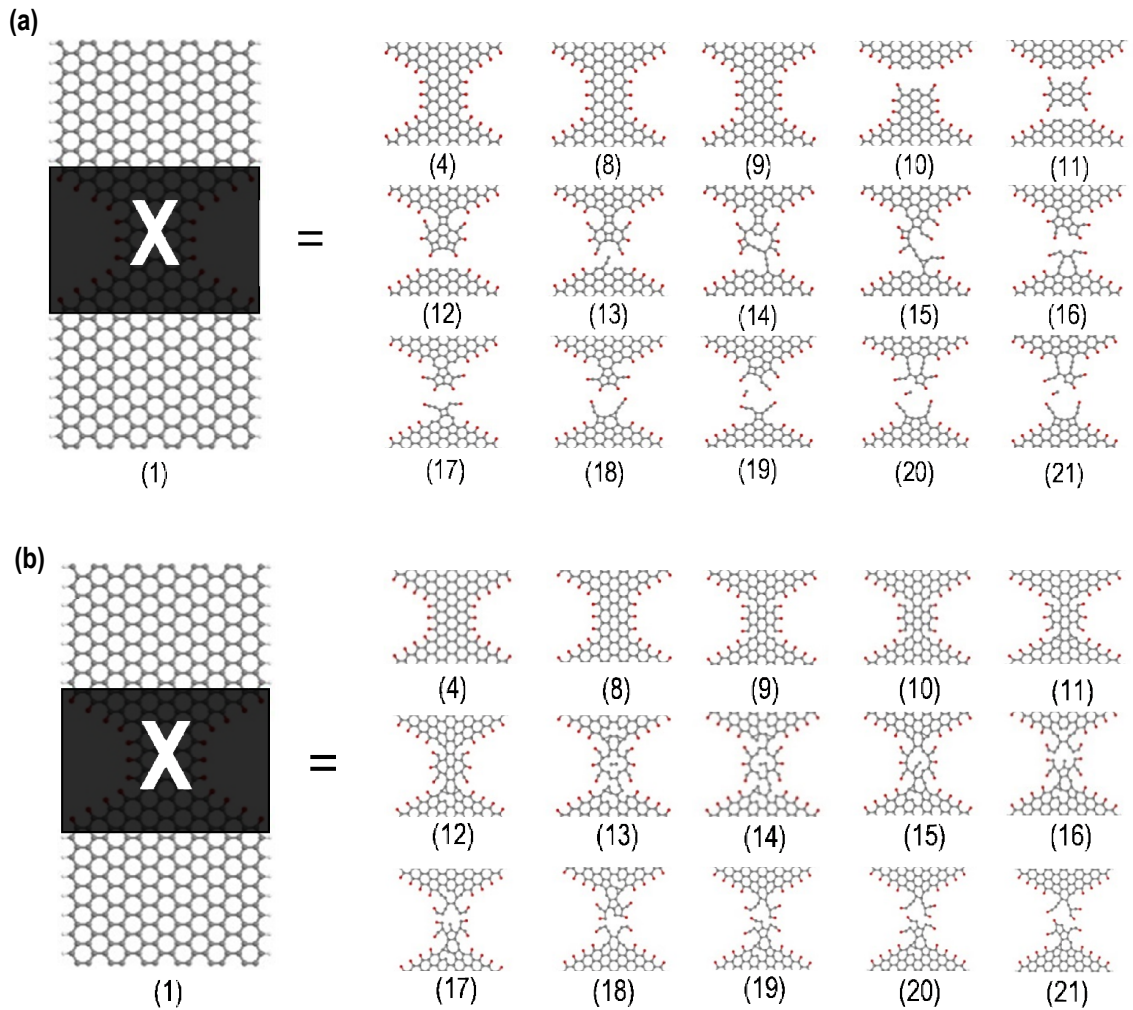


Figure 4.2. (a) The first set of break junction traces configurations [1, 4, 8, 9, 10, 11, 12, 13, 14, 15, 16, 17, 18, 19, 20, 21]. (b) Second set of the break junction traces [1, 4, 8, 9, 10, 11, 12, 13, 14, 15, 16, 17, 18, 19, 20, 21].

The changes in the calculated conductances of junctions approaching rupture show a close resemblance to the experiments presented in this chapter and by Barreiro, et al. [19] and arise from the changes in the atomic configuration of the junction. I therefore attribute the experimentally-observed jumps of the conductance to a transition from two- or few-path atomic configurations to single-path junctions, even though naïve application of Ohm's Law would predict a factor 2 *decrease* of the conductance upon changing from a double to a single pathway.

In the remainder of this chapter I will give a detailed analysis of the interference effects leading to the sudden conductance *increase* prior to the formation of a graphene nano-gap.

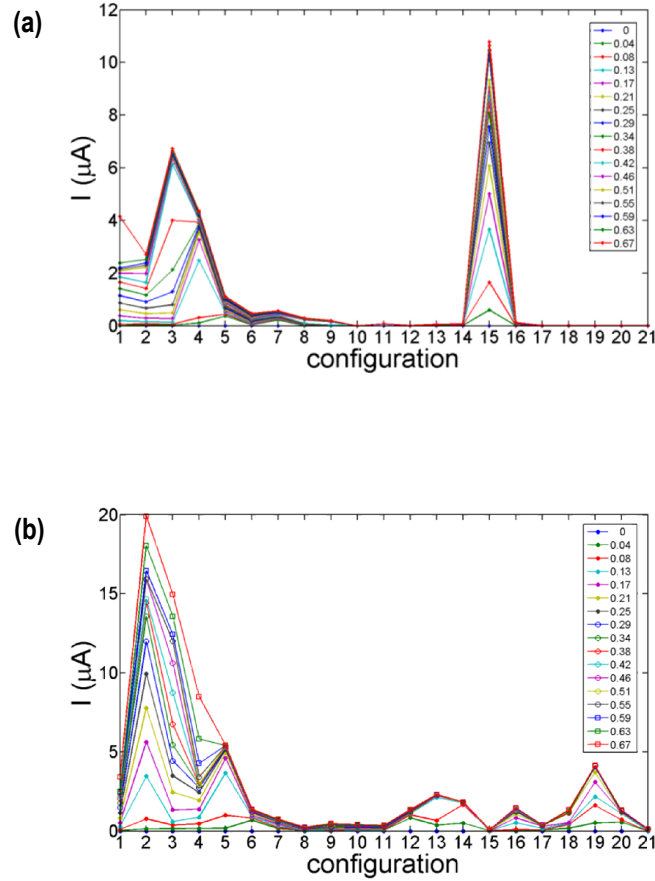


Figure 4.3. Calculated current in different applied bias voltages for (a) 21 different configurations shown in figure 4.2a and (b) another 21 different configurations shown in figure 4.2b.

Before proceeding to an analysis of QI effects, I first note that the conductance enlargement cannot be attributed to changes in the band structure near breaking. The band structures of the periodic chains and ribbons shown in figure 4.4 reveal that all are semi-metallic except alkane (figure 4.4c), due to the formation of a π band associated with the p orbital perpendicular to the plane of the structures. Moreover, the ribbon (figure 4.4e) has more open conductance channels than the chain (figure 4.4d) around the Fermi energy ($E=0$). The increase in conductance upon changing from a ribbon to a chain is therefore not due to a change in band structure, but rather due to QI in the different semi-metallic pathways. A similar behaviour is also found for

structures with hydrogen-termination and combined hydrogen-oxygen termination as shown in figure 4.4a-i.

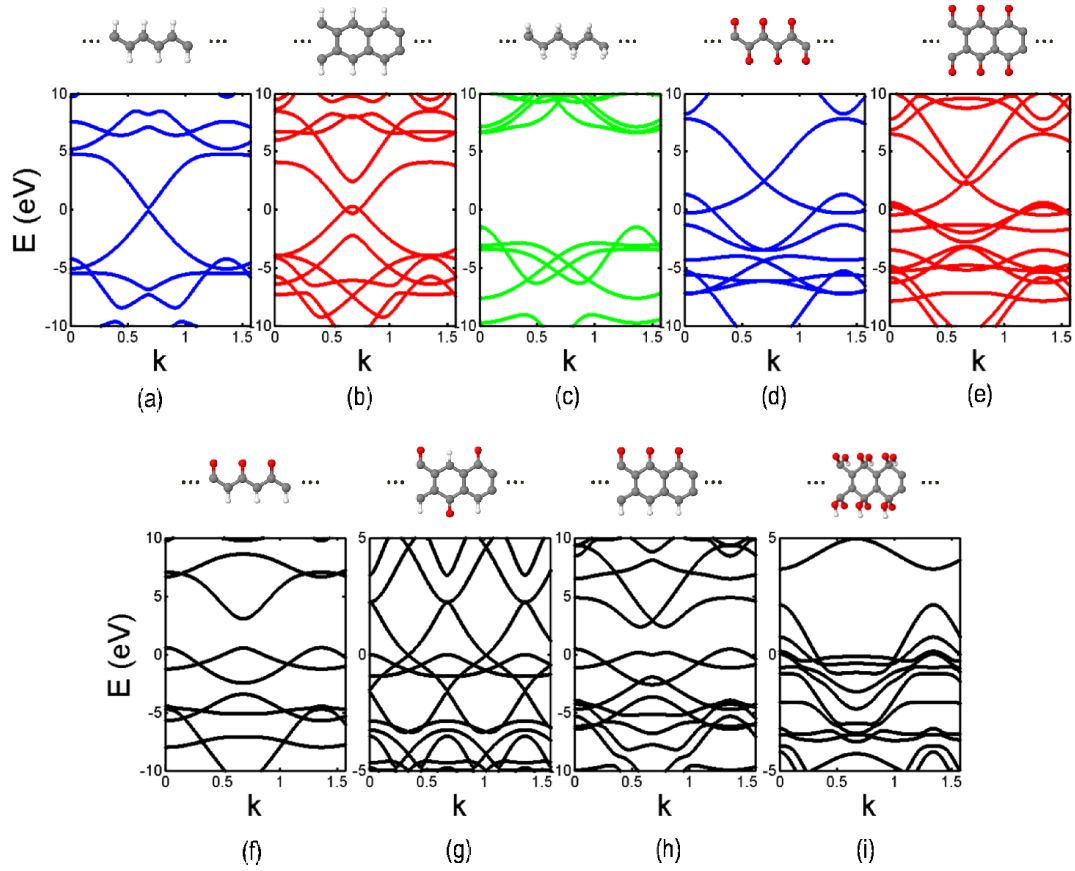


Figure 4.4. Band structure of (a) C-H atomic chain, (b) C-H benzene chain, (c) C-H₂ atomic chain, (d) C-O atomic chain, (e) C-O benzene chain, (f) C-O-H atomic chain, (g) C-O-H benzene chain 1 and (h) C-O-H benzene chain 2 (i) COOH benzene chain.

Figure 4.5b shows the calculated current-voltage curves (corresponding transmission coefficients $T(E)$ for electrons of energy E traversing the junctions are shown in figure 4.5d) for the five oxygen-terminated constrictions c_1 - c_5 of figure 4.5a, with widths varying from 3 nm (c_5) down to a single atomic chain (c_1). The chains and ribbons in figure 4.5a are connected to two hydrogen-terminated zigzag graphene electrodes. The blue curve of figure 4.5b shows that the current through the chain c_1 is higher than the current through the ribbon c_2 (green curve in figure 4.5b), particularly at higher bias voltages.

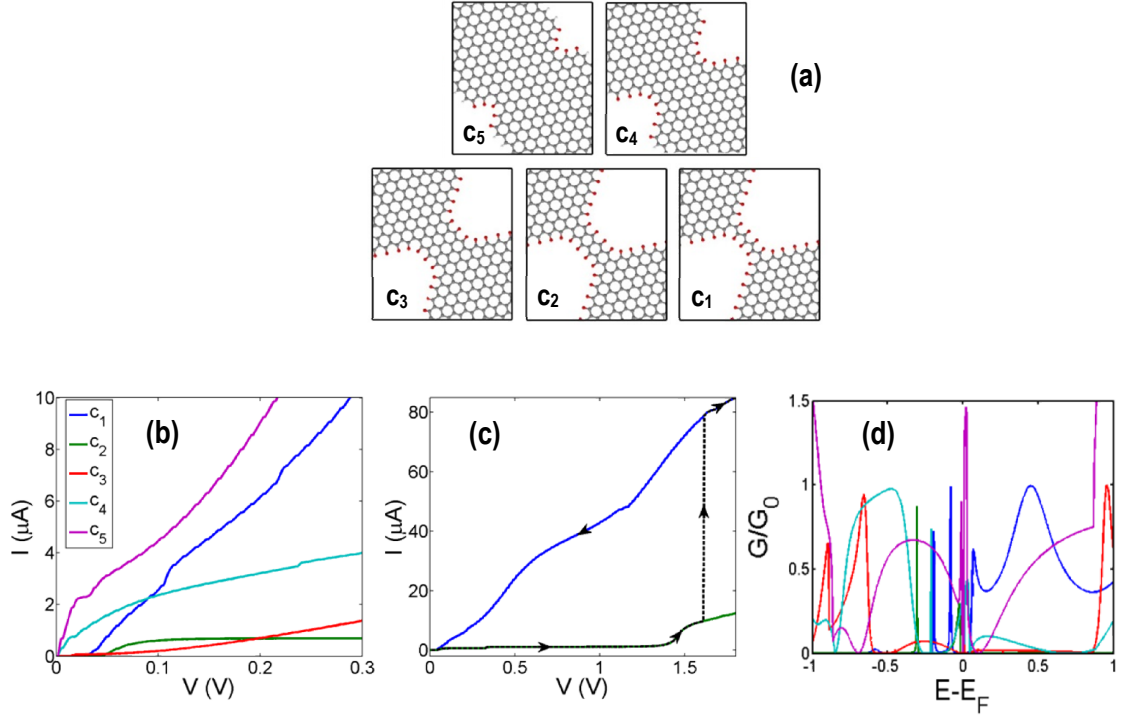


Figure 4.5. (a) Ideal configuration with reduced junction width down to the atomic chain, (b) Calculated current-voltage relations in oxygen-terminated junctions, (c) I–V characteristic for junctions c_1 and c_2 over a wider voltage range. Dashed lines and arrows indicate the current jump from double bond of structure c_2 to that of structure c_1 when an electroburning event occurs, (d) Calculated conductance vs. electrons energy.

To demonstrate that a two-path contact between two graphene electrodes typically has a lower conductance than a single-path contact, consider a graphene nanoribbon (on the left of figures 4.6a-d) connected to a carbon chain (on the right in figures 4.6a and 4.6b) or to hexagonal chains (figures 4.6c and 4.6d). To calculate the current flow through the junctions 4.6a-d and to study the effect of a bond breaking on the current when all other parameters fixed, we built a tight-binding Hamiltonian of each system as described in the methods section. Starting from junctions 4.6a and 4.6c with two pathways between the leads, I examined the effect of breaking a single bond to yield junction 4.6b and 4.6d respectively, with only one pathway each. As shown in figure 4.6, the current is increased when a bond broken. Moreover, even when the connection point $z=[0,1,2]$ of the linear chains is varied relative to the lower edge of the left-hand graphene nanoribbons, typically the single-bonded structures show higher currents. This demonstrates how constructive quantum interference in pico-scale graphene junctions produces

a significant jump in the current before breakdown. As an example, figure 4.6 shows that when only one of two single bonds in the hexagon–graphene junction is broken, the current increases by a factor of 11.5. This shows that in a junction formed from strong covalent bonds, the current in the one-pathway junction can be higher than in junctions with more than one pathway. This captures the feature revealed by the *DFT-NEGF* calculations on the structures of figure 4.1, that if bonds break in a filament with many pathways connecting two electrodes from different points, the current flow can increase. This result is highly non-classical and as shown in the next section, is a consequence of constructive quantum interference in pico-scale graphene junctions.

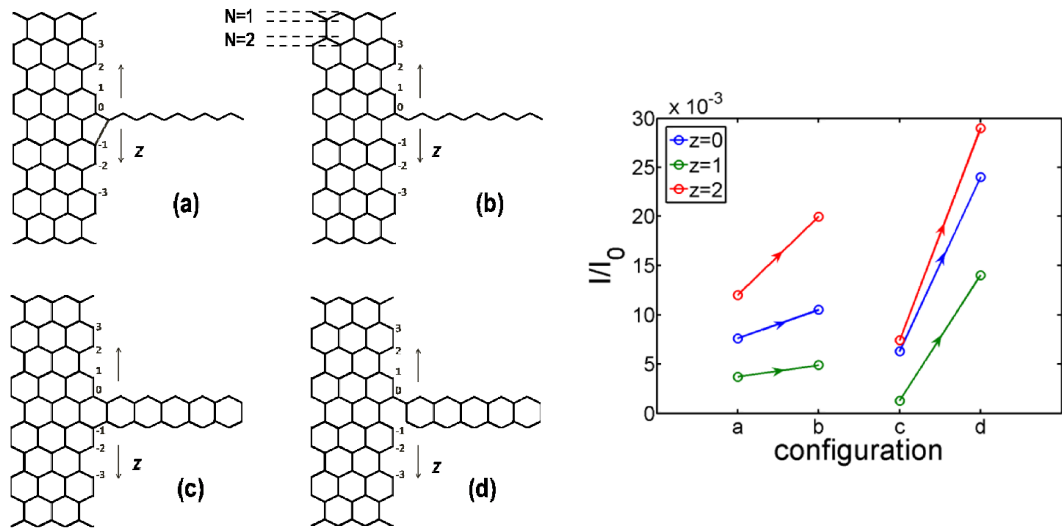


Figure 4.6. Each of figs a-d show an electrode formed from a graphene nanoribbon (on the left) in contact with an electrode (on the right) formed from a linear chain (a and b) or a chain of hexagons (c and d). For (a) and (c) the contact to the chain is via a single bond. For (b) and (d) the contact to the chain is via two bonds. For a voltage $V=20mV$, the circles show the current through each structure. The arrows indicate that upon switching from a two-bond contact to a single-bond contact, the current increases. $I_0=77.4 \mu A$ is the current carried by a quantum of conductance G_0 at 1 volt. The blue, green and red circles correspond to different positions $z=0, 1, 2$ of the contact.

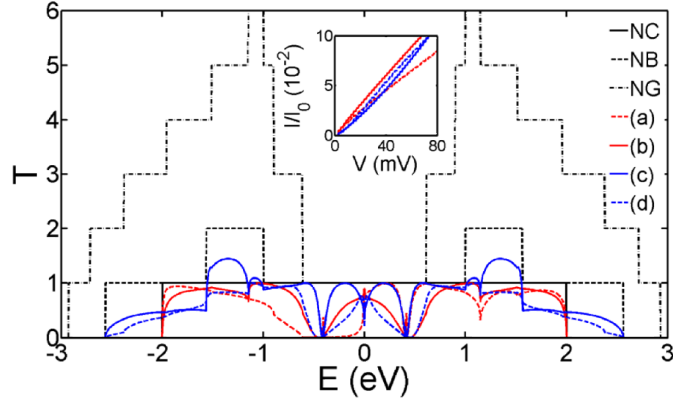


Figure 4.7. Transmission coefficient and number of open channels for the structures 4.6a-d. NC, NB and NG are the number of open channels in 1d carbon chain, benzene chain and 6N zigzag graphene ribbon, respectively. Inset: corresponding I - V relations and

To illustrate the origin of the jumps, figure 4.7 shows examples of the transmission coefficient and current-voltage relations calculated based on the simple tight-binding model with a single orbital per atom $\varepsilon_0 = 0eV$ and nearest neighbour couplings $= -1eV$, as described in method section. The graphs labelled NC, NB and NG are the number of open channels in a 1d carbon chain (right hand lead in figure 4.6a,b), benzene chain (right hand lead in figure 4.6c,d) and 6N-zigzag graphene ribbon (left hand lead in figure 4.6a-d), respectively. In all cases only one channel is opened at low energies, due to the band structure of the graphene nanoribbon. The corresponding transmission coefficients and I - V curves for the structures shown in figure 4.6a-d are labelled a-d in figure 4.7. The inset of figure 4.7 shows that the current of the structure shown in figure 4.6b is higher than all other structures in figure 4.6, reflecting the fact that graphene-1d carbon chain single junction carries higher current. When an extra coupling is added to the junction as shown in figure 4.6a; the current drops as shown by the dashed red curve in figure 4.7. Similarly for the hexagonal chain connected to the ribbon, cutting one of the two couplings (figure 4.6c to figure 4.6d) causes the current to increase, as shown by the dashed blue curves in figure 4.7.

To illustrate analytically the consequences of QI in few-pathway junctions, consider the structure shown in figure 4.8a, which consists of an atomic chain (in figure 4.8a this comprises atoms 2 and 3) connected to a single-channel lead terminating at atom $i=1$ and to a second

single-channel lead terminating at atom $j=4$. Now consider adding another atomic chain in parallel to the first, to yield the structure shown in figure 4.8b.

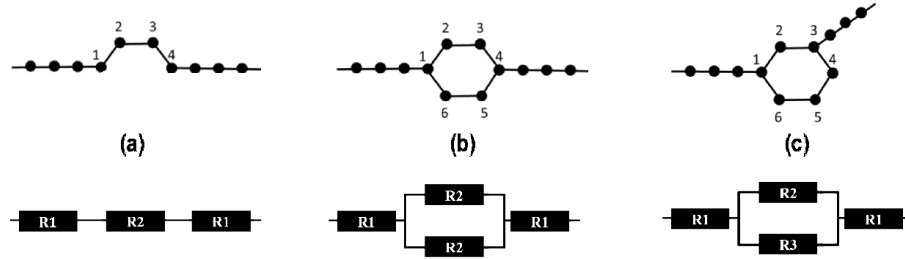


Figure 4.8. (a) shows a 1-d chain connected to 1d semi-infinite leads on the left and right, (b) shows two parallel chains forming a ring with para coupling to the leads and (c) shows two parallel chains with meta coupling to the leads. Classically this could be modeled with the serial and parallel resistors as the bottom row.

In the following, I shall show that the single-path structure of figure 4.8a has the highest of the three conductances. This trend is the opposite of what would be expected if the lines were classical resistors as shown in the bottom row of figure 4.8, and the circles were perfect connections. In that case (a) would have the lowest conductance and (c) the highest conductance since $G_a = 1/(2R_1 + R_2)$, $G_b = 1/(2R_1 + \frac{R_2}{2})$ and $G_c = 1/(2R_1 + \frac{R_2 R_3}{R_2 + R_3})$, G_a is always smaller than G_b and G_c . An intuitive understanding begins by noting that in the quantum case, electrical conductance is proportional to the transmission coefficient $T(E)$ of de Broglie waves of energy E passing through a given structure. If I neglect the lattice nature of the system, and consider the paths simply as classical waveguides, then for a wave propagating from the left hand end in each case, the bifurcations in (b) and (c) present an impedance mismatch, so that a fraction of the wave is reflected. Considering a waveguide of impedance Z with a bifurcation into two waveguides, for unit incident amplitude the total transmitted amplitude is $(2\sqrt{2}/3)$, and the transmitted intensity is $T = 8/9$. A similar analysis can be applied to a 1-D lattice formed of M semi-infinite chains. This is illustrated in figure 4.9a for $M = 2$ (a continuous chain) and figure 4.9b for $M = 3$ (a bifurcation).

Within a tight-binding or Hückel description of such systems, the transmission and reflection amplitudes r and t are obtained from matching conditions at site “0”. Then for electron energies E at the band centre (ie HOMO-LUMO gap centre, which coincides with the charge neutrality point in my model), it can be shown (see appendix A) that the transmission coefficient $T=|t|^2$ is given by

$$T = 4 (M-1) / M^2 \quad (4.1)$$

For $M = 2$, this formula yields $T=1$, as expected, because system 4.9a is just a continuous chain with no scattering. Since T cannot exceed unity, any changes can only serve to decrease T . For a bifurcation ($M = 3$), equation 4.1 yields $T=8/9$, which is the same result as a continuum bifurcated waveguide.

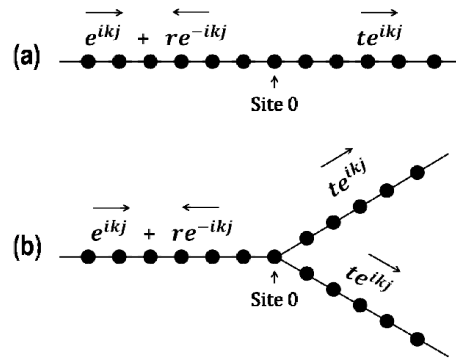


Figure 4.9. (a) A system with $M=2$ semi-infinite chains, centred on site 0. (b) A system with $M=3$ semi-infinite chains, centred on site 0. In each case, a plane wave from the left is either reflected with reflection amplitude r , or transmitted with transmission amplitude t .

When the two branches of figure 4.9b come together again to form a ring, there can be further interference effects, associated with additional reflections where the branches rejoin. These may serve to decrease or increase the transmission. At most the transmission will increase to $T=1$, but in general T will remain less than unity. It might be expected that the asymmetrical ring in figure 4.8c will be more likely to manifest destructive interference than the symmetrical ring in figure 4.8b. These intuitive conclusions from continuous and discrete models are confirmed by

the following rigorous analysis based on a tight-binding model of the actual atomic configurations, which captures the key features of the full DFT-NEGF calculations.

We consider a simple tight-binding (Hückel) description, with a single orbital per atom of ‘site energy’ ε_0 and nearest neighbour couplings $-\gamma$. As an example, for an infinite chain of such atoms, the Schrodinger’s equation takes the form: $\varepsilon_0\varphi_j - \gamma\varphi_{j-1} - \gamma\varphi_{j+1} = E\varphi_j$ for $-\infty < j < \infty$. The solution to this equation is $\varphi_j = e^{ikj}$, where $-\pi < k < \pi$ is wave vector. Substituting this into the Schrodinger’s equation yields the dispersion relation of $E = \varepsilon_0 - 2\gamma \cos k$. This means that such a 1d chain possesses a continuous band of energies between $E^- = \varepsilon_0 - 2\gamma$ and $E^+ = \varepsilon_0 + 2\gamma$. Since the 1-d leads in figure 4.8 are infinitely long and connected to macroscopic reservoirs (not shown), systems 4.8a-c are open systems. In these cases, the transmission coefficient $T(E)$ for electrons of energy E incident from the first lead is obtained by noting that the wave vector $k(E)$ of an electron of energy E traversing the ring is given by $k(E) = \cos^{-1}(\varepsilon_0 - E)/2\gamma$. When E coincides with the mid-point of the HOMO-LUMO gap of the bridge, ie when $E = \varepsilon_0$, this yields $k(E) = \pi/2$. Since $T(E)$ is proportional to $|1 + e^{ikL}|^2$, where L is the difference in path lengths between the upper and lower branches, for structure 4.8b, one obtains constructive interference, because $e^{ikL} = e^{i0} = 1$ and for structure 4.8c destructive interference, because $e^{ikL} = e^{i2k} = -1$. This result is unsurprising, because it is well known that the meta-coupled ring 4.8c should have a lower conductance than the para-coupled ring 4.8b [22]. More surprising is the fact the single-chain structure 4.8a has a higher conductance than both 4.8b and 4.8c. To illustrate this feature, we note (see appendix A for more details) that the ratio of the Green’s function G_{ring} of the structure of figure 4.8b to the Green’s function of the chain 4.8a, evaluated between the atoms 1 and 4 is:

$$G_{ring} / G_{chain} = (1-\alpha) / 2 \quad (4.2)$$

where α is a small self-energy correction due to the attachment of the leads. For small α , this means that the transmission of the linear chain at the gap centre is $4x$ higher than the

transmission of a para ring (because transmission is proportional to the square of the Green's function), which demonstrates that the conductances of both the two-path para and meta coupled structures are lower than that of a single-path chain. This result is the opposite of the behaviour discussed in [23], where the conductance of two identical parallel chains was found to be *4x higher* than that of a single chain. The prediction in ref. [23] is only applicable in the limit that the coupling of the branches to the nodes is weak, whereas in sp^2 -bonded graphene junctions, the coupling is strong.

I have addressed a hitherto mysterious feature of electro-burnt graphene junctions, namely a ubiquitous conductance enlargement at the final stages prior to nanogap formation. Through a combined experimental and theoretical investigation of electro-burnt graphene nanojunctions, we have demonstrated that conductance enlargement at the point of breaking a consequence of a transition from multiple-path to single-path quantum transport. This fundamental role of quantum interference was demonstrated using calculations based on *DFT-NEGF* methods, tight-binding modelling and analytic results for the structures of figure 4.8. Therefore these results suggest that conductance jumps provide a tool for characterising the atomic-scale properties of sp^2 -bonded junctions and in particular, conductance enlargement prior to junction rupture is a signal of the formation of electro-burnt junctions, with a current path formed from a single sp^2 -bond. Conductance enlargement is common, but does not occur in all electro-burnt nanojunctions, because direct jumps from two-path to broken junctions can occur. With greater control of the electro-burning feedback, my analysis suggests that one could create carbon-based atomic chains and filaments, which possess many of the characteristics of single molecules without the need for anchor groups, because the chains are already covalently bonded to electrodes.

Computational Methods: The Hamiltonian of the structures described in this chapter were obtained using density functional theory as described below or constructed from a simple tight-binding model with a single orbital per atom of site energy $\varepsilon_0 = 0$ and nearest neighbour couplings $\gamma = -1$.

DFT calculation: The optimized geometry and ground state Hamiltonian and overlap matrix elements of each structure was self-consistently obtained using the *SIESTA* [24] implementation of density functional theory (*DFT*). *SIESTA* employs norm-conserving pseudo-potentials to account for the core electrons and linear combinations of atomic orbitals to construct the valence states. The generalized gradient approximation (*GGA*) of the exchange and correlation functional is used with the Perdew-Burke-Ernzerhof parameterization (*PBE*) [25] a double- ζ polarized (*DZP*) basis set, a real-space grid defined with an equivalent energy cut-off of 250 Ry. The geometry optimization for each structure is performed to the forces smaller than 40 meV/Å. For the band structure calculation, given structure was sampled by a $1 \times 1 \times 500$ Monkhorst-Pack k -point grid.

Transport calculation: The mean-field Hamiltonian obtained from the converged *DFT* calculation or a simple tight-binding Hamiltonian was combined with our home-made implementation of the non-equilibrium Green's function method, the *GOLLUM* [26], to calculate the phase-coherent, elastic scattering properties of the each system consist of left (source) and right (drain) leads and the scattering region. The transmission coefficient $T(E)$ for electrons of energy E (passing from the source to the drain) is calculated via the relation:

$$T(E) = \text{Trace}(\Gamma_R(E)G^R(E)\Gamma_L(E)G^{R\dagger}(E)) \quad (4.3)$$

In this expression, $\Gamma_{L,R}(E) = i(\Sigma_{L,R}(E) - \Sigma_{L,R}^\dagger(E))$ describe the level broadening due to the coupling between left (L) and right (R) electrodes and the central scattering region, $\Sigma_{L,R}(E)$ are the retarded self-energies associated with this coupling and $G^R = (ES - H - \Sigma_L - \Sigma_R)^{-1}$ is the retarded Green's function, where H is the Hamiltonian and S is overlap matrix. Using obtained transmission coefficient ($T(E)$), the conductance could be calculated by Landauer formula ($G = G_0 \int dE T(E)(-\partial f/\partial E)$) where $G_0 = 2e^2/h$ is the conductance quantum. In addition, the current through the device at voltage V could be calculated as:

$$I(V) = \frac{2e}{h} \int_{-\frac{V}{2}}^{+\frac{V}{2}} dE T(E) [f(E - \frac{V}{2}) - f(E + \frac{V}{2})] \quad (4.4)$$

where $f(E) = (1 + \exp((E - E_F)/k_B T))^{-1}$ is the Fermi-Dirac distribution function, T is the temperature and $k_B = 8.6 \times 10^{-5} \text{ eV/K}$ is Boltzmann's constant.

Molecular dynamics: Left and right leads (figs 1c-e) were pulled in the transport direction by -0.1 \AA and 0.1 \AA every 40 fs (200 time steps) using the molecular dynamic code *LAMMPS* [27]. Energy minimization of the system was achieved in each 200 time steps by iteratively adjusting atomic coordinates using following parameters: the stopping energy of 0.2, the force tolerances of 10^{-8} , the maximum minimizer iterations of 1000 and the number of force/energy evaluations of 10000. The atoms were treated in the *REAX* force field model with *reax/c* parameterization and charge equilibration method as described in [27] with low and high cut-off of 0 and 10 for Taper radius and the charges equilibrated precision of 10^{-6} . The atomic positions are updated in 0.02 fs time steps at 400 K with constant volume and energy. The snapshot of the atomic coordinates was sampled every 665 time steps. The whole procedure performed twice and totally 42 configuration extracted. Each of obtained set of coordinates was used as an initial set of coordinates for the subsequent self-consistent *DFT* loops as described above.

Experimental Methods: Similar to previous studies using few-layer graphene flakes, the feedback controlled electro-burning is performed in air at room temperature. The feedback-controlled electro-burning of the SLG devices [28] is based on the same method as previously used for electro-burning of few-layer graphene flakes [11] and electro-migration of metal nanowires [29]. A voltage (V) applied between the two metal electrodes is ramped up at a rate of 0.75 V/s , while the current (I) is recorded with a 200 \mu s sampling rate. When the feedback condition, which is set at a drop ΔI of the current within the past 15 mV is met the voltage is ramped down to zero at a rate of 225 V/s . After each voltage ramp the resistance of the SGL device is measured and the process is repeated until the low-bias resistance exceeds $500 \text{ M}\Omega$. To prevent the SGL device from burning too abruptly at the initial voltage ramps, the feedback

condition is adjusted for the each voltage ramp depending on the voltage at which the previous current drop occurred.

References

- [1] E. Burzurí, F. Prins, and H. S. van der Zant, "Characterization of Nanometer-Spaced Few-Layer Graphene Electrodes," *Graphene*, vol. 1, p. 26, 2012.
- [2] X. Deng, Z. Zhang, G. Tang, Z. Fan, and C. Yang, "Spin filtering and large magnetoresistance behaviors in carbon chain-zigzag graphene nanoribbon nanojunctions," *Physics Letters A*, vol. 378, pp. 1540-1547, 2014.
- [3] Z. Zanolli, G. Onida, and J.-C. Charlier, "Quantum spin transport in carbon chains," *ACS nano*, vol. 4, pp. 5174-5180, 2010.
- [4] B. Akdim and R. Pachter, "Switching behavior of carbon chains bridging graphene nanoribbons: effects of uniaxial strain," *ACS nano*, vol. 5, pp. 1769-1774, 2011.
- [5] L. Shen, M. G. Zeng, S. W. Yang, C. Zhang, X. F. Wang, and Y. P. Feng, "Electron Transport Properties of Atomic Carbon Nanowires between Graphene Electrodes," *Journal of the American Chemical Society*, vol. 132, pp. 11481-11486, 2010.
- [6] V. L. Katkov and V. A. Osipov, "Planar graphene tunnel field-effect transistor," *Applied Physics Letters*, vol. 104, p. 053102, 2014.
- [7] C. Joachim and M. A. Ratner, "Molecular electronics: Some views on transport junctions and beyond," *Proceedings of the National Academy of Sciences of the United States of America*, vol. 102, pp. 8801-8808, 2005.
- [8] Y. He, H. Dong, T. Li, C. Wang, W. Shao, Y. Zhang, *et al.*, "Graphene and graphene oxide nanogap electrodes fabricated by atomic force microscopy nanolithography," *Applied Physics Letters*, vol. 97, p. 133301, 2010.

- [9] B. Standley, W. Bao, H. Zhang, J. Bruck, C. N. Lau, and M. Bockrath, "Graphene-Based Atomic-Scale Switches," *Nano Letters*, vol. 8, pp. 3345-3349, 2008.
- [10] H. M. Wang, Z. Zheng, Y. Y. Wang, J. J. Qiu, Z. B. Guo, Z. X. Shen, *et al.*, "Fabrication of graphene nanogap with crystallographically matching edges and its electron emission properties," *Applied Physics Letters*, vol. 96, p. 023106, 2010.
- [11] F. Prins, A. Barreiro, J. W. Ruitenber, J. S. Seldenthuis, N. Aliaga-Alcalde, L. M. K. Vandersypen, *et al.*, "Room-Temperature Gating of Molecular Junctions Using Few-Layer Graphene Nanogap Electrodes," *Nano Letters*, vol. 11, pp. 4607-4611, 2011.
- [12] F. Börrnert, A. Barreiro, D. Wolf, M. I. Katsnelson, B. Büchner, L. M. K. Vandersypen, *et al.*, "Lattice Expansion in Seamless Bilayer Graphene Constrictions at High Bias," *Nano Letters*, vol. 12, pp. 4455-4459, 2012.
- [13] A. Barreiro, H. S. J. van der Zant, and L. M. K. Vandersypen, "Quantum Dots at Room Temperature Carved out from Few-Layer Graphene," *Nano Letters*, vol. 12, pp. 6096-6100, 2012.
- [14] C. Nef, L. Posa, P. Makk, W. Fu, A. Halbritter, C. Schonenberger, *et al.*, "High-yield fabrication of nm-size gaps in monolayer CVD graphene," *Nanoscale*, vol. 6, pp. 7249-7254, 2014.
- [15] ITRS, "International Technology Roadmap for Semiconductors," 2012.
- [16] M. Ratner, "A brief history of molecular electronics," *Nat Nano*, vol. 8, pp. 378-381, 2013.
- [17] O. Cretu, A. R. Botello-Mendez, I. Janowska, C. Pham-Huu, J.-C. Charlier, and F. Banhart, "Electrical transport measured in atomic carbon chains," *Nano letters*, vol. 13, pp. 3487-3493, 2013.

- [18] S. V. Aradhya and L. Venkataraman, "Single-molecule junctions beyond electronic transport," *Nat Nano*, vol. 8, pp. 399-410, 2013.
- [19] A. Barreiro, F. Börrnert, M. H. Rummeli, B. Büchner, and L. M. K. Vandersypen, "Graphene at High Bias: Cracking, Layer by Layer Sublimation, and Fusing," *Nano Letters*, vol. 12, pp. 1873-1878, 2012.
- [20] Y. Lu, C. A. Merchant, M. Drndić, and A. T. C. Johnson, "In Situ Electronic Characterization of Graphene Nanoconstrictions Fabricated in a Transmission Electron Microscope," *Nano Letters*, vol. 11, pp. 5184-5188, 2011.
- [21] Y. Wu, V. Perebeinos, Y.-m. Lin, T. Low, F. Xia, and P. Avouris, "Quantum Behavior of Graphene Transistors near the Scaling Limit," *Nano Letters*, vol. 12, pp. 1417-1423, 2012.
- [22] J. Rincón, K. Hallberg, A. A. Aligia, and S. Ramasesha, "Quantum Interference in Coherent Molecular Conductance," *Physical Review Letters*, vol. 103, p. 266807, 2009.
- [23] M. Magoga and C. Joachim, "Conductance of molecular wires connected or bonded in parallel," *Physical Review B*, vol. 59, pp. 16011-16021, 1999.
- [24] J. M. Soler, E. Artacho, J. D. Gale, A. García, J. Junquera, P. Ordejón, *et al.*, "The SIESTA method for ab initio order- N materials simulation," *Journal of Physics: Condensed Matter*, vol. 14, p. 2745, 2002.
- [25] J. P. Perdew, K. Burke, and M. Ernzerhof, "Generalized Gradient Approximation Made Simple," *Physical Review Letters*, vol. 77, pp. 3865-3868, 1996.
- [26] J. Ferrer, C. Lambert, V. Garcia-Suarez, D. Zsolt Manrique, D. Visontai, L. Oroszlani, *et al.*, "GOLLUM: a next-generation simulation tool for electron, thermal and spin transport," *New Journal of Physics*, vol. 16, p. 093029, 2014.

- [27] S. Plimpton, "Fast parallel algorithms for short-range molecular dynamics," *Journal of Computational Physics*, vol. 117, pp. 1-19, 1995.
- [28] C. S. Lau, J. A. Mol, J. H. Warner, and G. A. D. Briggs, "Nanoscale control of graphene electrodes," *Physical Chemistry Chemical Physics*, vol. 16, pp. 20398-20401, 2014.
- [29] A. Mangin, A. Anthore, M. L. Della Rocca, E. Boulat, and P. Lafarge, "Reduced work functions in gold electromigrated nanogaps," *Physical Review B*, vol. 80, p. 235432, 2009.

Chapter 5

A Magic-Ratio Rule (MRR)

In this chapter, I demonstrate a new magic ratio rule (*MRR*), which captures the contribution of connectivity to the electrical conductance of graphene-like aromatic molecules. When one electrode is connected to a site i and the other is connected to a site i' of a particular molecule, I assign the molecule a *magic integer* $M_{ii'}$. Two molecules with the same aromatic core, but different pairs of electrode connection sites (i, i' and j, j' respectively) possess different magic integers $M_{ii'}$ and $M_{jj'}$. Based on connectivity alone, I predict that when the coupling to electrodes is weak and the Fermi energy of the electrodes lies close to the centre of the HOMO-LUMO gap, the ratio of their conductances is equal to $(M_{ii'}/M_{jj'})^2$. The *MRR* is exact and parameter free for a tight binding representation of a molecule and a qualitative guide for real molecules.

The results presented in this chapter were published in: Geng, et al. Magic ratios for connectivity-driven electrical conductance of graphene-like molecules, 2015, Journal of the American Chemical Society (JACS), 137 (13), 4469-4476

This study is a collaborative work and the experiment has been carried out in the University of Bern.

Charge transport through polycyclic aromatic hydrocarbons (PAHs) has attracted intensive attention in recent years [1, 2], partly due to their role in the design and development of molecular electronic devices [3-6]. Since PAHs are well-defined and defect free, they also provide model systems for understanding transport in graphene, treated as an infinite alternant PAH, and graphene-based nanostructures [7-9]. When a single molecule is connected to metallic electrodes, electrons passing through the molecule from one electrode to the other can remain phase coherent, even at room temperature [10, 11]. This has led to a great deal of discussion about the role of quantum interference (QI) in determining the electrical conductance of single molecules [12-21], culminating in a series of recent experiments revealing room-temperature signatures of QI [22-30].

Both experiment and theory have focused primarily on elucidating the conditions for the appearance of constructive or destructive interference. In the simplest case, where electrons are injected at the Fermi energy E_F of the electrodes, constructive QI arises when E_F coincides with a delocalized energy level E_n of the molecule. Similarly a simple form of destructive QI occurs when E_F coincides with the energy E_b of a bound state located on a pendant moiety [31, 32]. In practice, unless energy levels are tuned by electrostatic, electrochemical or mechanical gating, molecules located within a junction rarely exhibit these types of QI, because E_F is usually located in the HOMO-LUMO (H-L) gap. For this reason, discussions have often focussed on conditions for destructive or constructive QI when E_F is located at the centre of the H-L gap. For the purpose of identifying conditions for destructive QI within the delocalised π -system, a useful conceptual approach is to represent molecules by lattices of connected sites ($C(sp^2)$ atoms), such as those shown in figure 5.1, in which 1a represents a benzene ring, 1b represents naphthalene, 1c represents anthracene and 1d represents anthanthrene. Such abstractions highlight the role of connectivity in determining the presence or absence of destructive QI. For example, the lattices of figure 5.1 are bipartite, being composed of equal numbers of ‘primed’ and ‘unprimed’ sites, such that primed sites (labelled by primed integers such as $1', 2', 3'$) are connected to unprimed sites only (labelled by non-primed integers such as $1, 2, 3$) and vice versa. It is well known [33-38], (see also the appendix B) that if electrodes are

connected to two sites which are both primed or both unprimed, then destructive interference occurs and the contribution from π -orbitals to the electrical conductance G vanishes. For a benzene ring this corresponds to the well-known case of meta-coupled electrodes, but more generally it holds for any bipartite lattice.

Studies of such lattices have yielded a variety of simple rules for the appearance of destructive QI [21, 33-38], for which the π -orbital contribution to G vanishes. The aim of this chapter is to elucidate a simple rule for determining the non-zero values of electrical conductance arising from constructive QI in aromatic molecules. At first sight, this task seems rather daunting, because there is only one conductance (*i.e.* $G = 0$) when QI is destructive, whereas there are many possible non-zero values of G when QI is constructive. Furthermore, the non-zero values of conductances in the presence of constructive QI depend on the strength and detailed nature of the contacts to electrodes.

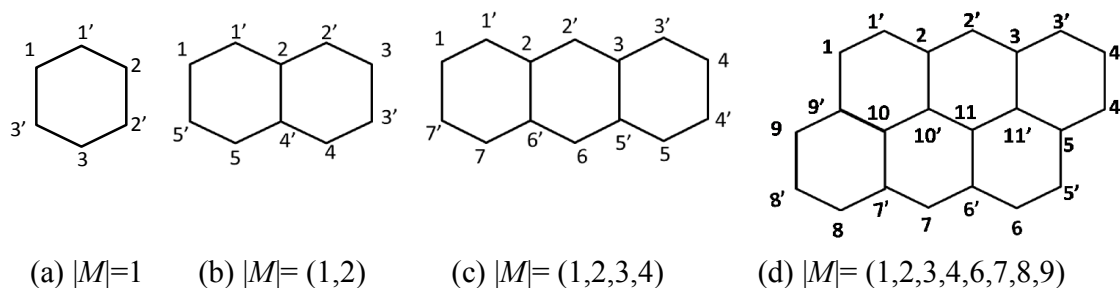


Figure 5.1. Four examples of bipartite lattices, with the magnitude of their magic numbers shown underneath each lattice. (a) represents benzene, (b) naphthalene, (c) anthracene and (d) anthanthrene.

Remarkably, in what follows, I demonstrate a “*magic ratio rule*” based on tables of quantum numbers M_{ii} , which capture the contribution of connectivity to the electrical conductance of graphene-like aromatic molecules, or molecules with graphene-like cores, when one electrode is connected to

an ‘unprimed’ site i and the other is connected to a ‘primed’ site i' . In particle physics, quantum numbers such as ‘charm’ and ‘colour’ are assigned to elementary particles. In the case of lattices such as those in figure 5.1, I refer to these new quantum numbers as ‘magic integers $M_{ii'}$ ’. For each of the molecules shown in figure 5.1, the allowed values of $|M_{ii'}|$ are shown beneath each lattice. Clearly the spectrum of magic integers increases with size of the aromatic core. The precise values of $M_{ii'}$ are not trivial, since for example $M_{ii'} = 5$ is missing from the set of anthanthrene integers.

	1'	2'	3'	4'	5'
1	-2	1	-1	1	-1
2	-1	-1	1	-1	1
3	1	-2	-1	1	-1
4	-1	2	-2	-1	1
5	2	-1	1	-1	-2

Table 5.1. The M-table of MIs $M_{ii'}$ for the naphthalene lattice of figure 5.1b.

Magic integers (MIs) capture the complexity of interference patterns created by electrons at the centre of HOMO-LUMO gap and allow the prediction of conductance ratios *via* the following ‘magic ratio rule’ (MRR), which states that “the ratio of conductances of two molecules is equal to the squares of the ratios of their magic integers.” Clearly, when comparing conductances of the same aromatic core, but different contacts, the signs of the MIs are irrelevant. This rule is derived in the appendix B. To each lattice such as those in figure 5.1, the quantum numbers $M_{ii'}$ form a table of MIs, which I refer to as M-tables. As shown in the table 5.3, for the benzene ring 1a, this is a 3×3 table, with all entries equal to ± 1 , so that $|M_{ii'}| = 1$ is the only possibility and therefore as expected, para (*i.e.* 3,1') or ortho (3,2' or 3,3') connectivities yield the same electrical conductances. For the naphthalene lattice 1b, the 5×5 M-table is shown in table 5.1. As expected from symmetry, this table

shows the conductances associated with contact sites 1,1' and 5,5' are equal and proportional to $(2)^2 = 4$. It also shows that the conductance with contact sites 4,2' or 5,1' would take the same value, which is a less obvious result.

	1'	2'	3'	4'	5'	6'	7'	8'	9'	10'	11'
1	-9	7	-4	4	-1	1	-1	1	-1	2	-3
2	-1	-7	4	-4	1	-1	1	-1	1	-2	3
3	1	-3	-4	4	-1	1	-1	1	-1	2	-3
4	-1	3	-6	-4	1	-1	1	-1	1	-2	3
5	1	-3	6	-6	-1	1	-1	1	-1	2	-3
6	-1	3	-6	6	-9	-1	1	-1	1	-2	3
7	3	-9	8	-8	7	-7	-3	3	-3	6	1
8	-6	8	-6	6	-4	4	-4	-6	6	-2	-2
9	6	-8	6	-6	4	-4	4	-4	-6	2	2
10	3	1	-2	2	-3	3	-3	3	-3	-4	1
11	-2	6	-2	2	2	-2	2	-2	2	-4	-4

Table 5.2. The M-table for the anthanthrene lattice of figure 5.1d. Note that the first (row) index is non-primed and the second (column) index is primed.

The MRR is an exact formula for conductance ratios of tight-binding representations of molecules in the weak coupling limit, when the Fermi energy is located at the centre of the HOMO-LUMO (H-L) gap. It does not depend on the size of the H-L gap and is independent of asymmetries in the contacts. In what follows, I explore the real-life implications of the MRR by evaluating the conductance ratio of two molecules both experimentally carried out by our collaborator and using density functional theory (*DFT*) combined with non-equilibrium Green's functions.

Molecule	C-table	M-table																																																																																																																																
	<table border="1"> <thead> <tr> <th></th> <th>1</th> <th>2</th> <th>3</th> </tr> </thead> <tbody> <tr> <th>1'</th> <td>1</td> <td>1</td> <td>0</td> </tr> <tr> <th>2'</th> <td>0</td> <td>1</td> <td>1</td> </tr> <tr> <th>3'</th> <td>1</td> <td>0</td> <td>1</td> </tr> </tbody> </table>		1	2	3	1'	1	1	0	2'	0	1	1	3'	1	0	1	<table border="1"> <thead> <tr> <th></th> <th>1'</th> <th>2'</th> <th>3'</th> </tr> </thead> <tbody> <tr> <th>1</th> <td>1</td> <td>-1</td> <td>1</td> </tr> <tr> <th>2</th> <td>1</td> <td>1</td> <td>-1</td> </tr> <tr> <th>3</th> <td>-1</td> <td>1</td> <td>1</td> </tr> </tbody> </table>		1'	2'	3'	1	1	-1	1	2	1	1	-1	3	-1	1	1																																																																																																
	1	2	3																																																																																																																															
1'	1	1	0																																																																																																																															
2'	0	1	1																																																																																																																															
3'	1	0	1																																																																																																																															
	1'	2'	3'																																																																																																																															
1	1	-1	1																																																																																																																															
2	1	1	-1																																																																																																																															
3	-1	1	1																																																																																																																															
	<table border="1"> <thead> <tr> <th></th> <th>1</th> <th>2</th> <th>3</th> <th>4</th> <th>5</th> </tr> </thead> <tbody> <tr> <th>1'</th> <td>1</td> <td>1</td> <td>0</td> <td>0</td> <td>0</td> </tr> <tr> <th>2'</th> <td>0</td> <td>1</td> <td>1</td> <td>0</td> <td>0</td> </tr> <tr> <th>3'</th> <td>0</td> <td>0</td> <td>1</td> <td>1</td> <td>0</td> </tr> <tr> <th>4'</th> <td>0</td> <td>1</td> <td>0</td> <td>1</td> <td>1</td> </tr> <tr> <th>5'</th> <td>1</td> <td>0</td> <td>0</td> <td>0</td> <td>1</td> </tr> </tbody> </table>		1	2	3	4	5	1'	1	1	0	0	0	2'	0	1	1	0	0	3'	0	0	1	1	0	4'	0	1	0	1	1	5'	1	0	0	0	1	<table border="1"> <thead> <tr> <th></th> <th>1'</th> <th>2'</th> <th>3'</th> <th>4'</th> <th>5'</th> </tr> </thead> <tbody> <tr> <th>1</th> <td>-2</td> <td>1</td> <td>-1</td> <td>1</td> <td>-1</td> </tr> <tr> <th>2</th> <td>-1</td> <td>-1</td> <td>1</td> <td>-1</td> <td>1</td> </tr> <tr> <th>3</th> <td>1</td> <td>-2</td> <td>-1</td> <td>1</td> <td>-1</td> </tr> <tr> <th>4</th> <td>-1</td> <td>2</td> <td>-2</td> <td>-1</td> <td>1</td> </tr> <tr> <th>5</th> <td>2</td> <td>-1</td> <td>1</td> <td>-1</td> <td>-2</td> </tr> </tbody> </table>		1'	2'	3'	4'	5'	1	-2	1	-1	1	-1	2	-1	-1	1	-1	1	3	1	-2	-1	1	-1	4	-1	2	-2	-1	1	5	2	-1	1	-1	-2																																																								
	1	2	3	4	5																																																																																																																													
1'	1	1	0	0	0																																																																																																																													
2'	0	1	1	0	0																																																																																																																													
3'	0	0	1	1	0																																																																																																																													
4'	0	1	0	1	1																																																																																																																													
5'	1	0	0	0	1																																																																																																																													
	1'	2'	3'	4'	5'																																																																																																																													
1	-2	1	-1	1	-1																																																																																																																													
2	-1	-1	1	-1	1																																																																																																																													
3	1	-2	-1	1	-1																																																																																																																													
4	-1	2	-2	-1	1																																																																																																																													
5	2	-1	1	-1	-2																																																																																																																													
	<table border="1"> <thead> <tr> <th></th> <th>1</th> <th>2</th> <th>3</th> <th>4</th> <th>5</th> <th>6</th> <th>7</th> </tr> </thead> <tbody> <tr> <th>1'</th> <td>1</td> <td>1</td> <td>0</td> <td>0</td> <td>0</td> <td>0</td> <td>0</td> </tr> <tr> <th>2'</th> <td>0</td> <td>1</td> <td>1</td> <td>0</td> <td>0</td> <td>0</td> <td>0</td> </tr> <tr> <th>3'</th> <td>0</td> <td>0</td> <td>1</td> <td>1</td> <td>0</td> <td>0</td> <td>0</td> </tr> <tr> <th>4'</th> <td>0</td> <td>0</td> <td>0</td> <td>1</td> <td>1</td> <td>0</td> <td>0</td> </tr> <tr> <th>5'</th> <td>0</td> <td>0</td> <td>1</td> <td>0</td> <td>1</td> <td>1</td> <td>0</td> </tr> <tr> <th>6'</th> <td>0</td> <td>1</td> <td>0</td> <td>0</td> <td>0</td> <td>1</td> <td>1</td> </tr> <tr> <th>7'</th> <td>1</td> <td>0</td> <td>0</td> <td>0</td> <td>0</td> <td>0</td> <td>1</td> </tr> </tbody> </table>		1	2	3	4	5	6	7	1'	1	1	0	0	0	0	0	2'	0	1	1	0	0	0	0	3'	0	0	1	1	0	0	0	4'	0	0	0	1	1	0	0	5'	0	0	1	0	1	1	0	6'	0	1	0	0	0	1	1	7'	1	0	0	0	0	0	1	<table border="1"> <thead> <tr> <th></th> <th>1'</th> <th>2'</th> <th>3'</th> <th>4'</th> <th>5'</th> <th>6'</th> <th>7'</th> </tr> </thead> <tbody> <tr> <th>1</th> <td>-3</td> <td>2</td> <td>-1</td> <td>1</td> <td>-1</td> <td>1</td> <td>-1</td> </tr> <tr> <th>2</th> <td>-1</td> <td>-2</td> <td>1</td> <td>-1</td> <td>1</td> <td>-1</td> <td>1</td> </tr> <tr> <th>3</th> <td>1</td> <td>-2</td> <td>-1</td> <td>1</td> <td>-1</td> <td>1</td> <td>-1</td> </tr> <tr> <th>4</th> <td>-1</td> <td>2</td> <td>-3</td> <td>-1</td> <td>1</td> <td>-1</td> <td>1</td> </tr> <tr> <th>5</th> <td>1</td> <td>-2</td> <td>3</td> <td>-3</td> <td>-1</td> <td>1</td> <td>-1</td> </tr> <tr> <th>6</th> <td>-2</td> <td>4</td> <td>-2</td> <td>2</td> <td>-2</td> <td>-2</td> <td>2</td> </tr> <tr> <th>7</th> <td>3</td> <td>-2</td> <td>1</td> <td>-1</td> <td>1</td> <td>-1</td> <td>-3</td> </tr> </tbody> </table>		1'	2'	3'	4'	5'	6'	7'	1	-3	2	-1	1	-1	1	-1	2	-1	-2	1	-1	1	-1	1	3	1	-2	-1	1	-1	1	-1	4	-1	2	-3	-1	1	-1	1	5	1	-2	3	-3	-1	1	-1	6	-2	4	-2	2	-2	-2	2	7	3	-2	1	-1	1	-1	-3
	1	2	3	4	5	6	7																																																																																																																											
1'	1	1	0	0	0	0	0																																																																																																																											
2'	0	1	1	0	0	0	0																																																																																																																											
3'	0	0	1	1	0	0	0																																																																																																																											
4'	0	0	0	1	1	0	0																																																																																																																											
5'	0	0	1	0	1	1	0																																																																																																																											
6'	0	1	0	0	0	1	1																																																																																																																											
7'	1	0	0	0	0	0	1																																																																																																																											
	1'	2'	3'	4'	5'	6'	7'																																																																																																																											
1	-3	2	-1	1	-1	1	-1																																																																																																																											
2	-1	-2	1	-1	1	-1	1																																																																																																																											
3	1	-2	-1	1	-1	1	-1																																																																																																																											
4	-1	2	-3	-1	1	-1	1																																																																																																																											
5	1	-2	3	-3	-1	1	-1																																																																																																																											
6	-2	4	-2	2	-2	-2	2																																																																																																																											
7	3	-2	1	-1	1	-1	-3																																																																																																																											

Table 5.3. Examples of M-tables of magic integers for Benzene, Naphthalene and Anthracene.

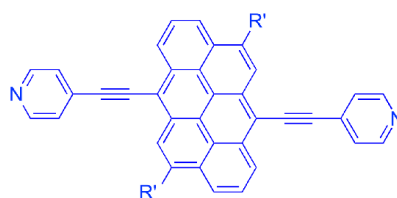
I first restrict the discussion to bipartite lattices with equal numbers of primed and non-primed sites. To obtain the M-table for a given lattice, first construct a connectivity table C, with rows labelled by primed integers and columns by unprimed integers, such that the entry $C_{i'i}$ contains a '1' if sites i' and i are connected and zero otherwise. The corresponding M-table M is then defined to be the transpose of the cofactor matrix of C. This means that if the determinant of the matrix obtained by removing the i th column and i' th row of C is denoted $d_{i'i'}$, then $M_{i'i'} = (-1)^{(i+i')}d_{i'i'}$.

To aid the experimental investigation of the MRR, it is helpful to select two molecules exhibiting constructive QI with very different values of $M_{i'i'}$ and therefore, based on the M-table of table 5.2, I compared the conductance of molecule **1**, derived from an anthanthrene core as shown in scheme 5.1, with an MI of $M_{15'} = -1$, with that of the corresponding molecule **2**, for which $M_{72'} = -9$. This means that the MRR prediction for the electrical conductance of the core of **2** is $(9)^2 = 81$ times higher than that of the core of **1**. Below I demonstrate that even though **1** and **2** differ from the idealisation of figure 5.1d, this ratio is reflected in employed a mechanically controllable break junction (MCBJ) measurements of their conductances, which reveal that the single-molecule conductance of

short-axis contacted anthanthrene **2** is approximately 79 times higher than that of its long-axis contacted analogue **1**.



1 R = -OC₈H₁₇



2 R' = 4-(2-ethylhexyloxy)phenyl

Scheme 5.1. Two molecules studied experimentally, each with the anthanthrene core. Following the numbering convention in figure 5.1d, **1** is long-axis contacted with connection sites 1,5' and **2** is short-axis contacted with connection sites 7,2'.

Anthanthrene is the compact dibenzo[*def,mno*]chrysene molecule, which together with its angular counterpart, dibenzo[*b,def*]chrysene, represents a promising building block for many applications in the field of organic electronic materials [39-41]. Advantageously, what sets these prototypical non-linear PAHs apart from the linearly fused acenes, such as anthracene and pentacene, is the enhanced stability towards degradative chemical reactions and photooxidation [42-44]. To measure their single-molecule electrical conductances, a *MCBJ* setup capable of operating in solution is employed. In a *MCBJ* experiment, molecular junctions are formed by opening and closing a nanogap between two gold electrodes. Further details of conductance measurements could be found in [22, 45, 46].

Figure 5.2a displays typical conductance (G) versus distance (Δz) stretching traces, as plotted on a semi-logarithmic scale, and recorded for 0.1 mM molecules **1** and **2** in a solution of mesitylene and THF (4:1 v/v) using the MCBJ technique. For reference, two traces (black curves) representing the molecule-free solution is also plotted, which reveal classical tunnelling characteristics, *i.e.* an exponential decrease of the conductance upon junction elongation. After the Au-Au contacts break, the formation of molecular junctions is signalled by the presence of additional plateaus in the range $10^{-3} G_0 \geq G \geq 10^{-7.0} G_0$ ($G_0 = 2e^2/h$, quantum conductance). Typically 1000 individual conductance versus relative displacement traces (G vs Δz) were recorded for both molecules **1** and **2**, and analysed further by constructing all-data-point histograms without any data selection to extract statistically significant results from the different junction configurations (as shown in figure 5.2b). The prominent peaks between $10^{-7} G_0 < G < 10^{-4} G_0$ represent molecular junction features. The statistically-most-probable conductance of each molecular junction is obtained by fitting Gaussians to the characteristic maxima in the one-dimensional (1D) conductance histograms. As shown in figure 5.2b, the most probable conductance for the anthanthrene molecules is $10^{-4.6} G_0$ for **2** and $10^{-6.1} G_0$ for **1**, indicating that the conductance of molecule **2** is a factor of 32 higher than the conductance of **1**. However, it should be noted that the most probable conductance results from the molecular conductances associated with different contact configurations and a variety of electrode separations. To facilitate comparison with theory, it is of interest to explore the molecular conductance through fully stretched junctions, for which contact occurs via the pyridyl groups. Quantitative analyses of 2D histograms (figure 5.2c,d) reveals the evolution of molecular orientations and junction configurations during the stretching process.

The statistically averaged conductance–distance traces (figure 5.2c,d) exhibit “through-space” tunnelling at the beginning of the stretching process (< 0.3 nm) and then a clear molecular plateau with slightly different conductance decays for both molecules. The analysis of stability and junction formation probability was performed by constructing the stretching distance distribution shown in the inset of figure 5.2c,d. The single peak distribution suggests the junction formation

probability of the anthanthrene-based molecules could reach up to $\sim 100\%$. The single maximum in the plateau-length histogram represents the most probable relative characteristic stretching distance $\Delta z^* = 1.7$ nm for **1**, and 1.5 nm for **2**.

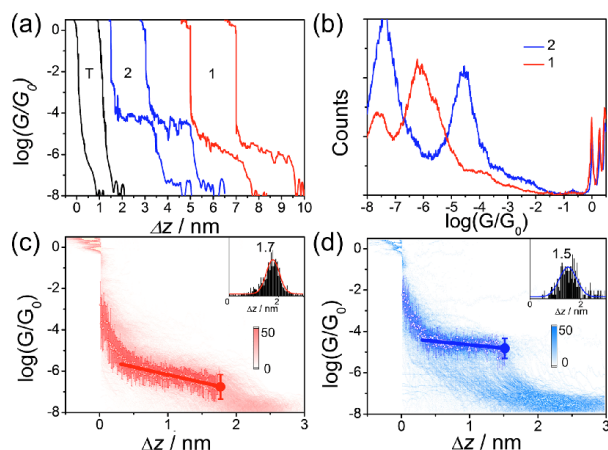


Figure 5.2. (a) Individual conductance-distance traces of **1** (red) and **2** (blue) using THF/mesitylene; (b) conductance histograms of **1** (red) and **2** (blue), the sharp peak around $10^{-7.5} G_0$ is attributed to the noise limit of *MCBJ* setup under the current experimental condition; (c,d) 2D conductance histograms of **1** (c) and **2** (d) with statistically averaged conductance–distance traces (circles) with variation indicated by the standard deviation (bar) and linear fitting (line). The solid circles represent the last data point in the linear fitting before junction rupture, and the solid error bar was determined from the Gaussian fitting of the $\log G$ peak of last data point. Insets: Stretching distance distributions determined from $0.1 G_0$ to $10^{-7} G_0$ (c) and from $0.1 G_0$ to $10^{-5.9} G_0$ (d).

The most probable absolute displacement z^* in an experimental molecular junction formed between two gold tips is obtained by adding the snap-back distance Δz_{corr} to the relative displacement, namely $z^* = \Delta z^* + \Delta z_{\text{corr}}$. Taking into account $\Delta z_{\text{corr}} = (0.5 \pm 0.1)$ nm, the z^* values are estimated to be 2.2 nm for **1** and 2.0 nm for **2**, which is quite close to the corresponding molecular length, and suggests that both molecules can be fully stretched during the break junction measurement. Thus the conductance of the fully-stretched molecular junction for molecules **1** and **2** are determined to be $10^{-6.7 \pm 0.7} G_0$ (solid red circle in figure 5.2c) and $10^{-4.8 \pm 0.6} G_0$ (solid blue circle in figure 5.2d), with

the conductance ratio of ~ 79 , which is in good agreement with the MRR. To further investigate the accuracy of the MRR and to elucidate the origins of deviations from the rule, I performed DFT-based calculations of the transmission coefficients $T(E)$ of electrons of energy E passing from one electrode to the other, from which the zero temperature electrical conductance is given by Landauer formula: $G = G_0 T(E_F)$ and the room-temperature conductance obtained by integrating $T(E)$ over E , weighted by the derivative of the Fermi function.

Clearly the anthanthrene cores of molecules **1** and **2** do not directly contact the electrodes, but instead make indirect contact via the pyridyl rings and acetylene linkers. Therefore as an initial step, I computed the electrical conductance of the anthanthrene cores of figure 5.3a, when they are in direct contact with the gold electrodes. When the left and right electrodes are connected to atoms $i, i' = 1, 5'$ respectively, this resembles the core of molecule **1**. Similarly the $i, i' = 7, 2'$ connected structure resembles the core of molecule **2**. Figure 5.3b shows the conductance of the anthanthrenes with $1, 5'$ (red curve) and $7, 2'$ (blue curve) connectivities obtained from a *DFT-NEGF* calculation, obtained in the weak coupling limit (when the gold-carbon distance is 2.4 \AA). It is well known that the value of the Fermi energy predicted by DFT (*i.e.* $E_F^0 = 0$ in figure 5.3b) is not necessarily reliable and therefore it is of interest to evaluate the conductance ratio for various values of E_F . From figure 5.3b, I find that in the range $0.2 < E_F < 0.4 \text{ eV}$ the conductance ratio varies between 69 and 88 and for a Fermi energy of $E_F = 0.331 \text{ eV}$ a conductance ratio of 81 is obtained.

For the complete molecules measured experimentally, figure 5.4c and 4d show the logarithm of the G/G_0 at zero and room temperatures, respectively for molecule **1** (red solid line) and **2** (blue solid line) as a function of the Fermi energy E_F . Since *DFT* does not yield the correct H-L gap, spectral adjustment has been employed based on the experimental values of the H-L gaps [47]. As expected, figure 5.4 shows that the value of the conductance ratio depends on the location of the Fermi energy, but whatever value is chosen within the H-L gap, the conductance of **2** is much greater than that of **1**, in agreement with the MRR trend. Indeed for a value of $E_F = -0.33 \text{ eV}$, the conductance of molecule **2** ($10^{-4.98}$) is 81 times higher than that of molecule **1** ($10^{-6.9}$).

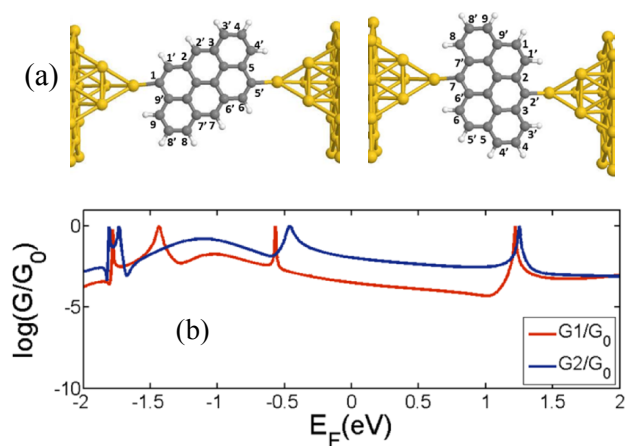


Figure 5.3. (a) The anthanthrene cores connected to gold electrodes. (b) Conductance of the anthanthrene with 1,5' (red curve) and 7,2' (blue curve) cores obtained from DFT-NEGF.

Beyond the molecules investigated above, I have also examined conductance ratios of naphthalene and anthracene cores obtained from the experiments reported in ref [26]. For naphthalene (molecules **4** and **6** in ref [26]) with connectivities 5,1' and 3,5' conductances of 20.8 nS and 4.1 nS were reported, which yields a measured conductance ratio of 5.1. From table 1, the MIs of these molecules are 2 and -1 respectively, yielding a MRR of 4, which is in good agreement with the experimental ratio. For anthracene (molecules **5** and **7** in ref [26]) with connectivities 6,2' and 4,7' conductances of 36.8 nS and 3.6 nS were reported, which yields a measured conductance ratio of 10.2. From the anthracene M-table presented in the SI, the MIs of these molecules are 4 and 1 respectively, yielding a MRR of 16, which also captures the trend of the experimental ratio. In this case slight disagreements may arise, because the conductance values in ref [26] include configurations in which contact is made directly with the core, rather than only through the terminal anchor groups.

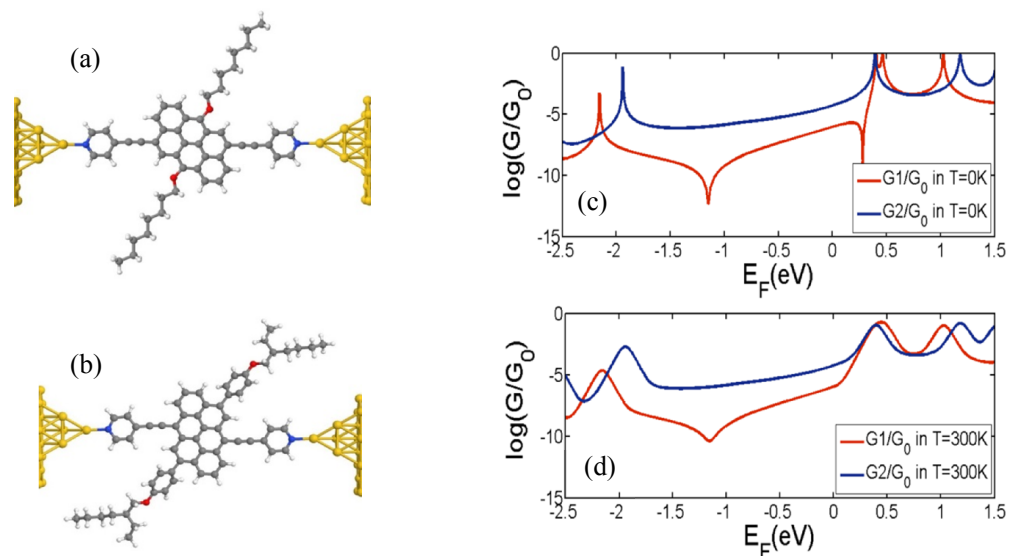


Figure 5.4. (a) and (b) show the structures of **1** and **2** when the electrodes are connected to nitrogen atoms of the pyridyl anchor groups. The conductance of molecules **1** and **2** at (c) zero temperature and (d) room temperature with predicted DFT-gap from Kohn-Sham mean field Hamiltonian and with spectral adjustment based on the experimental values, respectively.

I have identified a new magic ratio rule (MRR), which captures the contribution of connectivity to the conductance ratios of graphene-like cores, when the coupling to the electrodes is weak and the Fermi energy coincides with the centre of the HOMO-LUMO gap. The MRR is simple to implement and exact for a tight-binding, bipartite lattice of identical sites with identical couplings, when the Fermi energy is located at the gap centre and the number of primed sites is equal to the number of unprimed sites. It states that connectivity-driven conductance ratios are simply the squares of two magic integers, whose values depend only on the connectivity to the electrodes. Based on their ‘magic integers’ alone, the MRR predicts that the conductance of **2** is a factor of 81 higher than that of **1**, which is in good agreement with trends obtained from both experiment and *DFT* calculations. Literature values of conductances for naphthalene and anthracene [26] also reveal that the MRR predicts conductance trends for these molecules. This demonstrates that connectivity is a useful starting point for designing single-molecule junctions with desirable electrical properties. As an ex-

ample of such design considerations, for the purpose of connecting molecules to source-drain electrodes, a high conductance is desirable. On the other hand for the purpose of connecting to an electrostatic gate, a low conductance is needed to avoid leakage currents. This study suggests that both features can be obtained using the same molecule provided connectivities are selected with high and low MIs for source-drain and gate electrodes, respectively. As a second example, this results suggest that the MRR may be a useful guide for the design of future molecular-scale information processors, because with appropriate connectivities, graphene-like molecules provide direct information about the inverse (M) of a matrix (C).

DFT calculation: The optimized geometry and ground state Hamiltonian and overlap matrix elements of each structure was self-consistently obtained using the *SIESTA* [48] implementation of density functional theory (*DFT*). *SIESTA* employs norm-conserving pseudo-potentials to account for the core electrons and linear combinations of atomic orbitals to construct the valence states. The generalized gradient approximation (*GGA*) of the exchange and correlation functional is used with the Perdew-Burke-Ernzerhof parameterization (*PBE*) [49] a double- ζ polarized (*DZP*) basis set, a real-space grid defined with an equivalent energy cut-off of $250 Ry$. The geometry optimization for each structure is performed to the forces smaller than $10 meV/\text{\AA}$.

Transport calculations: The mean-field Hamiltonian obtained from the converged *DFT* calculation or a tight-binding Hamiltonian (using single orbital energy site per atom with Hückel parameterisation) was combined with our implementation of the non-equilibrium Green's function method, *GOLLUM* [50], to calculate the phase-coherent, elastic scattering properties of the each system consisting of left gold (source) and right gold (drain) leads and the scattering region (molecule **1** or **2**). The transmission coefficient $T(E)$ for electrons of energy E (passing from the source to the drain) is calculated via the relation: $T(E) = Trace(\Gamma_R(E)G^R(E)\Gamma_L(E)G^{R\dagger}(E))$. In this expression, $\Gamma_{L,R}(E) = i(\Sigma_{L,R}(E) - \Sigma_{L,R}^\dagger(E))$ describe the level broadening due to the coupling between left (L) and right

(R) electrodes and the central scattering region, $\Sigma_{L,R}(E)$ are the retarded self-energies associated with this coupling and $G^R = (ES - H - \Sigma_L - \Sigma_R)^{-1}$ is the retarded Green's function, where H is the Hamiltonian and S is overlap matrix. Using obtained transmission coefficient $T(E)$, the conductance could be calculated by Landauer formula ($G = G_0 \int dE T(E)(-\partial f/\partial E)$) where $G_0 = 2e^2/h$ is conductance quantum.

References

- [1] F. Chen and N. Tao, "Electron transport in single molecules: from benzene to graphene," *Accounts of chemical research*, vol. 42, pp. 429-438, 2009.
- [2] W. Pisula, X. Feng, and K. Müllen, "Charge-Carrier Transporting Graphene-Type Molecules†," *Chemistry of Materials*, vol. 23, pp. 554-567, 2010.
- [3] R. L. Carroll and C. B. Gorman, "The genesis of molecular electronics," *Angewandte Chemie International Edition*, vol. 41, pp. 4378-4400, 2002.
- [4] J. Wu, W. Pisula, and K. Müllen, "Graphenes as potential material for electronics," *Chemical Reviews*, vol. 107, pp. 718-747, 2007.
- [5] A. Coskun, J. M. Spruell, G. Barin, W. R. Dichtel, A. H. Flood, Y. Y. Botros, *et al.*, "High hopes: can molecular electronics realise its potential?," *Chemical Society Reviews*, vol. 41, pp. 4827-4859, 2012.
- [6] L. Zhang, A. Fonari, Y. Liu, A.-L. M. Hoyt, H. Lee, D. Granger, *et al.*, "Bistetracene: An Air Stable, High Mobility Organic Semiconductor with Extended Conjugation," *Journal of the American Chemical Society*, vol. 136, pp. 9248-9251, 2014.

- [7] J. Cai, P. Ruffieux, R. Jaafar, M. Bieri, T. Braun, S. Blankenburg, *et al.*, "Atomically precise bottom-up fabrication of graphene nanoribbons," *Nature*, vol. 466, pp. 470-473, 2010.
- [8] P. Ruffieux, J. Cai, N. C. Plumb, L. Patthey, D. Prezzi, A. Ferretti, *et al.*, "Electronic structure of atomically precise graphene nanoribbons," *Acs Nano*, vol. 6, pp. 6930-6935, 2012.
- [9] J. Cai, C. A. Pignedoli, L. Talirz, P. Ruffieux, H. Söde, L. Liang, *et al.*, "Graphene nanoribbon heterojunctions," *Nature nanotechnology*, vol. 9, pp. 896-900, 2014.
- [10] G. Sedghi, V. M. García-Suárez, L. J. Esdaile, H. L. Anderson, C. J. Lambert, S. Martín, *et al.*, "Long-range electron tunnelling in oligo-porphyrin molecular wires," *Nature nanotechnology*, vol. 6, pp. 517-523, 2011.
- [11] X. Zhao, C. Huang, M. Gulcur, A. S. Batsanov, M. Baghernejad, W. Hong, *et al.*, "Oligo(aryleneethynylene)s with Terminal Pyridyl Groups: Synthesis and Length Dependence of the Tunneling-to-Hopping Transition of Single-Molecule Conductances," *Chemistry of Materials*, vol. 25, pp. 4340-4347, 2013.
- [12] M. Magoga and C. Joachim, "Conductance of molecular wires connected or bonded in parallel," *Physical Review B*, vol. 59, p. 16011, 1999.
- [13] T. Papadopoulos, I. Grace, and C. Lambert, "Control of electron transport through Fano resonances in molecular wires," *Physical Review B*, vol. 74, p. 193306, 2006.
- [14] C. Wang, M. R. Bryce, J. Gigon, G. J. Ashwell, I. Grace, and C. J. Lambert, "Synthesis and properties of functionalized 4 nm scale molecular wires with thiolated termini for self-assembly onto metal surfaces," *The Journal of organic chemistry*, vol. 73, pp. 4810-4818, 2008.
- [15] S.-H. Ke, W. Yang, and H. U. Baranger, "Quantum-interference-controlled molecular electronics," *Nano letters*, vol. 8, pp. 3257-3261, 2008.

- [16] C. Finch, V. Garcia-Suarez, and C. Lambert, "Giant thermopower and figure of merit in single-molecule devices," *Physical review b*, vol. 79, p. 033405, 2009.
- [17] J. P. Bergfield, M. A. Solis, and C. A. Stafford, "Giant thermoelectric effect from transmission supernodes," *ACS nano*, vol. 4, pp. 5314-5320, 2010.
- [18] A. B. Ricks, G. C. Solomon, M. T. Colvin, A. M. Scott, K. Chen, M. A. Ratner, *et al.*, "Controlling Electron Transfer in Donor– Bridge– Acceptor Molecules Using Cross-Conjugated Bridges," *Journal of the American Chemical Society*, vol. 132, pp. 15427-15434, 2010.
- [19] T. Markussen, J. Schiötz, and K. S. Thygesen, "Electrochemical control of quantum interference in anthraquinone-based molecular switches," *The Journal of chemical physics*, vol. 132, p. 224104, 2010.
- [20] G. C. Solomon, J. P. Bergfield, C. A. Stafford, and M. A. Ratner, "When “small” terms matter: Coupled interference features in the transport properties of cross-conjugated molecules," *Beilstein journal of nanotechnology*, vol. 2, pp. 862-871, 2011.
- [21] H. Sadeghi, J. A. Mol, C. S. Lau, G. A. D. Briggs, J. Warner, and C. J. Lambert, "Conductance enlargement in picoscale electroburnt graphene nanojunctions," *Proceedings of the National Academy of Sciences*, vol. 112, pp. 2658–2663, 2015.
- [22] W. Hong, H. Valkenier, G. Mészáros, D. Z. Manrique, A. Mishchenko, A. Putz, *et al.*, "An MCBJ case study: The influence of π -conjugation on the single-molecule conductance at a solid/liquid interface," *Beilstein journal of nanotechnology*, vol. 2, pp. 699-713, 2011.
- [23] H. Vazquez, R. Skouta, S. Schneebeli, M. Kamenetska, R. Breslow, L. Venkataraman, *et al.*, "Probing the conductance superposition law in single-molecule circuits with parallel paths," *Nature nanotechnology*, vol. 7, pp. 663-667, 2012.

- [24] S. Ballmann, R. Härtle, P. B. Coto, M. Elbing, M. Mayor, M. R. Bryce, *et al.*, "Experimental Evidence for Quantum Interference and Vibrationally Induced Decoherence in Single-Molecule Junctions," *Physical review letters*, vol. 109, p. 056801, 2012.
- [25] S. V. Aradhya, J. S. Meisner, M. Krikorian, S. Ahn, R. Parameswaran, M. L. Steigerwald, *et al.*, "Dissecting contact mechanics from quantum interference in single-molecule junctions of stilbene derivatives," *Nano letters*, vol. 12, pp. 1643-1647, 2012.
- [26] V. Kaliginedi, P. Moreno-García, H. Valkenier, W. Hong, V. M. García-Suárez, P. Buitter, *et al.*, "Correlations between molecular structure and single-junction conductance: A case study with oligo (phenylene-ethynylene)-type wires," *Journal of the American Chemical Society*, vol. 134, pp. 5262-5275, 2012.
- [27] S. V. Aradhya and L. Venkataraman, "Single-molecule junctions beyond electronic transport," *Nature nanotechnology*, vol. 8, pp. 399-410, 2013.
- [28] C. R. Arroyo, S. Tarkuc, R. Frisenda, J. S. Seldenthuis, C. H. Woerde, R. Eelkema, *et al.*, "Signatures of quantum interference effects on charge transport through a single benzene ring," *Angewandte Chemie*, vol. 125, pp. 3234-3237, 2013.
- [29] C. M. Guédon, H. Valkenier, T. Markussen, K. S. Thygesen, J. C. Hummelen, and S. J. van der Molen, "Observation of quantum interference in molecular charge transport," *Nature nanotechnology*, vol. 7, pp. 305-309, 2012.
- [30] F. Prins, A. Barreiro, J. W. Ruitenber, J. S. Seldenthuis, N. Aliaga-Alcalde, L. M. Vandersypen, *et al.*, "Room-temperature gating of molecular junctions using few-layer graphene nanogap electrodes," *Nano letters*, vol. 11, pp. 4607-4611, 2011.
- [31] G. J. Ashwell, B. Urasinska, C. Wang, M. R. Bryce, I. Grace, and C. J. Lambert, "Single-

molecule electrical studies on a 7 nm long molecular wire," *Chemical communications*, pp. 4706-4708, 2006.

[32] C. Lambert, "Basic concepts of quantum interference and electron transport in single-molecule electronics," *Chemical Society Reviews*, pp. 875-888, 2015.

[33] K. Yoshizawa, T. Tada, and A. Staykov, "Orbital views of the electron transport in molecular devices," *Journal of the American Chemical Society*, vol. 130, pp. 9406-9413, 2008.

[34] K. Yoshizawa, "An orbital rule for electron transport in molecules," *Accounts of chemical research*, vol. 45, pp. 1612-1621, 2012.

[35] P. Fowler, B. Pickup, T. Todorova, and W. Myrvold, "Conduction in graphenes," *The Journal of chemical physics*, vol. 131, p. 244110, 2009.

[36] P. Fowler, B. Pickup, T. Todorova, and W. Myrvold, "A selection rule for molecular conduction," *The Journal of chemical physics*, vol. 131, p. 044104, 2009.

[37] D. Mayou, Y. Zhou, and M. Ernzerhof, "The Zero-Voltage Conductance of Nanographenes: Simple Rules and Quantitative Estimates," *The Journal of Physical Chemistry C*, vol. 117, pp. 7870-7884, 2013.

[38] T. Markussen, R. Stadler, and K. S. Thygesen, "The Relation between Structure and Quantum Interference in Single Molecule Junctions," *Nano Letters*, vol. 10, pp. 4260-4265, 2010.

[39] K. N. Winzenberg, P. Kemppinen, G. Fanchini, M. Bown, G. E. Collis, C. M. Forsyth, *et al.*, "Dibenzo [b, def] chrysene derivatives: solution-processable small molecules that deliver high power-conversion efficiencies in bulk heterojunction solar cells," *Chemistry of Materials*, vol. 21, pp. 5701-5703, 2009.

- [40] K. B. Burke, Y. Shu, P. Kemppinen, B. Singh, M. Bown, I. I. Liaw, *et al.*, "Single crystal X-ray, AFM, NEXAFS, and OFET studies on angular polycyclic aromatic silyl-capped 7, 14-Bis(ethynyl) dibenzo [b, def] chrysenes," *Crystal Growth & Design*, vol. 12, pp. 725-731, 2012.
- [41] R. Cardia, G. Mallocci, A. Mattoni, and G. Cappellini, "Effects of TIPS-Functionalization and Perhalogenation on the Electronic, Optical, and Transport Properties of Angular and Compact Dibenzochrysene," *The Journal of Physical Chemistry A*, vol. 118, pp. 5170-5177, 2014.
- [42] J.-B. Giguère, J. Boismenu-Lavoie, and J.-F. Morin, "Cruciform Alkynylated Anthanthrene Derivatives: A Structure–Properties Relationship Case Study," *The Journal of organic chemistry*, vol. 79, pp. 2404-2418, 2014.
- [43] A. Maliakal, K. Raghavachari, H. Katz, E. Chandross, and T. Siegrist, "Photochemical stability of pentacene and a substituted pentacene in solution and in thin films," *Chemistry of materials*, vol. 16, pp. 4980-4986, 2004.
- [44] W. Fudickar and T. Linker, "Why triple bonds protect acenes from oxidation and decomposition," *Journal of the American Chemical Society*, vol. 134, pp. 15071-15082, 2012.
- [45] W. Hong, D. Z. Manrique, P. Moreno-Garcia, M. Gulcur, A. Mishchenko, C. J. Lambert, *et al.*, "Single molecular conductance of tolanes: experimental and theoretical study on the junction evolution dependent on the anchoring group," *Journal of the American Chemical Society*, vol. 134, pp. 2292-2304, 2012.
- [46] W. Hong, H. Li, S.-X. Liu, Y. Fu, J. Li, V. Kaliginedi, *et al.*, "Trimethylsilyl-Terminated Oligo(phenylene ethynylene)s: An Approach to Single-Molecule Junctions with Covalent Au–C σ -Bonds," *Journal of the American Chemical Society*, vol. 134, pp. 19425-19431, 2012.
- [47] V. M. García-Suárez and C. J. Lambert, "First-principles scheme for spectral adjustment

in nanoscale transport," *New Journal of Physics*, vol. 13, p. 053026, 2011.

[48] J. M. Soler, E. Artacho, J. D. Gale, A. García, J. Junquera, P. Ordejón, *et al.*, "The SIESTA method for ab initio order-N materials simulation," *Journal of Physics: Condensed Matter*, vol. 14, p. 2745, 2002.

[49] J. P. Perdew, K. Burke, and M. Ernzerhof, "Generalized gradient approximation made simple," *Physical review letters*, vol. 77, p. 3865, 1996.

[50] J. Ferrer, C. Lambert, V. García-Suárez, D. Z. Manrique, D. Visontai, L. Oroszlany, *et al.*, "GOLLUM: a next-generation simulation tool for electron, thermal and spin transport," *New Journal of Physics*, vol. 16, p. 093029, 2014.

Chapter 6

Molecular thermoelectric devices

Understanding phonon transport at a molecular scale is fundamental to the development of high-performance thermoelectric materials for the conversion of waste heat into electricity. We have studied phonon and electron transport in alkane and oligoynes chains of various lengths and find that due to the more rigid nature of the latter, the phonon thermal conductances of oligoynes are counter intuitively lower than that of the corresponding alkanes. The thermal conductance of oligoynes decreases monotonically with increasing length, whereas the thermal conductance of alkanes initially increases with length and then decreases. This difference in behaviour arises from phonon filtering by the gold electrodes and disappears when higher-Debye-frequency electrodes are used. Consequently a molecule that better transmits higher-frequency phonon modes, combined with a low-Debye-frequency electrode that filters high-energy phonons is a viable strategy for suppressing phonon transmission through the molecular junctions. The low thermal conductance of oligoynes, combined with their higher thermopower and higher electrical conductance lead to yield a maximum thermoelectric figure of merit of $ZT = 1.4$, which is several orders of magnitude higher than for alkanes.

The results presented in this chapter were published in: Sadeghi, et al. Oligoynes molecular junctions for efficient room temperature thermoelectric power generation, 2015, Nano letters 15 (11), 7467-7472

For many years, the attraction of the single-molecule electronics [1-6] has stemmed from their potential for sub-10nm electronic switches and rectifiers, and from their provision of sensitive platforms for single-molecule sensing. In the recent years, their potential for removing heat from nanoelectronic devices (thermal management) and thermoelectrically converting waste heat into electricity [7-10] has also been recognised. The efficiency of a thermoelectric device for power generation is characterised by the dimensionless figure of merit $ZT = GS^2T/\kappa$, where G is the electrical conductance, S is the thermopower (Seebeck coefficient), T is temperature and κ is the thermal conductance [11-14]. Therefore low- κ materials are needed for efficient conversion of heat into electricity, whereas materials with high κ are needed for thermal management. Inorganic materials for thermoelectricity have been extensively studied and have delivered ZT values as high as 2.2 at temperatures over 900K [15]. However this level of efficiency does not meet the requirements of current energy demands [16] and furthermore, the materials are difficult to process and have limited global supply. Organic thermoelectric materials may be an attractive alternative, but at present the best organic thermoelectric material with a ZT of 0.6 in room temperature [17, 18] is still not competitive with inorganics. In an effort to overcome these limitations, single organic molecules and self-assembled monolayers have attracted recent scientific interest, both for their potential as room temperature thermoelectric materials and thermal management [19, 20].

Strategies for reducing the denominator (ie κ) of ZT in single-molecule junctions are fundamentally different from inorganic bulk materials. In the latter, phonon transport can be reduced by nanostructuring [21, 22], whereas molecular junctions are naturally nanostructured and additional strategies based on molecular phonon conversion [23] become possible, including the reduction of thermal conductance due to weak overlap between the continuum of vibrational states in the electrodes and discrete vibrational states of the molecules or the weak interaction between different part of the molecules, as in π - π stacked structures [24]. On the other hand, strategies for increasing the numerator of ZT (ie the power factor) focus on tuning electron transport properties, which are determined by the energetic position of the electrode Fermi energy relative to transport resonances through the frontier orbitals of the molecule. If $T_{ei}(E)$ is

the transmission coefficient of electrons of energy E passing from one electrode to the other through a molecule, then the thermopower S is approximately proportional to the slope of the $\ln T_{el}(E)$, evaluated at the Fermi energy E_F , whereas the electrical conductance is proportional to $T_{el}(E_F)$. Therefore if the Fermi energy lies in a region of high slope, close to a transmission resonance of the frontier orbitals and provided the (HOMO-LUMO) gap between the resonances is greater than $\sim 4k_B T$ (ie ~ 100 meV at room temperature), then both G and S can be enhanced [11]. In the literature, there are many experiments addressing electronic properties of single molecules, but far fewer addressing single-molecule phonon transport, partly because it is extremely difficult to measure the thermal conductance of a single molecule. This difficulty is partly circumvented by scanning thermal microscope measurements of a few thousands of molecules in parallel, such as a recent experimental study of the length-dependent thermal conductance of alkanes by the *IBM* group [25], which revealed a surprising initial increase in thermal conductance with length for short alkanes.

In this chapter, I present a comparative theoretical study of the length dependent thermal properties of the alkanes and oligoynes, which elucidates the origin of this initial increase and demonstrate that oligoynes offer superior performance for future efficient thermoelectric power generation. Since the thermopower and electrical conductance of oligoynes and alkanes are generally understood [26-28], my main focus in this chapter is to calculate the thermal conductance of these materials, which contains contributions from both electrons and phonons. The main unexpected result from my study is that thermal conductances of oligoynes are lower than alkanes of the same length, which is counter intuitive, because alkanes are more floppy than oligoynes. Moreover, the thermopower and electrical conductance is higher in oligoynes. The resulting combination of low thermal conductance, high thermopower and high electrical conductance lead to a high value of ZT and make oligoynes attractive for future thermoelectric devices.

Recently length-dependent thermopowers of alkane, alkene, and oligoyne chains with four different anchor groups (thiol, isocyanide, and amine end groups and direct coupling) were theoretically studied for the chains with the length 2, 4, 6 and 8 carbon atoms [26-28]. It was

shown that the sign and magnitude of the thermopower, and the conductance-length attenuation factor (β) are strongly affected by the anchor groups. For example, in oligoynes the thermopower was found to be positive with a direct C-Au bond or thiol anchor and negative with a NC end group [29]. Furthermore, while the conductance G decays exponentially as $\exp(-\beta L)$ with increasing molecular length L , the thermopower shows a linear length dependence [30]. The crucial point is that higher thermopower is predicted for oligoynes compared with alkanes for all lengths [29], a fact that is in good agreement with my calculations below. Although the thermal conductance of self-assembled monolayers of alkanes sandwiched between gold and GaAs was shown to be length independent and as high as $27 \text{ MW m}^{-2}\text{K}^{-1}$ [23], recent experiment on alkanes sandwiched between gold and SiO_2 shows length dependencies [25] in agreement with my study in this chapter.

As shown in figures 6.1a and 6.2a, the alkanes and oligoynes of interest in this study are of lengths of 2, 4, 8 and 16 carbon atoms ($N = 1, 2, 4, \text{ and } 8$) and are connected to two gold electrodes through dihydrobenzo[b]thiophene (BT) anchor groups. To study the thermal properties of the alkanes (figure 6.1a) and oligoynes (figure 6.2a), I use density functional theory (*DFT*) to calculate their electronic and vibrational properties within the junction. I first carry out geometry optimization of each molecule placed between two gold electrodes using *DFT* [31, 32] to find the ground state optimum positions of the atoms (q) relative to each other's and electronic mean field Hamiltonian of the system including electrodes and molecule (see methods below). The mean field Hamiltonian is combined with our Green's function scattering method [33] to calculate the electron transmission coefficient $T_{el}(E)$, from which the electrical conductance $G = G_0 \int dE T_{el}(E) (-\partial f / \partial E)$ is obtained, where G_0 is the conductance quantum and $f(E)$ is the Fermi function. Figures 6.1b and 6.2b show $T_{el}(E)$ for alkanes with $N = 1, 2, 4$ and 8 pairs of carbon atoms and oligoynes with $N = 1, 2$ and 4 pairs of carbon atoms, respectively. In agreement with previous experimental and theoretical studies [26, 34-37], when evaluated at the *DFT*-computed Fermi energy (E_F^{DFT}) the transmission coefficients decrease with the length for both alkanes and oligoynes. However, the conductances of the oligoynes are higher than those of the alkanes for equivalent lengths, due to the broken π -conjugation in the alkanes.

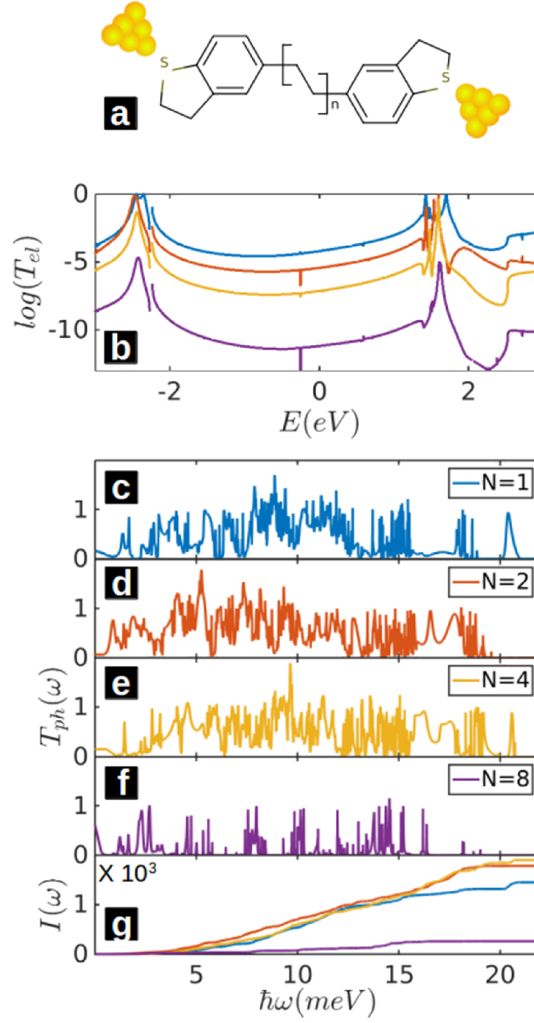


Figure 6.1. Molecular structure and transport properties of alkanes with the length of $N = 1, 2, 4, 8$ between two gold electrodes. (a) Schematic of the junction, (b) electronic and (c-f) phononic transmission coefficients. (g) The integrated phonon transmission $I(\omega)$. All molecules are terminated with BT (ie dihydrobenzo[*b*]thiophene) anchor groups.

To calculate the vibrational modes of each structure, I use the harmonic approximation method to construct the dynamical matrix D . Each atom is displaced from its equilibrium position by $\delta q'$ and $-\delta q'$ in x, y and z directions and the forces on all atoms calculated in each case. For $3n$ degrees of freedom ($n =$ number of atoms), the $3n \times 3n$ dynamical matrix $D_{ij} = (F_i^q(\delta q'_j) - F_j^q(-\delta q'_i))/2M_{ij}\delta q'_j$ is constructed, where F and M are the force and mass matrices (see methods below). For an isolated molecule, the square root of the eigenvalues of D determines the frequencies ω associated with the vibrational modes of the molecule in the junction. For a molecule within a junction, the dynamical matrix describes an open system composed of the

molecule and two semi-infinite electrodes and is used to calculate the phononic transmission coefficient $T_{ph}(\omega)$ for the phonons with energy $\hbar\omega$ passing through the molecule from the right to the left electrode. Figures 6.1c-f and 6.2c-e show $T_{ph}(\omega)$ for alkanes and oligoynes respectively of different lengths. To elucidate the different areas under these curves, figure 6.1g and 6.2f show their integrated transmission coefficients $I(\omega) = \int_0^\omega T_{ph}(\omega)d\omega$. At high frequencies, the transmission is limited by the number of open phonon channels in the gold electrodes, which falls to zero above the gold (111) Debye frequency of 21 *meV*. This shows that a molecule that better transmits higher modes, combined with a low-Debye-frequency electrode that filters high energy phonons could be a viable strategy to suppress phonon transmission through the junction.

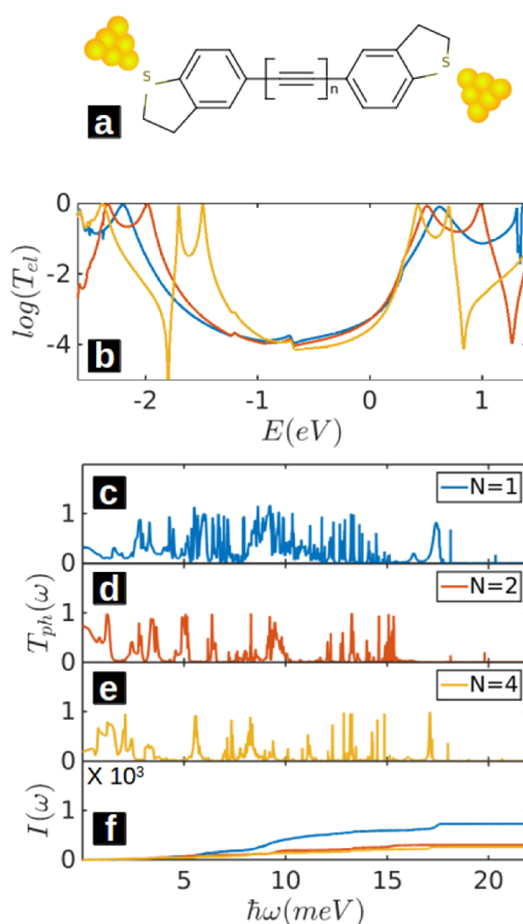


Figure 6.2. Molecular structure and transport properties of oligoynes with the length of $N = 1, 2, 4$ between two gold electrodes. (a) Schematic of the junction, (b) electronic and (c-e) phononic transmission coefficients. (f) The integrated phonon transmission $I(\omega)$. All molecules are terminated with BT (ie dihydrobenzo[b]thiophene) anchor groups.

The thermal conductance of the junction ($\kappa = \kappa_{ph} + \kappa_{el}$) is obtained by summing the contributions from both electrons (κ_{el}) and phonons (κ_{ph}). The electronic (phononic) thermal conductances are calculated from the electronic (phononic) transmission coefficients shown in figures 6.1b and 6.2b (figures. 6.1c-f and 6.2c-e) as described in the methods section below. Figure 6.3a,b shows the resulting electronic thermal conductance κ_{el} and figure 6.3c,d the phononic thermal conductance κ_{ph} for alkanes and oligoynes, respectively. In general, the thermal conductance is dominated by phonons. For example the phononic thermal conductance κ_{ph} of the $N = 1$ oligoyne (alkane) is more than 30 (700) times bigger than electronic thermal conductance κ_{el} at room temperature. Therefore for these molecules κ_{el} is negligible. In addition, the thermal conductances of the alkanes are higher than those of the oligoynes, which suggests that alkanes are potentially useful for thermal management, but less useful for thermoelectricity.

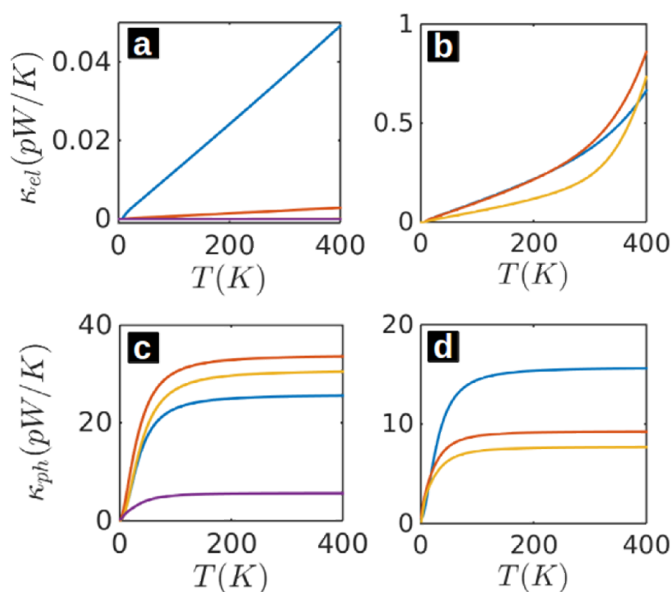


Figure 6.3. Electronic and phononic thermal conductance of alkanes and oligoynes. (a,b) show the electronic thermal conductance of alkanes and oligoynes respectively. (c,d) show the phononic thermal conductance of alkanes and oligoynes respectively. Results are shown for molecules of different lengths. For colour coding see figure 6.1.

In both types of junctions, the thermal conductance increases with temperature up to about 170K, (ie the Debye temperature of the gold electrodes) and then remains constant (fig. 6.3c,d). For oligoynes, at room temperature, κ is equal to 15.6, 9.2 and 7.7 pW/K for $N = 1, 2, 4$

respectively. It is apparent that the thermal conductance of the oligoynes molecules decreases monotonically with length. In contrast, for alkanes, thermal conductance initially increases with length and then decreases. At room temperature, the κ of alkanes are equal to 25.4, 33.4, 30.3 and 5.6 pW/K for $N = 1, 2, 4$ and 8 respectively, revealing that the $N = 2$ alkane has the highest thermal conductance. This initial increase in thermal conductance with length followed by a decrease has been observed experimentally [25] and predicted theoretically [38] in previous studies, although its origin remains unexplored. To account for this behaviour it is useful to understand why it does not occur for the more rigid oligoynes.

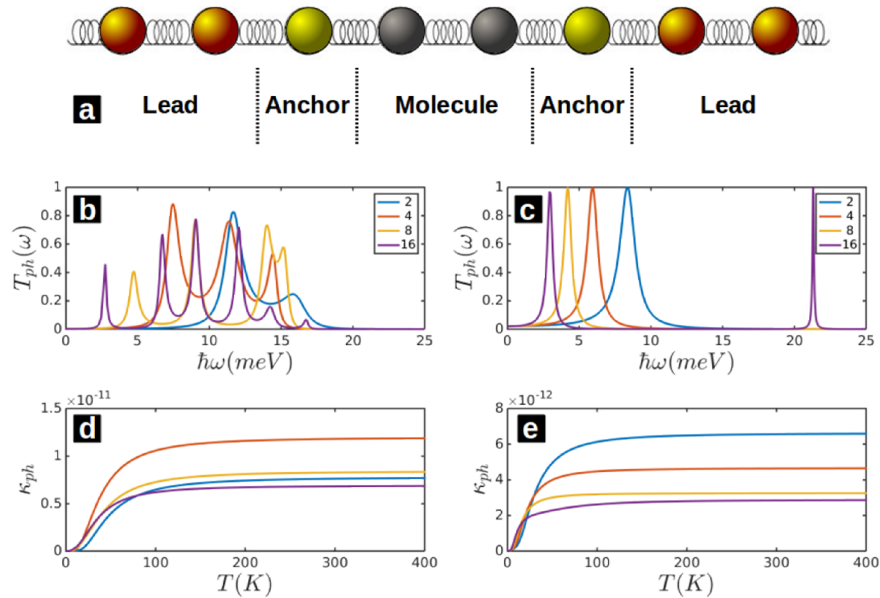


Figure 6.4. A calculation of the phonon transmission coefficient and thermal conductance of a 1D chain of atoms (with a single degree of freedom) connected by harmonic springs. (a) schematic of junction structure, (b,c) the phonon transmission coefficient of chains of varying length with (b) weak and (c) stronger springs between the atoms and with a fixed coupling between the anchor atom and lead. (d, e) the corresponding thermal conductances (d) for (b) and (e) for (c). In both cases, the resonance widths decrease with increasing length. For the more floppy molecule (b) increasing from $N=2$ to $N=4$ causes more resonances enter the non-filtered low-energy window, leading to an increase in thermal conductance.

First I note that the phonon thermal conductance of oligoynes is lower than that of alkanes, because due to their rigidity, the phonon level spacing between the oligoynes modes is bigger

than that of the alkanes (figure 6.1c-f and figure 6.2c-e). Consequently a greater fraction of the oligoyne modes lie above the Debye frequency of the gold electrodes and are therefore filtered by the gold. In the less-rigid alkanes, which possess more low-frequency modes (figure 6.1c-f), this filtering effect is less pronounced. As the length of the chain is increased, all modes move to lower frequencies (which tends to increase the thermal conductance) and the widths of transmission resonances decrease (which tends to decrease the thermal conductance), because the imaginary part of the self-energy is proportional to the inverse length of the molecules [39].

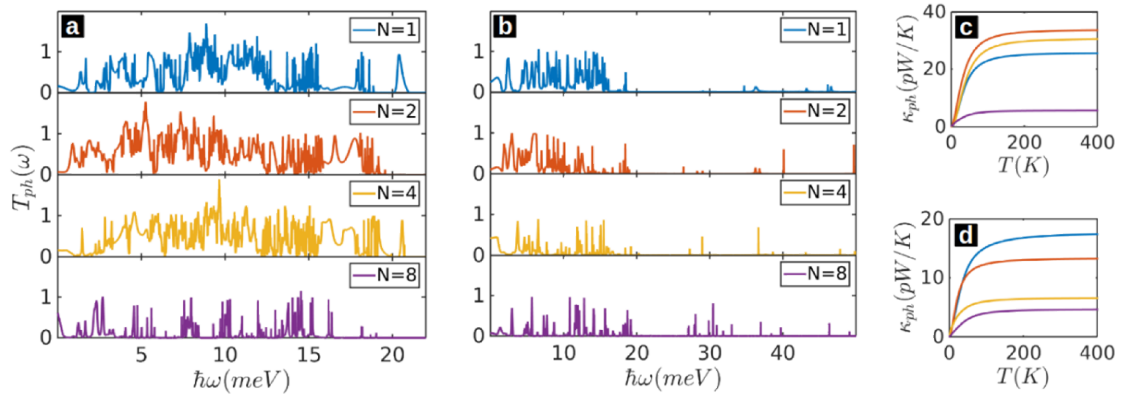
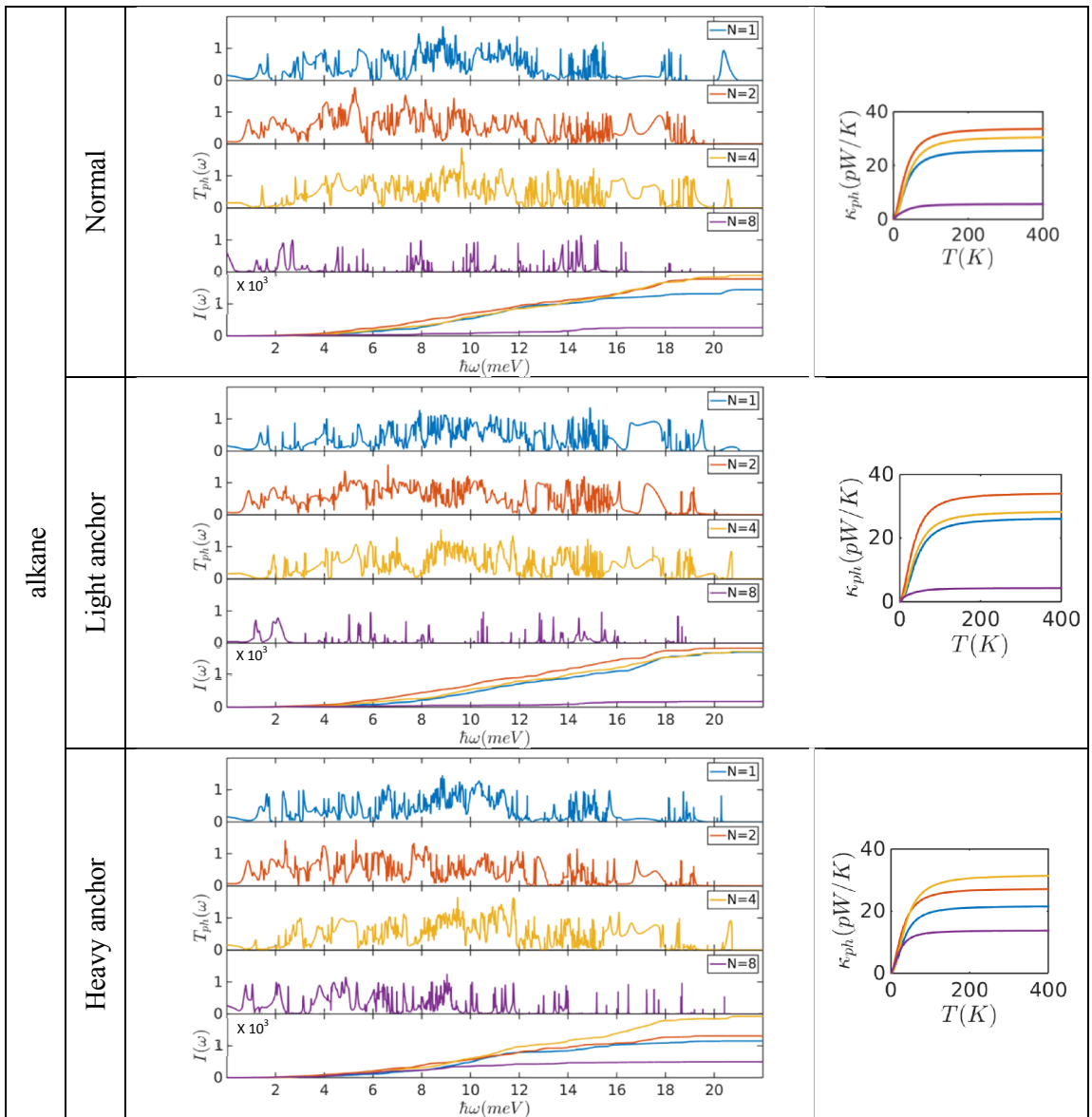


Figure 6.5. Alkane chains connected to two gold lead with (a, c) normal gold mass and (b, d) reduced gold mass. (a, b) show the phonon transmission coefficient and (c, d) phonon thermal conductance. At high frequencies, the transmission is limited by the number of open phonon channels in the gold electrodes, which falls to zero above the gold Debye frequency. This shows that a molecule that better transmits higher modes, combined with a low-Debye-frequency electrode that filters high energy phonons could be a viable strategy to suppress phonon transmission through the junction.

This unconventional behaviour is also illustrated by a simple “tight-binding” model (see fig. 6.4) with one degree of freedom per atom. In oligoyne, relatively-high frequency of the modes means that resonance narrowing dominates at all lengths. In the case of alkanes, a significant number of the $N=1$ modes are filtered by the gold and upon increasing to $N=2$, these modes move to lower frequencies and are no longer filtered, leading to the unexpected increase in thermal conductance. At longer lengths decrease in resonance widths with increasing length dominates and κ_{ph} decreases with length. To demonstrate that this counter-intuitive effect disappears when phonon filtering is removed, I have examined the effect of artificially reducing

the mass of the electrodes gold atoms. This is achieved by simply multiplying the mass matrix M_{ij} by a scale factor in the *DFT*-constructed dynamical matrix, which increases the Debye frequency of the electrodes. As shown in figure 6.5, the resulting thermal conductance of the alkanes decreases monotonically with length. This leads us to predict that conventional length dependence for thermal conductance of alkanes will be observed if higher-Debye-frequency electrodes such as graphene [5] are used.



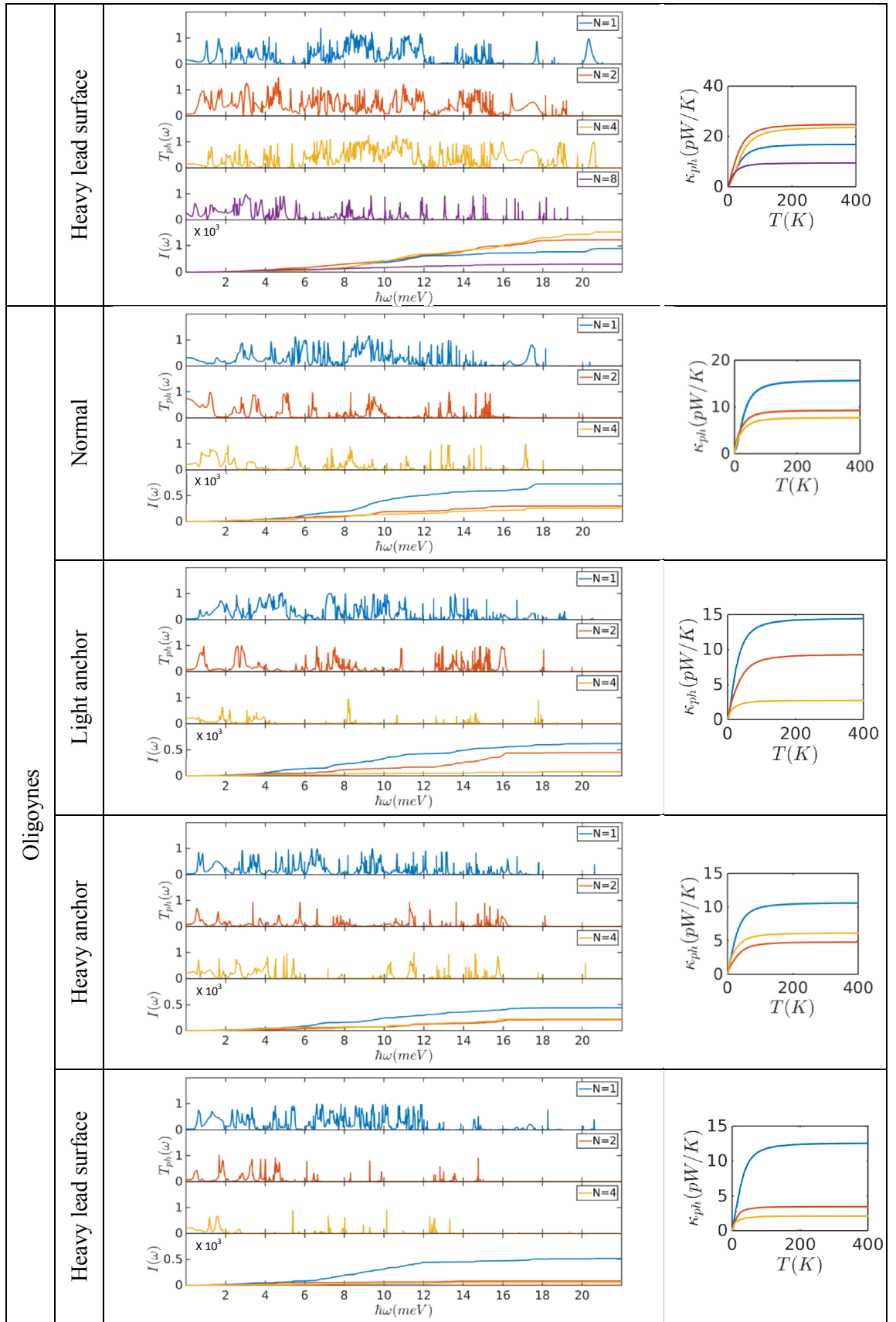


Figure 6.6. Thermal conductance of the alkanes and oligynes with artificially-scaled masses of atoms on the BT anchors or the electrode surface.

In addition, to demonstrate the effect of the junction properties e.g. different anchor and electrode surface on the phononic thermal conductance, I have examined the effect of artificially changing the mass of the atoms in the BT anchors by a factor of 0.5 or 2 and of the atoms on the surface of the electrodes by a factor of 2 as shown in figure 6.6. Although thermal conductance is affected by changes in the anchor or electrodes surface, in all cases, the alkanes show an initial rise in κ_{ph} upon increasing the length from $N=1$ to $N=2$ and the thermal conductance of alkanes is higher than that of the corresponding oligoynes.

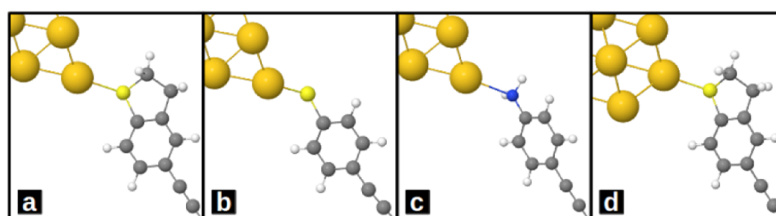


Figure 6.7. Junction configurations. Three different anchors (a) dihydrobenzo[b]thiophene (*BT*), (b) thiol (*SH*) and (c) amine (*NH₂*) anchors connected to the similar electrode and (d) *BT* anchor connected to the electrode with different surface structure (pyramid tip).

Furthermore, to demonstrate that this trend is resilient and independent of the anchor and electrode surface configuration, using *DFT*-constructed dynamical matrix, I have calculated the phononic thermal conductance of the alkane and oligoynes with the length of $N=4$ with two other anchors (amine and thiol anchors) and a different configuration of the electrode tip as shown in figure 6.7. The corresponding electronic and phononic transmission coefficients are shown in figure 6.8 and 6.9 for alkanes and oligoynes, respectively. Although the amplitude of the thermal conductance varies with anchor and tip configuration (figure 6.10), the thermal conductance of oligoynes is still lower than that of the corresponding alkanes.

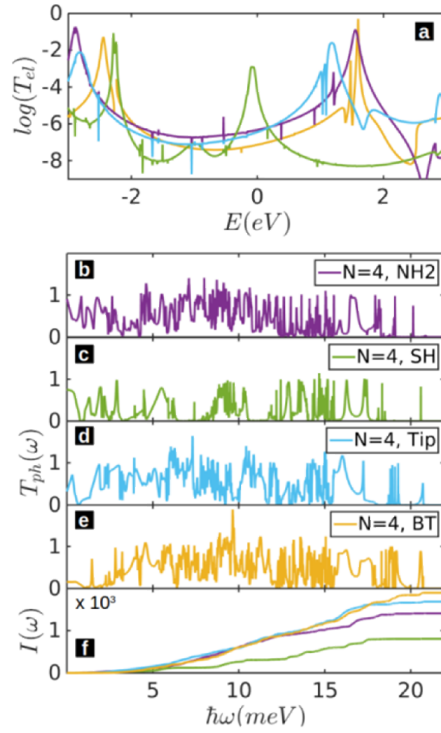


Figure 6.8. Electronic and phononic properties of alkane $N=4$ junctions shown in figure 6.7. (a) electronic, (b-e) phononic transmission coefficients, (f) cumulative phononic transmission coefficient $I(\omega)$.

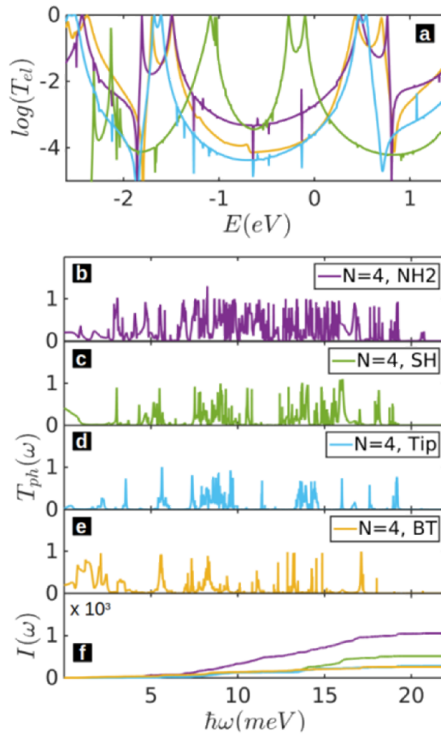


Figure 6.9. Electronic and phononic properties of oligoyne $N=4$ junctions shown in figure 6.7. (a) electronic, (b-e) phononic transmission coefficients, (f) cumulative phononic transmission coefficient $I(\omega)$.

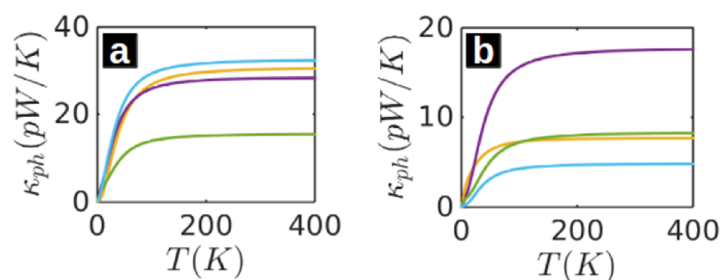


Figure 6.10. Phononic thermal conductance of the alkanes and oligoynes with different junction structure (shown in figure 6.7) versus different temperatures. (a) alkanes and (b) oligoynes. Colour map is as figures 6.8 and 6.9.

To compare the potential of these two families of molecules for thermoelectricity, I calculated the electrical conductance and thermopower of the alkanes and oligoynes as described in the methods section below. Since the thermopower depends on the Fermi energy of the leads and could be tuned by electrostatic or electrochemical gating or doping, I computed the electrical conductance, thermopower and total thermoelectric figure of merit at different Fermi energies. Figures 6.11a,b show the thermopower of alkanes and oligoynes respectively with different lengths at room temperature and for different Fermi energies. In general the thermopower is an order of magnitude higher for oligoynes. This is because for oligoynes, the Fermi energy lies in the tail of the HOMO or LUMO resonance [26] depending on the anchor groups (see eg figure 6.2b and figure 6.9a) and therefore the slope of the $\ln T_{ei}(E)$ is high, which leads to higher thermopower. In contrast, the Fermi energy for alkanes is near the middle of the HOMO-LUMO gap (see fig. 6.1b and figure 6.8a), where the slope of the $\ln T_{ei}(E)$ is much lower. The electrical conductance of alkanes also is lower than oligoynes due to the broken π -conjugation (figures 6.1b and 6.2b). Simultaneously, as discussed above, the thermal conductance is lower for oligoynes. Combining the high electrical conductance of oligoynes, with their high thermopower and low thermal conductance, yields a maximum ZT of 1.4 (at a Fermi energy of $0.3eV$), which is several orders of magnitude higher than for alkanes, as shown in figures 6.11c,d. To achieve this high value, the Fermi energy should be optimally located in the tail of the LUMO resonance, which could be achieved by doping, or gating the molecules.

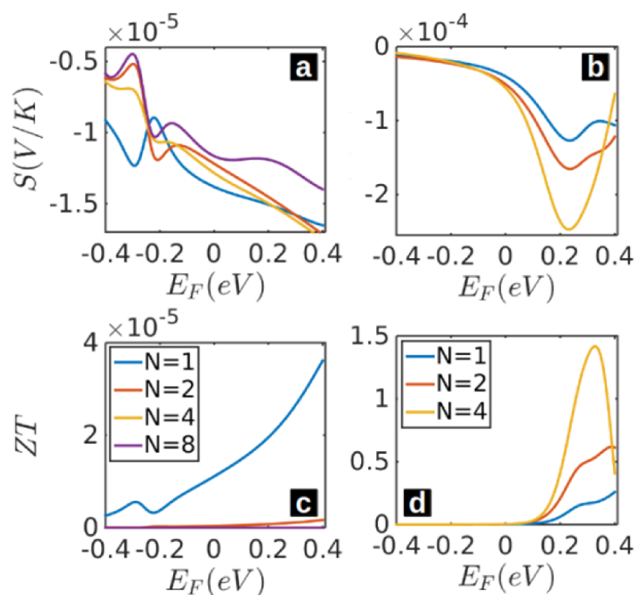


Figure 6.11. Thermopower S and full thermoelectric figure of merit ZT for alkanes and oligoynes. (a,b) show the thermopower of alkanes and oligoynes respectively. (c,d) show the figure of merit of alkanes and oligoynes respectively. Results are shown for molecules of different lengths N .

Understanding phonon and electron transport through molecules attached to metallic electrodes is crucial to the development of high-performance thermoelectric materials and to thermal management in nanoscale devices. I have studied simultaneously phonon and electron transport in alkane and oligoynes chains as model systems and find that due to the more rigid nature of the latter, the phonon thermal conductances of oligoynes are lower than that of the corresponding alkanes. Therefore in view of their higher thermal conductance, I conclude that alkanes are the better candidates for thermal management. The thermal conductance of oligoynes decreases monotonically with increasing length, whereas the thermal conductance of alkanes initially increases with length and then decreases. This difference in behaviour arises from phonon filtering by the gold electrodes and leads us to predict that the initial rise in thermal conductance of alkanes would disappear if higher-Debye-frequency electrodes such as graphene are used. Furthermore, by comparing results for different anchor groups and tip configurations I conclude that the above trends are resilient. This is a significant result, because it demonstrates that not just the molecule alone, but combinations of molecules and electrodes and their interplay should

be included in design strategies for future organic-molecule-based thermoelectricity. The low thermal conductance of oligoynes, combined with their higher thermopower and higher electrical conductance yield a maximum ZT of 1.4, which is several orders of magnitude higher than for alkanes. Therefore oligoynes are attractive candidates for high-performance thermoelectric energy conversion.

Computational Methods: The geometry of each structure consisting of the gold electrodes and a single molecule (alkane or oligoyne) was relaxed to the force tolerance of $20 \text{ meV}/\text{\AA}$ using the *SIESTA*[32] implementation of density functional theory (*DFT*), with a double- ζ polarized basis set (*DZP*) and the Generalized Gradient Approximation (*GGA*) functional with Perdew-Burke-Ernzerhof (*PBE*) parameterization. A real-space grid was defined with an equivalent energy cut-off of 250 Ry . From the relaxed xyz coordinate of the system, sets of xyz coordinates were generated by displacing each atom in positive and negative x, y and z directions by $\delta q' = 0.01 \text{\AA}$. The forces in three directions $q_i = (x_i, y_i, z_i)$ on each atom were then calculated by *DFT* without geometry relaxation. These sets of the force $F_i^q = (F_i^x, F_i^y, F_i^z)$ are used to construct the dynamical matrix as:

$$D_{ij} = \frac{K_{ij}^{qq'}}{M_{ij}} \quad (6.1)$$

where $K_{ij}^{qq'}$ for $i \neq j$ are obtained from finite differences

$$K_{ij}^{qq'} = \frac{F_i^q(\delta q'_j) - F_j^q(-\delta q'_j)}{2\delta q'_j} \quad (6.2)$$

and the mass matrix $M = \sqrt{M_i M_j}$. To satisfy momentum conservation, the K for $i = j$ (diagonal terms) is calculated from $K_{ii} = -\sum_{i \neq j} K_{ij}$. The phonon transmission $T_{ph}(\omega)$ then can be calculated from the relation:

$$T_{ph}(\omega) = Tr(\Gamma_L^{ph}(\omega)G_{ph}^R(\omega)\Gamma_R^{ph}(\omega)G_{ph}^{R\dagger}(\omega)) \quad (6.3)$$

In this expression, $\Gamma_{L,R}^{ph}(\omega) = i\left(\Sigma_{L,R}^{ph}(\omega) - \Sigma_{L,R}^{ph\dagger}(\omega)\right)$ describes the level broadening due to the coupling between left (L) and right (R) electrodes and the central scattering region formed from the molecule and closest contact layers of gold, $\Sigma_{L,R}^{ph}(\omega)$ are the retarded self-frequencies associated with this coupling and $G_{ph}^R = (\omega^2 I - D - \Sigma_L^{ph} - \Sigma_R^{ph})^{-1}$ is the retarded Green's function, where D and I are the dynamical and the unit matrices, respectively. The phonon thermal conductance κ_{ph} at temperature T is then calculated from:

$$\kappa_{ph}(T) = \frac{1}{2\pi} \int_0^\infty \hbar\omega T_{ph}(\omega) \frac{\partial f_{BE}(\omega, T)}{\partial T} d\omega \quad (6.4)$$

where $f_{BE}(\omega, T) = (e^{\hbar\omega/k_B T} - 1)^{-1}$ is Bose-Einstein distribution function and \hbar is reduced Planck's constant and $k_B = 8.6 \times 10^{-5} \text{ eV/K}$ is Boltzmann's constant.

To calculate electronic properties of the molecules in the junction, from the converged DFT calculation, the underlying mean-field Hamiltonian H was combined with our quantum transport code, *GOLLUM* [33]. This yields the transmission coefficient $T_{el}(E)$ for electrons of energy E (passing from the source to the drain) via the relation $T_{el}(E) = Tr(\Gamma_L^{el}(E)G_{el}^R(E)\Gamma_R^{el}(E)G_{el}^{R\dagger}(E))$ where $\Gamma_{L,R}^{el}(E) = i\left(\Sigma_{L,R}^{el}(E) - \Sigma_{L,R}^{el\dagger}(E)\right)$ describes the level broadening due to the coupling between left (L) and right (R) electrodes and the central scattering region, $\Sigma_{L,R}^{el}(E)$ are the retarded self-energies associated with this coupling and $G_{el}^R = (ES - H - \Sigma_L^{el} - \Sigma_R^{el})^{-1}$ is the retarded Green's function, where H is the Hamiltonian and S is the overlap matrix obtained from *SIESTA*. Using the approach explained in [11, 14, 33], the electrical conductance $G_{el}(T) = G_0 L_0$, the electronic contribution of the thermal conductance $\kappa_e(T) = (L_0 L_2 - L_1^2)/hTL_0$ and the thermopower $S(T) = -L_1/eTL_0$ of the junction are calculated from the electron transmission coefficient $T_{el}(E)$ where:

$$L_n(T) = \int_{-\infty}^{+\infty} dE (E - E_F)^n T_{el}(E) \left(-\frac{\partial f_{FD}(E, T)}{\partial E} \right) \quad (6.5)$$

and $f_{FD}(E, T)$ is the Fermi-Dirac probability distribution function $f_{FD}(E, T) = (e^{(E-E_F)/k_B T} + 1)^{-1}$, T is the temperature, E_F is the Fermi energy, $G_0 = 2e^2/h$ is the conductance quantum, e is electron charge and h is the Planck's constant. Since the above methodology ignores phonon-phonon and electron-phonon scattering, my agreement with the measurements of ref [25] suggests that such inelastic scattering is not a large effect. This is consistent with measurements on other molecules, which suggest that inelastic scattering of electrons at room temperature is a small effect, provided the length of the molecule is less than approximately $3nm$ (see eg [40, 41]). In our calculations, the size of the molecules are between 1.2 to $2.9 nm$.

References

- [1]C. Lambert, "Basic concepts of quantum interference and electron transport in single-molecule electronics," *Chemical Society Reviews*, pp. 875-888, 2015.
- [2]S. V. Aradhyia and L. Venkataraman, "Single-molecule junctions beyond electronic transport," *Nat Nano*, vol. 8, pp. 399-410, 2013.
- [3]Y. Geng, S. Sangtarash, C. Huang, H. Sadeghi, Y. Fu, W. Hong, *et al.*, "Magic Ratios for Connectivity-Driven Electrical Conductance of Graphene-like Molecules," *Journal of the American Chemical Society*, vol. 137, pp. 4469–4476, 2015.
- [4]J. R. Widawsky, W. Chen, H. Vázquez, T. Kim, R. Breslow, M. S. Hybertsen, *et al.*, "Length-dependent thermopower of highly conducting au–c bonded single molecule junctions," *Nano letters*, vol. 13, pp. 2889-2894, 2013.

- [5] H. Sadeghi, J. A. Mol, C. S. Lau, G. A. D. Briggs, J. Warner, and C. J. Lambert, "Conductance enlargement in picoscale electroburnt graphene nanojunctions," *Proceedings of the National Academy of Sciences*, vol. 112, pp. 2658–2663, 2015.
- [6] L. Sun, Y. A. Diaz-Fernandez, T. A. Gschneidner, F. Westerlund, S. Lara-Avila, and K. Moth-Poulsen, "Single-molecule electronics: from chemical design to functional devices," *Chemical Society Reviews*, vol. 43, pp. 7378-7411, 2014.
- [7] A. L. Moore and L. Shi, "Emerging challenges and materials for thermal management of electronics," *Materials Today*, vol. 17, pp. 163-174, 2014.
- [8] Y. Kim, W. Jeong, K. Kim, W. Lee, and P. Reddy, "Electrostatic control of thermoelectricity in molecular junctions," *Nature nanotechnology*, vol. 9, pp. 881-885, 2014.
- [9] J. R. Widawsky, P. Darancet, J. B. Neaton, and L. Venkataraman, "Simultaneous determination of conductance and thermopower of single molecule junctions," *Nano letters*, vol. 12, pp. 354-358, 2011.
- [10] H. Sadeghi, S. Sangtarash, and C. J. Lambert, "Electron and heat transport in porphyrin-based single-molecule transistors with electro-burnt graphene electrodes," *Beilstein Journal of Nanotechnology*, vol. 6, p. 1413, 2015.
- [11] H. Sadeghi, S. Sangtarash, and C. J. Lambert, "Enhanced Thermoelectric Efficiency of Porous Silicene Nanoribbons," *Sci. Rep.*, vol. 5, p. 9514, 2015.
- [12] P. Reddy, S.-Y. Jang, R. A. Segalman, and A. Majumdar, "Thermoelectricity in molecular junctions," *Science*, vol. 315, pp. 1568-1571, 2007.
- [13] N. A. Zimbovskaya, "The effect of dephasing on the thermoelectric efficiency of molecular junctions," *Journal of Physics: Condensed Matter*, vol. 26, p. 275303, 2014.

- [14] H. Sadeghi, S. Sangtarash, and C. J. Lambert, "Enhancing the thermoelectric figure of merit in engineered graphene nanoribbons," *Beilstein Journal of Nanotechnology*, vol. 6, pp. 1176-1182, 2015.
- [15] L.-D. Zhao, S.-H. Lo, Y. Zhang, H. Sun, G. Tan, C. Uher, *et al.*, "Ultralow thermal conductivity and high thermoelectric figure of merit in SnSe crystals," *Nature*, vol. 508, pp. 373-377, 2014.
- [16] G. J. Snyder and E. S. Toberer, "Complex thermoelectric materials," *Nature materials*, vol. 7, pp. 105-114, 2008.
- [17] D.-Y. Chung, T. Hogan, P. Brazis, M. Rocci-Lane, C. Kannewurf, M. Bastea, *et al.*, "CsBi₄Te₆: A High-Performance Thermoelectric Material for Low-Temperature Applications," *Science*, vol. 287, pp. 1024-1027, 2000.
- [18] L.-D. Zhao, V. P. Dravid, and M. G. Kanatzidis, "The panoscopic approach to high performance thermoelectrics," *Energy & Environmental Science*, vol. 7, pp. 251-268, 2014.
- [19] Q. Zhang, Y. Sun, W. Xu, and D. Zhu, "Organic thermoelectric materials: emerging green energy materials converting heat to electricity directly and efficiently," *Advanced Materials*, vol. 26, pp. 6829-6851, 2014.
- [20] S. Majumdar, J. A. Sierra-Suarez, S. N. Schiffres, W.-L. Ong, I. Higgs, C. Fred, A. J. McGaughey, *et al.*, "Vibrational mismatch of metal leads controls thermal conductance of self-assembled monolayer junctions," *Nano letters*, vol. 15, pp. 2985-2991, 2015.
- [21] G. Fagas, A. Kozorezov, C. Lambert, J. Wigmore, A. Peacock, A. Poelaert, *et al.*, "Lattice dynamics of a disordered solid-solid interface," *Physical Review B*, vol. 60, pp. 6459-6464, 1999.

- [22] A. Kambili, G. Fagas, V. Fal'ko, and C. Lambert, "Phonon-mediated thermal conductance of mesoscopic wires with rough edges," *Physical Review B*, vol. 60, pp. 15593-15596, 1999.
- [23] R. Y. Wang, R. A. Segalman, and A. Majumdar, "Room temperature thermal conductance of alkanedithiol self-assembled monolayers," *Applied Physics Letters*, vol. 89, p. 173113, 2006.
- [24] G. Kiršanskas, Q. Li, K. Flensberg, G. C. Solomon, and M. Leijnse, "Designing π -stacked molecular structures to control heat transport through molecular junctions," *Applied Physics Letters*, vol. 105, p. 233102, 2014.
- [25] T. Meier, F. Menges, P. Nirmalraj, H. Hölscher, H. Riel, and B. Gotsmann, "Length-Dependent Thermal Transport along Molecular Chains," *Physical review letters*, vol. 113, p. 060801, 2014.
- [26] F. Hüser and G. C. Solomon, "From Chemistry to Functionality: Trends for the Length Dependence of the Thermopower in Molecular Junctions," *The Journal of Physical Chemistry C*, vol. 119, pp. 14056–14062, 2015.
- [27] A. Tan, J. Balachandran, S. Sadat, V. Gavini, B. D. Dunietz, S.-Y. Jang, *et al.*, "Effect of Length and Contact Chemistry on the Electronic Structure and Thermoelectric Properties of Molecular Junctions," *Journal of the American Chemical Society*, vol. 133, pp. 8838-8841, 2011.
- [28] K. Baheti, J. A. Malen, P. Doak, P. Reddy, S.-Y. Jang, T. D. Tilley, *et al.*, "Probing the Chemistry of Molecular Heterojunctions Using Thermoelectricity," *Nano Letters*, vol. 8, pp. 715-719, 2008.

- [29] O. Karlström, M. Strange, and G. C. Solomon, "Understanding the length dependence of molecular junction thermopower," *The Journal of Chemical Physics*, vol. 140, p. 044315, 2014.
- [30] F. Pauly, J. K. Viljas, and J. C. Cuevas, "Length-dependent conductance and thermopower in single-molecule junctions of dithiolated oligophenylene derivatives: A density functional study," *Physical Review B*, vol. 78, p. 035315, 2008.
- [31] J. M. Soler, E. Artacho, J. D. Gale, A. García, J. Junquera, P. Ordejón, *et al.*, "The SIESTA method for ab initio order-N materials simulation," *Journal of Physics: Condensed Matter*, vol. 14, p. 2745, 2002.
- [32] J. P. Perdew, K. Burke, and M. Ernzerhof, "Generalized Gradient Approximation Made Simple," *Physical Review Letters*, vol. 77, pp. 3865-3868, 1996.
- [33] J. Ferrer, C. Lambert, V. Garcia-Suarez, D. Zsolt Manrique, D. Visontai, L. Oroszlani, *et al.*, "GOLLUM: a next-generation simulation tool for electron, thermal and spin transport," *New Journal of Physics*, vol. 16, p. 093029, 2014.
- [34] P. Moreno-García, M. Gulcur, D. Z. Manrique, T. Pope, W. Hong, V. Kaliginedi, *et al.*, "Single-Molecule Conductance of Functionalized Oligoynes: Length Dependence and Junction Evolution," *Journal of the American Chemical Society*, vol. 135, pp. 12228-12240, 2013.
- [35] B. Xu and N. J. Tao, "Measurement of Single-Molecule Resistance by Repeated Formation of Molecular Junctions," *Science*, vol. 301, pp. 1221-1223, 2003.
- [36] C. Wang, A. S. Batsanov, M. R. Bryce, S. Martín, R. J. Nichols, S. J. Higgins, *et al.*, "Oligoyne Single Molecule Wires," *Journal of the American Chemical Society*, vol. 131, pp. 15647-15654, 2009.

- [37] N. J. Tao, "Electron transport in molecular junctions," *Nat Nano*, vol. 1, pp. 173-181, 2006.
- [38] D. Segal, A. Nitzan, and P. Hänggi, "Thermal conductance through molecular wires," *The Journal of chemical physics*, vol. 119, pp. 6840-6855, 2003.
- [39] N. R. Claughton, M. Leadbeater, and C. J. Lambert, "Theory of Andreev resonances in quantum dots," *Journal of Physics: Condensed Matter*, vol. 7, p. 8757, 1995.
- [40] G. Sedghi, V. M. García-Suárez, L. J. Esdaile, H. L. Anderson, C. J. Lambert, S. Martín, *et al.*, "Long-range electron tunnelling in oligo-porphyrin molecular wires," *Nature nanotechnology*, vol. 6, pp. 517-523, 2011.
- [41] X. Zhao, C. Huang, M. Gulcur, A. S. Batsanov, M. Baghernejad, W. Hong, *et al.*, "Oligo(aryleneethynylene)s with Terminal Pyridyl Groups: Synthesis and Length Dependence of the Tunneling-to-Hopping Transition of Single-Molecule Conductances," *Chemistry of Materials*, vol. 25, pp. 4340-4347, 2013.

Chapter 7

Conclusions

My focus in this thesis was on electron and phonon transport theory in nano and molecular scale quantum devices, the modelling of the experiments and the developments of new concepts for future applications. I mainly considered junctions through which transport is assumed to be elastic and coherent. Good agreement between predictions and experiment suggests that this is a reasonable assumption. However, the method could be extended to the incoherent and inelastic regimes provided those parameters that the theory lacks are provided from experimental data e.g. the experimental HOMO-LUMO gap, the broadening due to the screening effect, Coulomb or additional energy, etc. There is some debate in the community whether or not these parameters could be predicted theoretically, but at present there is no method that could give a reliable result. In some cases the nature of the problem and the experimental limits do not even allow a qualitative treatment. For example screening effects depend on the actual shape of the contact for which the precise imaging of the junction (e.g. graphene - molecule - graphene) is not possible without destroying the junction.

As a theorist there are some quantities that you can calculate and some which you can not calculate. From my view, the crucial point is that we shall be able to predict the trends and develop new design strategies for future applications. I have tried throughout my PhD to utilize this modelling power with additional information revealed from the measurement for predicting new trends and proposing new applications, some of which is shown to be correct experimentally and some others that still need the experimental proof. Some of these results have been included in this thesis.

In this thesis explicitly I covered four main results in the areas of molecular sensing, new graphene-based molecular junctions, quantum interference rules, thermoelectricity and thermal

management. In the chapter 3, I demonstrated the discriminating sensing properties of new bilayer-graphene, sculptureene-based nano-pore devices by calculating the electrical current-voltage characteristics of two-terminal device in the absence and presence of given nucleobase for many different positions and orientations of bases within the pore. The proposed method is based on direct electrical current measurement and potentially has clear advantages compared with conventional DNA sequencing methods based on ionic current measurement. I showed that discriminating sensing is resilient but the nanopores will need to be calibrated individually before use. Therefore, the proposed method could open new routes for label free, fast and cheap DNA sequencing. This is still to be realized and our collaborators in Oxford University and Oxford nanopore technology are currently trying to implement these strategy supported by the QuEEN Program Grant funded by the UK EPSRC.

In chapter 4, I considered newly developed platform for single molecule device fabrication namely electro-burnt graphene nano-junctions which allows three terminal device realization at a single molecule level with gating capability. I addressed a hitherto mysterious feature of electro-burnt graphene junctions, namely a ubiquitous conductance enlargement at the final stages prior to nanogap formation. I showed that conductance enlargement at the point of breaking is a consequence of a transition from multiple-path to single-path quantum transport which suggest that conductance jumps provide a tool for characterising the atomic-scale properties of sp^2 -bonded junctions. In particular, conductance enlargement prior to junction rupture is a signal of the formation of electro-burnt junctions, with a current path formed from a single sp^2 -bond. I demonstrated that with greater control of the electro-burning feedback, one could create carbon-based atomic chains and filaments, which possess many of the characteristics of single molecules without the need for anchor groups, because the chains are already covalently bonded to electrodes.

In chapter 5, I discussed our newly developed mid-gap transport theory, where in the weak coupling regime and in the vicinity of the middle of the HOMO and LUMO gap, a minimal theory of the connectivity dependent transport and quantum interference could be used to model conductance measurements at least in most cases even better than the current very expensive DFT or GW calculations. Whereas DFT and GW treat E_F as a free parameter, chosen to give the best agreement with experiment, mid-gap transport theory is parameter free because the Fermi energy is restricted to be the mid-point of HOMO-LUMO gap. This allowed us to identify a new magic ratio rule (MRR), which captures the contribution of connectivity to the conductance

ratios of graphene-like cores. The MRR is simple to implement and exact for a tight-binding, bipartite lattice of identical sites with identical couplings, when the Fermi energy is located at the gap centre. This theory states that connectivity-driven conductance ratios are simply the squares of two magic integers, whose values depend only on the connectivity to the electrodes. This is shown to be in good agreement with our measurement and other experimental data from the literature. The MRR may be a useful guide for the design of future molecular-scale information processors.

In chapter 6, my focus was mostly on phonon transport in the molecular junction. This allows us to engineer transmitted phonons from one side of the junction to another for both thermoelectricity and thermal management. Ideally we would want to kill the phonons for efficient conversion of heat to electricity in thermoelectric device, whereas a high thermal conductance junction is needed for thermal management proposes to for instance, cool down the electronic circuit. Understanding both phonon and electron transport through molecules attached to metallic electrodes is crucial to the development of high-performance thermoelectric materials and to thermal management in nanoscale devices. I have studied simultaneously phonon and electron transport in alkane and oligoynes chains as model systems and find that due to the more rigid nature of the latter, the phonon thermal conductances of oligoynes are lower than those of the corresponding alkanes. Therefore in view of their higher thermal conductance, I conclude that alkanes are the better candidates for thermal management. The thermal conductance of oligoynes decreases monotonically with increasing length, whereas the thermal conductance of alkanes initially increases with length and then decreases. This difference in behaviour arises from phonon filtering by the gold electrodes and leads us to predict that the initial rise in thermal conductance of alkanes would disappear if higher-Debye-frequency electrodes such as graphene are used. Furthermore, by comparing results for different anchor groups and tip configurations I conclude that the above trends are resilient. This is a significant result, because it demonstrates that not just the molecule alone, but combinations of molecules and electrodes and their interplay should be included in design strategies for future organic-molecule-based thermoelectricity. The low thermal conductance of oligoynes, combined with their higher thermopower and higher electrical conductance yield a maximum ZT of 1.4, which is several orders of magnitude higher than for alkanes. Therefore oligoynes are attractive candidates for high-performance thermoelectric energy conversion.

Appendix A

Analytical calculation for the electrical conductance of rings and chains

To derive equations 4.1 and 4.2 of the chapter 4, consider the multi-branched structure shown below, which is composed of (generally different) left and right leads connected to a structure containing M (generally different) branches. An analytic formula for the transmission coefficient

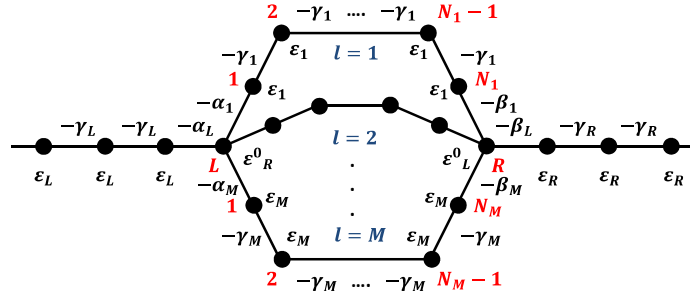


Figure A.0.1: A multi-branch structure described by a tight-binding model, with nodal sites L and R on the left and right connecting external current-carrying leads, by hopping matrix elements $-\alpha_L$ on the left and $-\beta_R$ on the right, and to internal branches l , by hopping matrix elements $-\alpha_L$ and $-\beta_l$, respectively. The energies of the nodal sites are ϵ_0^L and ϵ_0^R . The site energy and hopping matrix element of branch l are ϵ_l and γ_l , respectively.

of the above structure could be obtained [1] where the transmission coefficient is given by

$$T(E) = v_L \left(\frac{\alpha_L}{\gamma_L} \right)^2 |G_{RL}|^2 \left(\frac{\beta_R}{\gamma_R} \right)^2 v_R \quad (\text{A.0.1})$$

In this expression, v_L (v_R) is the electron group velocity in the left (right) lead, γ_L (γ_R) is the hopping element in the left (right) lead, α_L (β_R) are the coupling between the left (L) and right (R) nodal atom to the left (right) lead and G_{RL} is the Green's function of the whole structure describing a wave propagating from nodal atom L to nodal atom R.

To evaluate equation (A.0.1), the hopping elements $\gamma_L, \gamma_R, \gamma_l$ and orbital energies $\epsilon_L, \epsilon_R, \epsilon_l$ defining the left (L) and right (R) leads and each branch l should be chosen. For a given energy E , the wave-vectors in L, R and l are then given by $k_L(E) = \cos^{-1}(\epsilon_L - E)/2\gamma_L$, $k_R(E) = \cos^{-1}(\epsilon_R - E)/2\gamma_R$ and $k_l(E) = \cos^{-1}(\epsilon_l - E)/2\gamma_l$. The sign of the wave vectors is chosen such that the corresponding group velocities $v_L = 2\gamma_L \sin k_L(E)$, $v_R = 2\gamma_R \sin k_R(E)$ and $v_l = 2\gamma_l \sin k_l(E)$ are positive, or if the wavevector is complex, such that the imaginary part is positive. Next the orbital energies $\epsilon_L^0, \epsilon_R^0$ of the nodal sites L and R and their respective couplings $-\alpha_L, -\alpha_l$ and $-\beta_R, -\beta_l$ to the leads and branches should be chosen.

The final step in evaluating equation (A.0.1) is to compute the Green's function G_{RL} connecting the left nodal site L to the right nodal site R via the expression:

$$G_{RL} = \frac{y}{\Delta} \quad (\text{A.0.2})$$

In this equation, the numerator y is given by the following superposition of contributions from each of the M branches:

$$y = \sum_{l=1}^M y_l \quad (\text{A.0.3})$$

where

$$y_l = \frac{\alpha_l \beta_l \sin k_l}{\gamma_l \sin k_l (N_l + 1)} \quad (\text{A.0.4})$$

and N_l is the number of atoms in branch l . (For the special case $N_l = 1$, one should choose $\alpha_l = \beta_l = \gamma_l$.)

The denominator Δ of equation (A.0.2), which is given by

$$\Delta = y^2 - (a^L - x^L) (a^R - x^R) \quad (\text{A.0.5})$$

In this expression, the quantities x^L and x^R describe how a wave from the left or right nodal sites

is reflected back to those sites and are given by

$$x^L = \sum_{l=1}^M x_l^L \quad (\text{A.0.6})$$

$$x^R = \sum_{l=1}^M x_l^R \quad (\text{A.0.7})$$

$$x_l^L = \frac{\alpha_l^2 \text{sink}_l(N_l)}{\gamma_l \text{sink}_l(N_l + 1)} \quad (\text{A.0.8})$$

and

$$x_l^R = \frac{\beta_l^2 \text{sink}_l(N_l)}{\gamma_l \text{sink}_l(N_l + 1)} \quad (\text{A.0.9})$$

Finally, the quantities a_L and a_R contain information about the nodal site energies and their coupling to the left and right leads and are given by

$$a_L = (\epsilon_L^0 - E) - \frac{\alpha_L^2}{\gamma_L} e^{ik_L} \quad (\text{A.0.10})$$

and

$$a_R = (\epsilon_R^0 - E) - \frac{\beta_R^2}{\gamma_R} e^{ik_R} \quad (\text{A.0.11})$$

Consider the Green's function G_{RL} of a ring of atoms with N_1 atoms in branch 1 and N_2 atoms in branch 2. For a para-connected phenyl ring, $N_1 = N_2 = 2$, while for a meta connect ring, $N_1 = 1$ and $N_2 = 3$. Since all atoms are identical, all site energies within the branches are equal to a constant ϵ_0 and all couplings in figure A.0.1. (except α_R and α_L) are equal to γ , ie $\alpha_l = \beta_l = \gamma_l = \gamma$. This means that all wave vectors are equal to $k(E) = \cos^{-1}(\epsilon_0 - E)/2\gamma$ and $x_L = x_R$. First consider the case of an isolated ring for which $\alpha_L = \beta_R = 0$, in which case $a_L = a_R = 2\gamma \cos k$, $x_l = \frac{\gamma \text{sink}_l(N_l)}{\text{sink}_l(N_l + 1)}$, $y_l = \frac{\gamma \text{sink}_l}{\text{sink}_l(N_l + 1)}$. Since $\gamma \cos k - x_l = \gamma \text{sink} \frac{C_l}{S_l}$ where $S_l = \text{sink}_l(N_l + 1)$ and $C_l = \text{cosk}_l(N_l + 1)$, one obtains $a_L - x = \gamma \text{sink} \left(\frac{C_1}{S_1} + \frac{C_2}{S_2} \right)$, $y = \gamma \text{sink} (S_1 + S_2)/S_1 S_2$ and $\Delta = \frac{4\gamma^2 \sin^2 k}{S_1 S_2} \sin^2 k N/2$, where $N = N_1 + N_2 + 2$. These combine to yield

$$G_{RL} = \frac{y}{\Delta} = \frac{\text{cosk} \left(\frac{N_1 - N_2}{2} \right)}{2\gamma \text{sinksink} N/2} \quad (\text{A.0.12})$$

More generally, when the coupling to the left and right leads (α_L and β_R) are not zero, $a_L =$

$2\gamma\cos k + \sigma_L$ where $\sigma_L = (\epsilon_L^0 - \epsilon_0) - \frac{\alpha_L^2}{\gamma_L} e^{ikL}$ and similarly for a_R . In this case, I obtain equation

$$G_{RL} = \frac{\cos k(\frac{N_1 - N_2}{2})}{2\gamma \sin k \sin \frac{kN}{2} + \sigma_{ring}} \quad (\text{A.0.13})$$

where

$$\sigma_{ring} = \frac{2\gamma \sin k \sin kN (\sigma_L + \sigma_R) - S_1 S_2 \sigma_L \sigma_R}{2\gamma \sin k \sin \frac{kN}{2}} \quad (\text{A.0.14})$$

Furthermore, the calculation can easily be repeated for a single branch to yield

$$G_{RL} = \frac{-\sin k}{\gamma \sin k (N_1 + 3) + \sigma_{chain}} \quad (\text{A.0.15})$$

where

$$\sigma_{chain} = -2\sin k (N_1 + 2) (\sigma_L + \sigma_R) - \sin k (N_1 + 1) \sigma_L \sigma_R / \gamma \quad (\text{A.0.16})$$

As an example, for $N=6$, $k=\pi/2$, equation (A.0.13) for the a ring yields

$$G_{RL} = \frac{-2\gamma \cos k(\frac{N_1 - N_2}{2})}{4\gamma^2 - \sin k (N_1 + 1) \sin k (N_2 + 1) \sigma_L \sigma_R} \quad (\text{A.0.17})$$

For the para case, where $N_1=N_2=2$, this yields

$$G_{RL} = \frac{-2\gamma}{4\gamma^2 - \sigma_L \sigma_R} \quad (\text{A.0.18})$$

For the meta case, where $N_1=1$, $N_2=3$, it yields $G_{RL} = 0$ and for the ortho case, where $N_1=0$, $N_2=4$, it yields

$$G_{RL} = \frac{2\gamma}{4\gamma^2 - \sigma_L \sigma_R} \quad (\text{A.0.19})$$

These expressions demonstrate that at the centre of the HOMO-LUMO gap, ortho and para couplings lead to the same electrical conductance.

As a second example, of this odd-even conductance variation as a function of N_1 consider the Greens function of a linear chain at $k=\pi/2$. In this case equation (A.0.14) yields

$$G_{RL} = (-1)^{\frac{N_1+1}{2}} \frac{1}{2(\sigma_L + \sigma_R)} \quad \text{for } N_1 \text{ odd} \quad (\text{A.0.20})$$

and

$$G_{RL} = (-1)^{\frac{N_1}{2}} \frac{1}{\gamma + \sigma_L \sigma_R / \gamma} \quad \text{for } N_1 \text{ even} \quad (\text{A.0.21})$$

which shows that the conductance of such a chain also exhibits an odd-even oscillation as a function of the chain length. Furthermore, after dividing equation A.0.19 by equation A.0.22, one obtains

$$\frac{G_{ring}}{G_{chain}} = \frac{1 - \alpha}{2} \quad (\text{A.0.22})$$

where $\alpha = \frac{3\sigma_L \sigma_R / 4\gamma^2}{1 - \sigma_L \sigma_R / 4\gamma^2}$.

References

- [1] R. E. Sparks, V. M. García-Suárez, D. Z. Manrique, and C. J. Lambert, “Quantum Interference in Single Molecule Electronic Systems,” *Physical Review B*, vol. 075437, no. 7, p. 12, 2011.

Appendix B

Connectivity driven conductances in molecular junctions

The following derivation of the MRR involves proving the three 'ratio rules' of equations B.0.1, B.0.2 and B.0.3 stated below. Figure B.0.1a shows an example of a structure of interest, comprising a central region 2, connected by single atoms i and j to moieties on the left and right. The Greens function $\hat{G}_{ij}(E)$ connecting sites i and j of the structure of figure B.0.1a is proportional to the de Broglie wave amplitude at j , created by an incoming electron at i and the transmission coefficient $T_{ij}(E)$ is proportional to $|\hat{G}_{ij}(E)|^2$. Consequently the ratio of two transmission coefficients corresponding to connectivities i,j and l,m is given by the following Generalised Ratio Rule (GRR):

$$\frac{T_{ij}(E)}{T_{lm}(E)} = \frac{|\hat{G}_{ij}(E)|^2}{|\hat{G}_{lm}(E)|^2} \quad (\text{B.0.1})$$

This ratio does not depend on details of the electrodes or anchor groups, provided these are identical for both connectivities. Furthermore, if the coupling to moieties on the left and right are sufficiently weak, and E does not coincide with an eigenvalue of the isolated central region 2, $\hat{G}_{ij}(E) \approx \hat{g}_{ij}(E)$, where $\hat{g}_{ij}(E)$ is the Greens function of the isolated central region. In this case, the ratio of two transmission coefficients is given by the following Weakly-coupled Ratio Rule (WRR):

$$\frac{T_{ij}(E)}{T_{lm}(E)} = \frac{|\hat{g}_{ij}(E)|^2}{|\hat{g}_{lm}(E)|^2} \quad (\text{B.0.2})$$

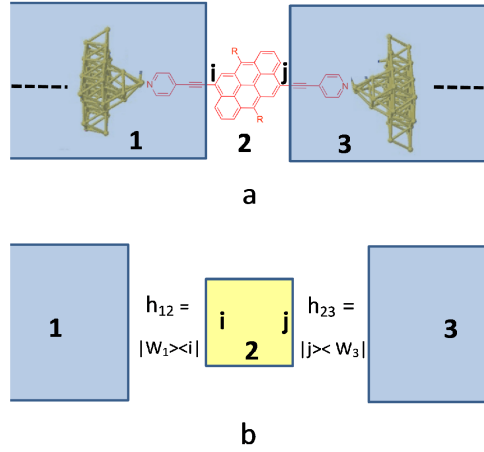


Figure B.0.1: (a) shows a physical realisation of a central moiety with sites i and j connected to current-carrying bonds, which in turn are connected to anchor groups and external electrodes. (b) shows a mathematical abstraction of such a system, in which an 'inner world' 2 is connected to an 'outer world' 1 and 3 by coupling matrices h_{12} and h_{23} .

Finally if E is located at the centre of the H-L gap (ie $E = E_F = 0$), then for a bi-partite lattice of identical sites, with equal numbers of primed and un-primed sites, described by a tight-binding model, $\hat{g}_{ij}(0) \approx (\frac{-1}{d}) M_{ij}$. Hence the ratio of two transmission coefficients corresponding to connectivities i, j and l, m is given by the following Magic Ratio Rule (MRR):

$$T_{ij}(0)/T_{lm}(0) = (M_{ij}/M_{lm})^2 \quad (\text{B.0.3})$$

The derivation of these ratio rules starts by noting that, the structure of figure B.0.1a is mathematically equivalent to the three-component system of figure B.0.1b, in which the central region 2 is connected to components 1 and 3, which at large distances from 2 take the form of crystalline, periodic leads, which extend to $-\infty$ and $+\infty$ respectively. Conceptually, when the coupling matrices h_{12} and h_{23} between these regions are set to zero, such a structure consists of a 'closed inner world' (ie an inner vector space) 2, whose Greens function g_{22} (for real E) is Hermitian, connected to an open 'outer world' composed of 1 and 3, whose Greens function is non-Hermitian.

When the coupling matrices are non-zero, the transmission coefficient $T_{ij}(E)$ from 1 to 3 is obtained from the Greens function G_{31} connecting orbitals on electrode atoms of 1 to orbitals on electrode atoms of 3. In fact at large distances from 2, where G_{31} can be projected onto scattering channels $|n_3\rangle$ and $|n_1\rangle$ of the crystalline leads of 3 and 1, the transmission coefficient

can be written

$$T_{ij}(E) = \sum_{n_1 n_3} T_{n_1 n_3}(E) \quad (\text{B.0.4})$$

where $T_{n_1 n_3}(E) = V_{n_1} V_{n_3} |\langle n_3 | G_{31} | n_1 \rangle|^2$. In this equation V_{n_1} and V_{n_3} are group velocities of electrons in channels $|n_1\rangle$ and $|n_3\rangle$. (This expression is mathematically equivalent to the formula $T_{ij}(E) = 4 \text{Tr}\{\Gamma_1 G_{22} \Gamma_3 G_{22}^\dagger\}$, where G_{22} is the Greens function of region 2, in the presence of couplings to regions 1 and 3.)

When $h_{12} = 0$ and $h_{23} = 0$, I denote the Greens functions of components 1, 2 and 3 by g_{11} and g_{22} and g_{33} respectively. Then Dyson's equation yields

$$G_{31} = g_{33} h_{32} G_{22} h_{21} g_{11} \quad (\text{B.0.5})$$

where

$$G_{22} = (g_{22}^{-1} - \Sigma)^{-1} \quad (\text{B.0.6})$$

or equivalently

$$G_{22} = g_{22} + g_{22} \Sigma G_{22} \quad (\text{B.0.7})$$

In this expression, $\Sigma = \Sigma_1 + \Sigma_3$, where $\Sigma_1 = h_{21} g_{11} h_{12}$ and $\Sigma_3 = h_{23} g_{33} h_{32}$.

So far the analysis has been rather general. I now consider the case where 1 is only coupled to a single orbital $|i\rangle$ in 2 and 3 is coupled to only a single orbital $|j\rangle$ in 2. (More generally, $|i\rangle$ and $|j\rangle$ could be arbitrary vectors in the inner vector space.) This situation is described by coupling matrices of the form $h_{21} = |W_1\rangle\langle i|$ and $h_{32} = |W_3\rangle\langle j|$, where $|W_1\rangle$ ($|W_3\rangle$) is a vector of matrix elements, in the space of 1 B.0.2, describing coupling of $|i\rangle$ ($|j\rangle$) to orbitals in 1 B.0.2. In this case, $\Sigma = \sigma_1 |i\rangle\langle i| + \sigma_3 |j\rangle\langle j|$, where $\sigma_l = \langle W_l | g_{ll} | W_l \rangle$, ($l = 1$ or 3). Writing $\hat{G}_{ij} = \langle i | G_{22} | j \rangle$, $\hat{g}_{ij} = \langle i | g_{22} | j \rangle$ where

$$\hat{G} = \begin{pmatrix} \hat{G}_{ii} & \hat{G}_{ij} \\ \hat{G}_{ji} & \hat{G}_{jj} \end{pmatrix} \quad \text{and} \quad \hat{g} = \begin{pmatrix} \hat{g}_{ii} & \hat{g}_{ij} \\ \hat{g}_{ji} & \hat{g}_{jj} \end{pmatrix},$$

yields from equation B.0.7,

$$\hat{G} = \hat{g} + \hat{g}\sigma\hat{G} \quad (\text{B.0.8})$$

where the self-energy matrix σ is given by $\sigma = \begin{pmatrix} \sigma_1 & 0 \\ 0 & \sigma_3 \end{pmatrix}$ Hence

$$\hat{G} = \hat{g}(1 - \sigma\hat{g})^{-1} \quad (\text{B.0.9})$$

Similarly equation B.0.5 yields

$$G_{31} = g_{33}|W_3\rangle\hat{G}_{ij}\langle W_1|g_{11} \quad (\text{B.0.10})$$

This expression shows that all elements of the matrix G_{31} are proportional to the single number \hat{G}_{ij} . Hence from equation B.0.4,

$$T_{ij}(E) = L(E)|\hat{G}_{ij}|^2 \quad (\text{B.0.11})$$

which proves the GRR of equation B.0.1. In equation B.0.11, the constant of proportionality $L(E) = \sum_{n_1 n_3} V_{n_1} V_{n_3} |\langle n_3 | g_{33} | W_3 \rangle \hat{G}_{ij} \langle W_1 | g_{11} | n_1 \rangle|^2$ is independent of the choice of i, j . Furthermore in equation B.0.9, \hat{g} is independent of the couplings $|W_1\rangle$ and $|W_3\rangle$. On the other hand, the self-energies σ_1 and σ_3 do depend on the couplings and on i, j . However in the weak coupling limit, these vanish and therefore in equation B.0.9, for sufficiently-weak couplings, it is safe to neglect the product $\sigma\hat{g}$, provided \hat{g} is finite. Since \hat{g} is the Greens function of the isolated region 2, which diverges when E coincides with an eigenvalue of 2, this condition requires that E should lie in an energy gap of 2. (It is interesting to note that this is the opposite of the condition for applicability of the Breit-Wigner formula for resonant transmission, which requires that E should be close to an energy level of 2.) When these conditions are satisfied, $\hat{G}_{ij}(E) \approx \hat{g}_{ij}(E)$, and the WRR of equation B.0.2 is obtained. The WRR can be utilised by noting that $g_{22}(E) = (E - H)^{-1}$, where H is the Hamiltonian for the isolated region 2. The WRR is a generally valid whenever $\sigma\hat{g}$ can be neglected compared with unity. Physically this means that if δ is the smaller of $|E_F - E_{HOMO}|$ and $|E_F - E_{LUMO}|$, then the level broadening Γ should be much less than δ , so the ratio $\Gamma/\delta \ll 1$.

The MRR of equation B.0.3 follows from the fact that if region 2 is a bi-partite lattice, then

the Hamiltonian H for the isolated region 2 is of the form

$$H = \begin{pmatrix} 0 & C \\ C^t & 0 \end{pmatrix} \quad (\text{B.0.12})$$

To obtain the transmission coefficient at the centre of the HOMO-LUMO gap, I evaluate the associated Green's function at $E = 0$, which yields

$$g_{22}(0) = \left(\frac{-1}{d}\right) \begin{pmatrix} 0 & M^t \\ M & 0 \end{pmatrix} \quad (\text{B.0.13})$$

where d is the determinant of C and the matrix of MIs M is the transpose of the cofactor matrix of C . Since the ratio of two matrix elements of $g_{22}(0)$ does not involve d , this completes the derivation of the MRR of equation B.0.3.

The condition that $g_{22}(0)$ is finite requires that d should not vanish. Clearly $d = 0$ when the rows or columns of C are linearly dependent, which occurs when C is not a square matrix; ie when the number of primed sites is not equal to the number of un-primed sites. In this case, a transmission resonance occurs at $E = 0$ and the Breit-Wigner formula should be used. For this reason, the MRR is restricted to bi-partite lattices of identical atoms with equal numbers of primed and un-primed atoms. If this condition is not satisfied, then for non-zero energies, the WRR should be used.

Since the upper left (lower right) blocks of g_{22} correspond to matrix elements between primed and primed (unprimed and unprimed) sites, the conductance vanishes when both electrodes connect to primed sites only (or unprimed sites only). For this reason, in addition to the non-trivial MIs shown in the M-tables tables, I assign an MI of zero to connectivities between primed and primed (or unprimed and unprimed) sites.

The above derivation also reveals that in addition to the MIs, each lattice possesses a second integer d . To each magic integer $M_{ii'}$, I assign a magic number (MN) defined by $m_{ii'} = M_{ii'}/d$. These allow the prediction of conductance ratios of molecules with different central cores via the following 'magic ratio rule' (MRR), which states that "the ratio of conductances of two molecules is equal to the squares of the ratios of their magic numbers."

Finally it is worth noting that knowledge of $T_{ij}(E)$ at $E = 0$ is particularly useful for bipartite lattices, because, $g_{22}(E)$ is symmetric about $E = 0$, so in the weak coupling limit $T_{ij}(E)$ will have a maximum or minimum (depending on the sign of the MI) at $E = 0$. Therefore at E

$= 0$, $\frac{dT_{ij}(E)}{dE}$ is zero and $T_{ij}(E)$ varies slowly with E . Finally I note that magic numbers are a useful concept for non-bipartite lattices of identical atoms, provided $\det H$ is non-zero. In this case, MIs are obtained by equating H to a connectivity matrix, which contains unit matrix elements $H_{ij} = 1$ between connected sites i and j only and defining $M = (\det H) H^{-1}$. However in this case the spectrum is not necessarily symmetric about the gap centre and $T_{ij}(E)$ will not necessarily be either a maximum or a minimum at $E = 0$.